THE STRUCTURE OF LOW-COVERAGE TI AND V ON THE AL(001) CRYSTAL SURFACE

by

Michael Kopczyk

A dissertation submitted in partial fulfillment
of the requirements for the degree

of

Doctor of Philosophy

in

Physics

MONTANA STATE UNIVERSITY
Bozeman, Montana

May, 2010

APPROVAL

of a dissertation submitted by

Michael Kopczyk

This dissertation has been read by each member of the dissertation committee and has been found to be satisfactory regarding content, English usage, format, citations, bibliographic style, and consistency, and is ready for submission to the Division of Graduate Education.

Dr. Richard J. Smith

Approved for the Department of Physics

Dr. Richard J. Smith

Approved for the Division of Graduate Education

Dr. Carl A. Fox

STATEMENT OF PERMISSION TO USE

In presenting this dissertation in partial fulfillment of the requirements for a doctoral degree at Montana State University, I agree that the Library shall make it available to borrowers under rules of the Library. I further agree that copying of this dissertation is allowable only for scholarly purposes, consistent with "fair use" as prescribed in the U.S. Copyright Law. Requests for extensive copying or reproduction of this dissertation should be referred to ProQuest Information and Learning, 300 North Zeeb Road, Ann Arbor, Michigan 48106, to whom I have granted "the exclusive right to reproduce and distribute my dissertation in and from microform along with the non-exclusive right to reproduce and distribute my abstract in any format in whole or in part."

Michael Kopczyk

May, 2010

DEDICATION

This work is dedicated to my parents Michael and Teodora Kopczyk, to whom I am grateful for life and upbringing, whose continued love, support and encouragement now and all throughout my life has given me opportunity grow up in this great and cherished land of America, granting me opportunities which they did not have in their youth and homeland of Ukraine.

ACKNOWLEDGEMENTS

My appreciation and thanks goes to Dr. Richard J. Smith my advisor, for his sponsorship and support, direction, advice and example of professionalism. I'd like to thank all my professors at MSU, especially Dr. V. Hugo Schmidt, Dr. George F. Tuthill, Dr. John L. Carlsten, Dr. Gregory E. Francis, Dr. John J. Neumeier, Dr. Yves Idzerda and Dr. Carla Riedel along with a special thanks to Dr. John E. Drumheller. My thanks goes to Michael Lerch, Nick Childs, Camas Key, Martin Finsterbusch, Chih Tsai Long, Dr. Asghar Kayani, Dr. Hui Chen, and Dr. Weerasinghe Priyantha for all their encouragement, help and support in the lab. A special thanks to Dr. Dae Sun Choi from Korea, for his guidance and teaching during his sabbatical at MSU. Also my thanks to Dr. Guillermo Bozzolo for his work with the BFS Model for Alloys, and providing me with a thesis topic. My hearty thanks and appreciation to Margaret Jarrett, Sarah Barutha, Sherry Heis, Jeannie Gunderson and Rose Waldon in the main office, to Jeremy Gay for help with computing matters, and to Norm Williams, John Getty and Bo Glaspey for technical support and help with our projects.

Thank you to Paul Nachman and all my friends and classmates. Special thanks to Oleg Zadvornyy and Kyle Suvak for their support and friendship. Extra special thanks to Robert G. DeCesaris, his wife Cami and daughters Victoria and Christina for their love, support and friendship. And last but not least my greatest thanks to my parents Michael and Teodora Kopczyk, my sister Mary and brother-in-law Ben, my nephew Anthony his wife Nicole, nephew Gary his wife Karyn, and their families for their love, encouragement and support.

Funding Acknowledgement: This work was supported by the National Science Foundation under Grant No. DMR 0516603.

TABLE OF CONTENTS

1. INTRODUCTION 1

1.1 Background 1
1.2 Ti and V on Al(001) 1
1.3 List of Acronyms 4

2. NEW UHV CHAMBER 6

2.1 Design of New UHV Chamber 6
2.2 Motivation 9
2.3 Experimental Techniques 11
2.4 Goniometer Sample Positioning Device 12
2.5 Comparison of LEIS Spectra in Old Chamber versus New Chamber 15

3. RBS 20

3.1 Introduction to RBS 20
3.2 RBS Elemental Composition Analysis 21
3.2.1 Kinematic Factor 21
3.2.2 Absolute Scattering Cross Section 22
3.2.3 RBS Yield 25

4. LEIS 29

4.1 LEIS - Introduction and Theory 29
4.1.1 Overview and Comparison with RBS 29
4.1.2 Al(001) Crystal Coordinate System 30
4.2 LEIS Experimental Setup 32
4.3 Binary-Particle Collision Dynamics in LEIS 34
4.3.1 Kinematic Factor 34
4.3.2 LEIS Yield and Scattering Cross Section 35
4.3.3 Screened-Coulomb Potential 36
4.3.3.1 Overview of the Interaction Potential in LEIS 36
4.3.3.2 Thomas-Fermi Screening Function $\chi(x)$ 38
4.3.3.3 The Screening Length a 39
4.3.4 The Shadow Cone 39
4.4 LEIS Spectra 43
4.4.1 LEIS energy scans 44
4.4.2 Azimuth-angle Scans 45
4.4.3 Polar Scans 47
4.4.3.1 Polar Scan in the [100] Azimuth 47

TABLE OF CONTENTS – CONTINUED

4.4.3.2 Polar Scan in the [110] Azimuth 49

5. LEED 53

5.1 An Introduction to LEED 53
5.2 Geometry and Basis Vectors 54
5.3 Construction of LEED Image - Structure Factor Analysis 56
5.4 Ti on Al(001) 59
5.5 Ag on Al(001) 63

6. THE BFS MODEL FOR ALLOYS 68

6.1 BFS Model for Analysis of TMs on Metal Substrates 68
6.1.1 Ti Interlayer for the Fe-Al System 69
6.1.2 Layer Examples of the Ti Interlayer Fe-Al System 72
6.1.3 Basis for Ti and V as Interlayers via the BFS Model 76
6.2 BFS Method Analysis of Ti and V on Al 77
6.2.1 Ti on an Al-bcc (100) Substrate 78
6.2.1.1 1 ML Ti on Al-bcc 78
6.2.1.2 0.5 ML Ti on Al-bcc 78
6.2.2 Ti on an Al-fcc (100) Substrate 79
6.2.2.1 1 ML Ti on Al-fcc 79
6.2.2.2 0.5 ML Ti on Al-fcc 80
6.2.3 V on an Al-bcc (100) Substrate 81
6.2.3.1 1 ML V on Al-bcc 81
6.2.3.2 0.5 ML V on Al-bcc 82
6.2.4 Conclusion for BFS Model Results for Ti-Al and V-Al 83

7. SIMULATION OF LEIS POLAR-ANGLE SCAN SPECTRA 84

7.1 Introduction and Overview 84
7.2 Two-dimensional Trajectory Tracing Method 84
7.2.1 Magic Formula Expressions and Coefficients 87
7.2.2 Universal Screening Function and Screening Length 92
7.3 Simulation Program Components 93
7.3.1 LEISsim Data Output and Convolution 93
7.3.1.1 Comparing ion beam step sizes $d = 0.001$ Å vs. $d = 0.01$ Å 94
7.4 LEIS Simulated Polar Scans for the Clean Al(001) Crystal 97
7.4.1 Simulated Polar scan in [100] Azimuth 98
7.4.2 Simulated Polar scan in [110] Azimuth 99
7.5 Simulations Accounting for Neutralization Effects 99

TABLE OF CONTENTS – CONTINUED

7.5.1 Simulated Polar scan in [100] Azimuth 100
7.5.2 Simulated Polar scan in [110] Azimuth 101
7.6 Motivation for using simulated spectra 103

8. STRUCTURE OF ULTRA-THIN TI FILM ON THE AL(001) SURFACE ... 104

8.1 Introduction 104
8.2 Experiment 105
8.3 Results 110
8.3.1 LEED 110
8.3.2 LEIS 111
8.3.2.1 LEIS Energy Scans 111
8.3.2.2 LEIS Azimuth-angle Scans 112
8.3.2.3 LEIS Polar-angle Scans (sub-monolayer Ti coverage) 114
8.3.2.4 LEIS Polar-angle Scans (at higher Ti coverage) 119
8.4 Conclusions 121
8.5 LEIS Simulated Polar Scans for Ti on the Al(001) Crystal 122
8.5.1 Simulated 0.82 ML Ti on Al(001) 124
8.5.1.1 Simulated Polar Scans in [100] Azimuth 126
8.5.1.2 Simulated Polar Scans in [110] Azimuth 127
8.5.2 Simulated 1.5 ML Ti on Al(001) 129
8.5.2.1 Simulated Polar Scans in [100] Azimuth 130
8.5.2.2 Simulated Polar Scans in [110] Azimuth 132

9. V ON THE AL(001) SURFACE 135

9.1 Introduction 135
9.2 Experiment 135
9.3 LEED Results 137
9.4 LEIS Results 139
9.4.1 LEIS Energy Scans 139
9.4.1.1 LEIS Energy Scans for 0.6 ML V 139
9.4.1.2 LEIS Energy Scans for 2.5 ML V 140
9.4.2 LEIS Azimuth Scans 141
9.4.3 LEIS Polar Scans 144
9.4.3.1 LEIS Polar-angle Scans for 0.6 ML V 144
9.4.3.2 LEIS Polar-angle Scans for 2.5 ML V 146
9.5 Summary of V-Al LEIS Results 150
9.6 Contrasting Ti and V on Al(001) 151
9.7 Conclusions 151

TABLE OF CONTENTS – CONTINUED

10. CONCLUSION 153

10.1 A Contrasting Comparison of Ti and V on Al(001) 153
10.1.1 LEED and LEIS Results Ti and V on Al(001) 153
10.1.2 Heats of Formation ΔH for Ti-Al and V-Al Alloys 154
10.1.2.1 Ti alloyed with Al 154
10.1.2.2 V alloyed with Al 155
10.1.2.3 Comparing Ti-Al with V-Al Alloys using ΔH^{for} 155
10.1.3 Comparing Surface Energies for Bulk Ti, V and Al 156
10.1.4 Atomic Size and Other Characteristics of Ti, V and Al 158
10.1.4.1 Electronegativity and Other Characteristics of Ti, V and Al 158
10.1.4.2 Atomic Size of Ti, V and Al 159
10.1.5 Conclusion: Effectiveness of V as an Interlayer Compared to Ti 160
10.2 Future Work 162
10.2.1 Expanded Studies for Ti and V on Al(001) 162
10.2.2 Cr, Nb and Mo on Al(001) 162
10.2.3 BFS Model Analysis of Fe-V-Al(001) Interlayer System 163
10.2.4 RBS Channeling Study of the Fe-V-Al(001) Interlayer System 163
10.2.5 Follow-up Work with Simulation of LEIS Polar Scans 164

REFERENCES CITED 165

LIST OF TABLES

Table Page

3.1 Comparison of radius r of disk with effective area of $\sigma(\theta)$ for three spectroscopic techniques. 25

4.1 Al-clean azimuth scan, contributing surface layer collision atom for reference-line peaks. Refer to peak labels in Fig. 4.5(b). 47

4.2 [100] azimuth, contributing layer and collision atom for Al-clean scan reference-line peaks. Refer to peak labels in Fig. 4.6(b). 49

4.3 [110] azimuth, contributing layer and collision atom for Al-clean scan reference-line peaks. Refer to peak labels in Fig. 4.7(b). 51

6.1 BFS Method results as applied to Al substrate and listed TM overlayers [1].70

6.2 BFS Method results pairing Al with Fe and Ti [1]. 71

6.3 BFS Method results pairing Ti with Fe and Al [1]. 72

6.4 First example Fe/Al/Al [1]..... 73

6.5 Next Al/Fe/Al/Al [1]..... 73

6.6 Ti/Al/Al [1]..... 74

6.7 Al/Ti/Al/Al [1]..... 74

6.8 Fe/Ti/Al/Al [1]..... 74

6.9 Ti/Fe/Al/Al [1]..... 75

6.10 Fe/Fe/Ti/Al/Al [1]..... 75

6.11 BFS Method results pairing substrate Al with transition elements Ti and V [1]. 76

6.12 BFS Method calculated cell energies for successive top four layers for 1 ML Ti on Al(100)-*bcc*. 78

6.13 BFS Method calculated cell energies for successive top four layers for 0.5 ML Ti on Al(100)-*bcc*. 79

6.14 BFS Method calculated cell energies for successive top four layers for 1 ML Ti on Al(100)-*fcc*. 80

6.15 BFS Method calculated cell energies for successive top four layers for 0.5 ML Ti on Al(100)-*fcc*. 81

LIST OF TABLES – CONTINUED

Table Page

6.16 BFS Method calculated cell energies for successive top four layers for 1 ML V on Al(100)-*bcc*. 81

6.17 BFS Method calculated cell energies for successive top four layers for 0.5 ML V on Al(100)-*bcc*. 82

7.1 Values for constants in Equation 7.10 for the Molière and Universal screening functions [2]..... 91

8.1 [100] azimuth, contributing layer and collision atom for Al-clean scan reference-line peaks. Refer to peak labels in Figure 8.5(b). 116

8.2 [110] azimuth, contributing layer and collision atom for Al-clean scan reference-line peaks. Refer to peak labels in Figure 8.6(b). 118

8.3 Neutralization constants for each layer of the model target planes for both low index azimuths. 124

8.4 Ti atom placement for two target planes in the [100] azimuth for 0.82 ML Ti on Al(100)..... 126

8.5 Ti atom placement for two target planes in the [110] azimuth for 0.82 ML Ti on Al(100)..... 128

8.6 Ti atom placement for two target planes in the [010] azimuth for 1.5 ML Ti on Al(100). 131

8.7 Ti atom placement for two target planes in the [110] azimuth for 1.5 ML Ti on Al(100). 133

9.1 Azimuth scan η_{signal} value comparisons for V deposition thickness of 0.6 ML vs. 2.5 ML. 143

9.2 Azimuth scan η_{signal} values for 0.8 ML Ti on Al(001)..... 144

9.3 Polar scan ([100] azimuth) η_{signal} value comparisons for V deposition thickness of 0.6 ML vs. 2.5 ML..... 148

9.4 Polar scan ([100] azimuth) η_{signal} value comparisons for Ti deposition thickness of 0.7 ML vs. $\geq$ 1 ML..... 148

9.5 Polar scan ([110] azimuth) η_{signal} value comparisons for V deposition thickness of 0.6 ML vs. 2.5 ML..... 149

LIST OF TABLES – CONTINUED

Table Page

9.6 Polar scan ([110] azimuth) η_{signal} value comparisons for Ti deposition thickness of 0.7 ML vs. $\geq$ 1 ML. 150

10.1 Values for enthalpy of formation ΔH (kJ/mol) experimental and calculated [3] for alloys of Al with Ti at ambient temperature. 155

10.2 Values for heats of formation ΔH (kJ/mol) experimental and calculated [3] for alloys of Al with V at ambient temperature. 155

10.3 Surface energies calculated (FDC) and experimental (Exp) for Al, Ti and V for low index surfaces [4]. 157

10.4 Comparison of atomic characteristics of Al, Ti and V. [5]. 158

LIST OF FIGURES

Figure Page

2.1 New UHV chamber drawings, each showing the beam line connection port to the right. (a) top view - side port detail, (b) top view - top port detail, (c) side view, (d) bottom view - bottom port detail. 7

2.2 Newly constructed UHV chamber mounted on stand before initial vaccum testing. 8

2.3 Cornell scattering geometry. 9

2.4 IBM scattering geometry. 10

2.5 New UHV chamber in operation installed on the beam line. 13

2.6 Schematic of the chamber scattering geometry. 14

2.7 Three-axis positioning goniometer used in the new UHV chamber. (a) Full view. (b) Sample holder 3-axis movement concentric-ring assembly. (c) Goniometer section that resides in the chamber, back view of sample holder. (d). Goniometer section that resides in the chamber, front view of sample holder. 16

2.8 Al(001) crystal sample mounted on the goniometer sample holder as installed inside the new UHV chamber. 17

2.9 LEIS polar angle scan spectra comparing those collected in the old chamber to those from the new UHV chamber. (a) [100] azimuth. (b) [110] azimuth. 18

2.10 Another set of LEIS polar angle scan spectra comparing those collected in the old chamber to those from the new UHV chamber. (a) [100] azimuth. (b) [110] azimuth. 19

3.1 Scattering geometry for RBS. 22

3.2 RBS spectrum for 2.5 ML V on the Al(001) surface. 26

4.1 Three-dimensional representation of the Al crystal *fcc* lattice with a characteristic Al(001) surface plane. 31

4.2 LEIS experimental setup schematic. 32

4.3 Schematic of shadow cone. 40

4.4 (a) LEIS energy scan post Ti deposition onto Al(001) surface. (b) Corresponding RBS spectrum used to determine Ti coverage at 0.8 ML. . 44

LIST OF FIGURES – CONTINUED

Figure Page

4.5 (a) Schematic of Al(001) surface plane. (b) Azimuth scan: Al-clean signal. 46

4.6 (a) Schematic of Al(100) plane perpendicular to crystal surface. (b) Polar scan along [100] azimuth: Al-clean signal. 48

4.7 (a) Schematic of Al(110) plane perpendicular to crystal surface. (b) Polar scan along [110] azimuth: Al-clean signal. 49

4.8 (a) Schematic of two (110) planes perpendicular to crystal surface, one with dark colored atoms and one with light-gray colored atoms. (b) Three-dimensional representation of the Al(001) crystal showing two unit cells. 51

5.1 Schematic representation of a LEED system showing electron gun, filtering grids and phosphor screen. In the lower left corner is a representation of the Bragg law of diffraction. To the lower right is an actual LEED image for the clean Al(001) surface. 53

5.2 Position vector representation (a) real space, (b) reciprocal space. 55

5.3 Real space representation of the Al(001) crystal surface showing two-atom unit cell. 57

5.4 (a) Reciprocal space representation of LEED screen for construction of LEED image for an Al(001) crystal surface, and (b) corresponding LEED image. 58

5.5 Real-space representation of Ti on the Al(001) crystal surface showing the four-atom unit cell. Small dark circles denote Al atoms and large lighter circles denote Ti atoms. 59

5.6 (a) Reciprocal space representation of the Ti-Al(001) system and (b) LEED image for ≈ 2.4 ML Ti on Al(001). 61

5.7 $c(2 \times 2)$ LEED schematic with accompanying table listings of solution values from Eqn. 5.14 62

5.8 Real-space representation of Ag on the Al(001) crystal surface showing the ten-atom unit cell. 63

5.9 Reciprocal space representation of the Ag-Al(001) system, table listings of solution values from Eqn. 5.20 and inset LEED schematic. 66

LIST OF FIGURES – CONTINUED

Figure Page

5.10 (a) LEED image for 0.7 ML Ag on Al(001) with (b) accompanying schematic drawing for clarity. 67

7.1 LEISsim Al (100) substrate plane model showing incident ion beam in [100] azimuth. 86

7.2 Scattering triangle for obtaining expressions to calculate the center-of-mass scattering angle Θ in a binary collision between an incoming ion and stationary target atom, as given by Ziegler [2]..... 89

7.3 LEISsim data output as processed by *GenOut* (spectrum with sharp peaks) and convolution with a gaussian (smooth rounded-peak spectrum) for a simulated polar-angle scan. This simulation was generated for the Al (100) plane, perpendicular to the surface, along the [100] azimuth. 95

7.4 Comparing simulated spectrum generated by incoming ion step sizes of $d = 0.001$Å and $d = 0.01$Å. (a) Raw *GenOut* data, (b) Convolution of data with a gaussian. 97

7.5 LEISsim polar-angle scan in [100] azimuth, spectrum is the sum of contributions from the top three layers (1, 2, 3)..... 98

7.6 LEISsim polar-angle scan in [110] azimuth, spectrum is the sum of contributions from the top three layers (1, 3, 5)..... 99

7.7 Simulated Al-clean polar-angle scan in the [100] azimuth as compared to a typical corresponding experimental spectrum..... 101

7.8 Simulated Al-clean polar-angle scan in the [110] azimuth as compared to a typical corresponding experimental spectrum..... 102

8.1 Theoretical models of Ti on Al(001) proposed by D. Spišák and J. Hafner [6]..... 106

8.2 Two LEED images, (a) clean Al(001) at 83.0 eV LEED-electron energy, (b) $\approx$ 2.4 ML Ti on Al(001) showing a faint c(2×2) pattern at 86.7 eV LEED-electron energy. 110

8.3 LEIS energy scan spectra post Ti deposition on the Al(001) crystal surface; (a) 0.8 ML Ti, [100] azimuth, (b) 0.7 ML Ti, [110] azimuth..... 111

LIST OF FIGURES – CONTINUED

Figure Page

8.4 Azimuth-angle scan spectra, Al(001) surface collected at a 12° polar angle, showing the Al-clean scan (taken at an incident ion energy of 1.2 keV), and the Al-peak and Ti-peak scans (0.8 ML Ti, taken at an incident ion energy of 1.0 keV). 113

8.5 (a) The Al(100) crystal plane, perpendicular to surface plane. (b) LEIS polar-angle scan spectra in the [100] azimuth for the clean Al(001) surface and for 0.7 ML Ti on the Al(001) surface..... 115

8.6 (a) The Al(110) crystal plane, perpendicular to surface plane. (b) LEIS polar-angle scan spectra in the [110] azimuth for the clean Al(001) surface and for 0.7 ML Ti on the Al(001) surface..... 118

8.7 LEIS Polar-angle scan spectra for higher Ti coverage on the Al(001) surface. (a). [100] azimuth. (b). [110] azimuth. 119

8.8 Proposed model for 1.5 ML Ti on the Al(001) surface..... 122

8.9 Low index azimuth directions and planes in the Al(001) crystal..... 123

8.10 Portion of 3-D model for 0.82 ML Ti on the Al(001) surface..... 125

8.11 LEIS polar-angle scan spectra in the [100] azimuth for the clean Al(001) surface and for Ti on the Al(001) surface. (a) Simulated 0.82 ML Ti, (b) Experimental 0.7 ML Ti. 127

8.12 LEIS polar-angle scan spectra in the [110] azimuth for the clean Al(001) surface and for Ti on the Al(001) surface. (a) Simulated 0.82 ML Ti, (b) Experimental 0.7 ML Ti. 129

8.13 Portion of 3-D model for 1.5 ML Ti on the Al(001) surface. 130

8.14 LEIS polar-angle scan spectra in the [100] azimuth for the clean Al(001) surface and for Ti on the Al(001) surface. (a) Simulated 1.5 ML Ti, (b) Experimental higher coverage Ti. 132

8.15 LEIS polar-angle scan spectra in the [110] azimuth for the clean Al(001) surface and for Ti on the Al(001) surface. (a) Simulated 1.5 ML Ti, (b) Experimental higher coverage Ti. 133

9.1 Two LEED images, (a) clean Al(001) $p(1\times1)$ pattern at 83.0 eV LEED-electron energy, (b) $\sim$0.6 ML V on Al(001) $p(1\times1)$ pattern at 93.7 eV LEED-electron energy. 138

LIST OF FIGURES – CONTINUED

Figure Page

9.2 Two LEED images, (a) ∼2.5 ML V on Al(001) $p(1 \times 1)$ pattern at 90.0 eV LEED-electron energy, (b) ∼2.5 ML V on Al(001) $p(1 \times 1)$ pattern at 95.1 eV LEED-electron energy. 139

9.3 LEIS energy scan spectra post 0.6 ML V deposition on the Al(001) crystal surface, incident He^+ beam oriented at a 45° polar angle and 52° azimuth angle (a) before collection of set of LEIS-angular scans, sample current at ∼ 13.7 nA, (b) after collection of set of LEIS-angular scans, sample current at ∼ 14.1 nA. 140

9.4 LEIS energy scan spectra post 2.5 ML V deposition on the Al(001) crystal surface, incident He^+ beam oriented at a 45° polar angle and 52° azimuth angle (a) before collection of set of LEIS-angular scans, sample current at ∼ 13 nA, (b) after collection of set of LEIS-angular scans, sample current at ∼ 14.2 nA. 141

9.5 Azimuth-angle scan spectra for the Al(001) surface collected at a 12° polar angle, showing the Al-clean scan, and the Al-peak and V-peak scans for, (a) ∼0.6 ML V coverage, and (b) ∼2.5 ML V coverage. 142

9.6 LEIS polar-angle scans for 0.6 ML V coverage plotted with the Al-clean scan for (a) the [100] azimuth, and (b) the [110] azimuth. 145

9.7 LEIS polar-angle scans for 2.5 ML V coverage plotted with the Al-clean scan for (a) the [100] azimuth, and (b) the [110] azimuth. 147

ABSTRACT

The BFS (Bozzolo-Ferrante-Smith) Method for Alloys predicts that V and Ti would be effective interlayers to act as a diffusion barrier between a metal substrate and metal overlayer. Previous work from our group using the RBS channeling technique, determined that Ti is an effective interlayer between Fe and the Al(001) bulk substrate. The Fe-V-Al(001) system was not treated in this earlier work. This thesis is focused on studying the structure of the first bi-metal interface of these tri-metal systems, i.e. the Ti-Al(001) and V-Al(001) interfaces. LEIS (low-energy ion scattering spectroscopy) and LEED (low-energy electron diffraction) were used as experimental techniques specifically designed to study the surface structure of the top few layers of sample surfaces. LEED images for the Ti-Al case gave a $c(2 \times 2)$ pattern, a change from the standard $p(1 \times 1)$ pattern of the clean Al(001) surface, suggesting Ti occupies every other Al lattice site. LEIS results suggest that Ti prefers subsurface occupancy for sub-monolayer Ti coverage, and fills the surface layer as deposition thickness increases above but near 1 ML. LEED images for the V-Al system produced nothing out of the ordinary, but rather display a blurry $p(1 \times 1)$ image, becoming less distinct as V deposition thickness increases, suggesting that V atoms place themselves in the Al substrate with no specific order. LEIS results suggest that V prefers sub-surface occupancy for both sub-monolayer and higher (up to 2.5 ML) V coverage. Contrasting the results of these experiments, we determined that the structural characteristics of the V-Al interface differed enough from those of the Ti-Al interface, to conclude that V cannot be considered as effective of an interlayer as Ti.

CHAPTER 1
INTRODUCTION

1.1 Background

This thesis is a study of Ti and V on the Al(001) crystal surface. The work was performed in the Ion Beams Lab in the Department of Physics at Montana State University, Bozeman, MT, under the direction of Dr. Richard J. Smith.

Experiments were conducted in an ultra-high vacuum chamber using various spectroscopic techniques to study the surface structure of low-coverage Ti and V on the Al(001) crystal surface. The lab is equipped with a 2 MV van de Graaff linear accelerator which accelerates high energy ions (He^+ or H^+) into the vacuum chamber for conducting RBS (Rutherford backscatteing spectroscopy) measurements on the sample. Most of this work was centered around the use of LEIS (low-energy ion scattering spectroscopy) and LEED (low-energy electron diffraction) to do surface structure studies. This study was part of the lab group's interlayer project. The study of interlayers involves investigating the structure of two different metals (an overlayer and substrate) separated by a thin metal interlayer [7]. My thesis work did not focus directly on the three 'sandwiched' metals, but rather on the structure of the first two metal components of the system, hence the study of Ti on Al(001) and V on Al(001).

1.2 Ti and V on Al(001)

Integral to our study as part of the interlayer project, was earlier collaborations with Dr. Guillermo Bozzolo, and his work in creating the BFS (Bozzolo-Ferrante-Smith) Method for Alloys [8]. The BFS Method is a technique for theoretically

calculating, the formation energies of a pair of metal elements to determine their likelihood to alloy. The results give a value for the energy of formation which if negative (lowering of the total energy of the system) the two are said to be likely to alloy. If on the other hand the result is positive (raising of the total energy) it is unlikely the two will alloy. The computer program that he and his team created involves semi-empirical calculations based on quantum-mechanical principles to arrive at a value for the formation energy of atoms in a lattice structure. The formation energy is composed of two contributions, one term accounts for lattice strain (stretching or compressing of the lattice structure in which the atoms are found) and the other accounts for the chemical energy of the different elements involved. The energy of formation then is the sum of the value found for each atom in the structure.

To motivate the study, the BFS Model calculations predict that both Ti and V should act as effective interlayers between Fe (overlayer) and Al (substrate) [1]. This prediction is arrived at by examining the energy of formation for the overlayer, interlayer and substrate elements as each is paired with the other two. Ti and V were found to share the same sub-grouping of elements which have a negative contribution to the formation energy in their interaction with Al as the substrate. The formation energy contribution from Al in contrast when paired with Ti and V, is positive. This same process was then repeated with Fe as the substrate instead of Al, which again placed Ti and V in the same subgroup with the same properties as in their interaction with Al. The main point then, is for an element to be an effective interlayer, it must have a likelihood to alloy with both the substrate and overlayer. On the flip side, both the substrate and the overlayer must each possess the property of non-likelihood to alloy with the interlayer. Finally, the total energy of formation must be negative, indicating the likelihood of alloying for the three-element system. The

interlayer therefore acts as the bond to keep the overlayer and substrate together in the 'sandwich'.

Our group in the past performed a study on the Fe-Ti-Al interlayer system and concluded that a thin layer of Ti is indeed an effective interlayer between Fe and Al [7, 9, 10]. It was concluded that Ti and Al in the surface layers form bonds that effectively stiffen the surface to prevent the Fe overlayer from diffusing into the Al substrate. A theoretical study by D. Spišák and J. Hafner [11] addressed this same system using density functional theory (DFT) calculations and concluded that for the clean Al(001) substrate, there is no diffusion barrier to Fe, but with a Ti-alloyed surface, a barrier is created to prevent the diffusion of Fe into the Al(001) substrate. The question that this study addresses then is whether V can be considered as effective an interlayer as Ti.

The focus of this thesis is to study the interaction of the pair of elements in the first part of the interlayer process, that is studying separately the surface characteristics of Ti on Al(001), and repeating the same study with V. The greater emphasis of the work consisted of using LEIS as a surface-structure sensitive technique. Using LEIS was motivated by a sabbatical stay in our lab by Dr. Dae Sun Choi from Korea. He made use of his expertise in LEIS to examine the structural properties of the surface layers of the Ag-Al(001) system [12]. Before his return to Korea, we began looking at Ti on Al(001). The use of LEIS was minimal in the lab up to the time of his visit, so with his work, LEIS became the main thrust of my thesis work. The use of LEED also played a major role in determining the surface characteristics of the Ti-Al and V-Al systems. The results of this study allowed us to conclude whether V can be considered as an interlayer of the caliber of Ti.

An introduction to our study would not be complete without a mention of the applications of a surface study such as this. The study of interlayers in the 1980's was

motivated by the desire to improve the characteristics of magnetic storage technology used in personal computer hard drives. The physics upon which this technology is based is found in GMR (giant-magneto resistance). Metals possessing this property experience a change in resistance in the presence of an external magnetic field. The media of a hard disk consists of two thin layers of metals placed together, one magnetic and the other non-magnetic. The process of alloying at the interface between these two metals, adversely affects the required properties needed for proper operation. The introduction of an interlayer is a solution to the problem, allowing the two metals to retain their pre-alloy properties integral in the storage process.

The study of Ti on the Al(001) surface has applicability in research for chemical storage of hydrogen in solid materials such as sodium alanate ($NaAlH_4$). Ti has been examined as a potential catalyst on the surface of the alanate to encourage the reaction needed for the storage process [13]. A more detailed overview of this topic will be presented in Chapter 8.

1.3 List of Acronyms

BFS Bozzolo-Ferrante-Smith Method for Alloys

LEED Low-Energy Electron Diffraction

LEIS Low-Energy Ion Scattering spectroscopy

MCS Multi-Channel Scaling

PHA Pulse Height Analysis

RGA Residual Gas Analyzer

RBS Rutherford Backscattering Spectroscopy

TFM Thomas-Fermi-Molière

TM Transition Metal

UHV Ultra High Vacuum

CHAPTER 2

NEW UHV CHAMBER

2.1 Design of New UHV Chamber

A new UHV chamber to study the structure of transition elements deposited on the Al(001) surface, was designed and contracted for construction to *NorCal Products, Inc.* The design phase was begun in the summer of 2006. Figure 2.1 shows the chamber drawing set sent to the manufacturer. The chamber was designed with numerous available ports to accommodate all spectroscopic equipment supported by the old chamber, with a generous placement of spare ports for visual inspection and connection of potential peripherals.

Plans were sent to the manufacturer and construction was completed with delivery in July 2007 to the Ion Beams Lab at Montana State University. Figure 2.2 shows the chamber soon after initial delivery, mounted on a stand constructed by Norm Williams. The photo also shows the chamber ion pump with gate valve mounted to the bottom port and a mass spectrum analyzer unit connected at right for use in vacuum testing.

Initial vacuum testing of the chamber revealed a small vacuum leak at a main chassis seal near the top 8" conflat flange. The chamber was returned to the manufacturer for repair. Upon successful completion of vacuum testing, installation of the various spectroscopic instrumentation, peripherals, and pumping systems was begun.

The chamber was put into operation in January 2008. Initial testing of the experimentation systems was performed on a clean Al(001) crystal which had been used in the old chamber.

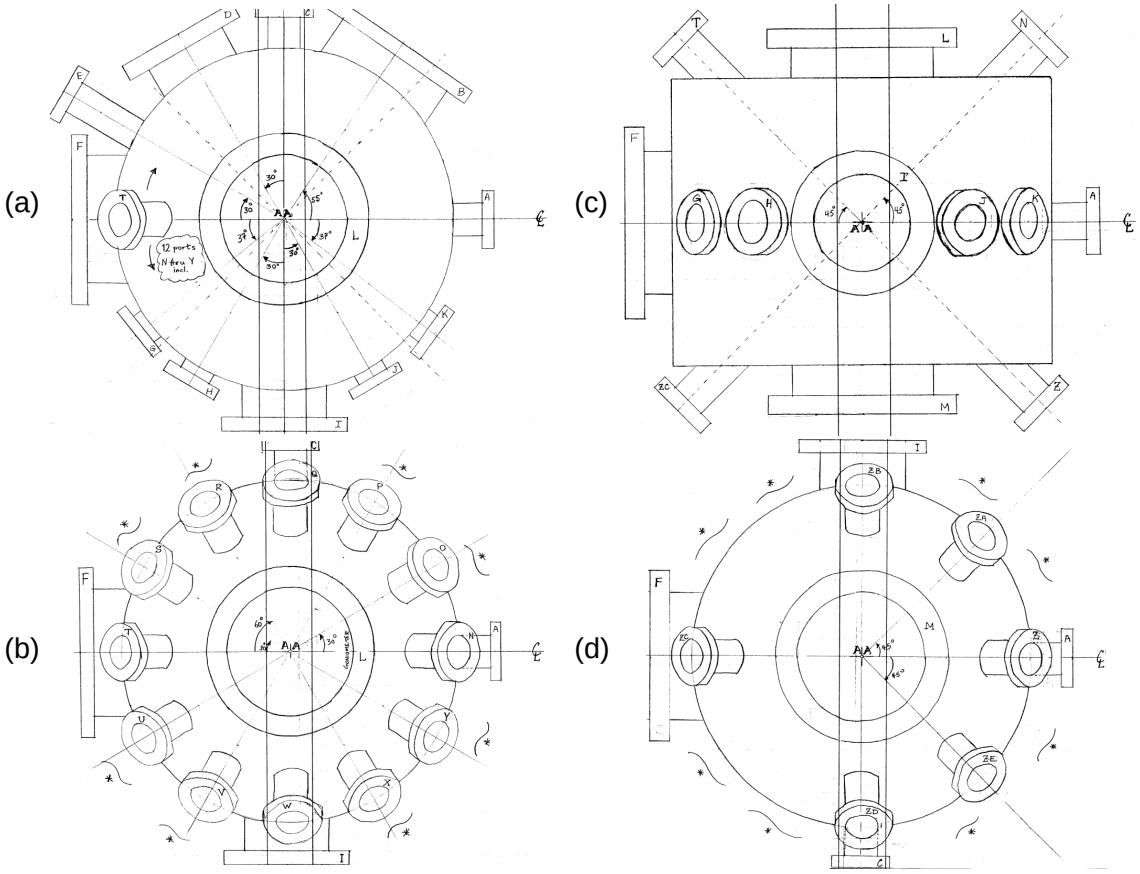

Figure 2.1: New UHV chamber drawings, each showing the beam line connection port to the right. (a) top view - side port detail, (b) top view - top port detail, (c) side view, (d) bottom view - bottom port detail.

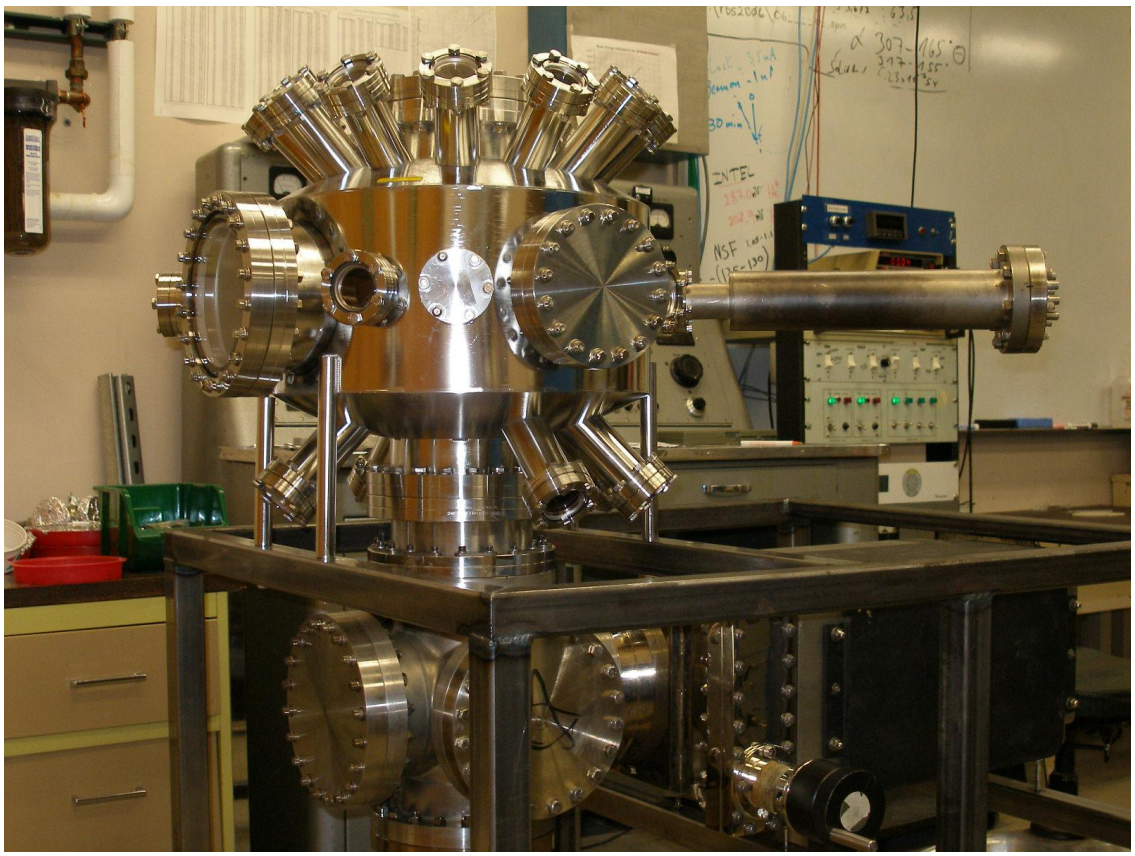

Figure 2.2: Newly constructed UHV chamber mounted on stand before initial vaccum testing.

2.2 Motivation

The construction of a new chamber was motivated by the desire to simplify the scattering geometry used in the previous UHV chamber. The previous geometry placed the electrostatic analyzer for LEIS out of the plane formed by the incident ion beam and the surface normal of the Al(001) crystal. This scattering geometry is called Cornell [14] geometry, a term used in ion-beam scattering experimentation. Figure 2.3 depicts the various unit direction vectors and angles in Cornell geometry.

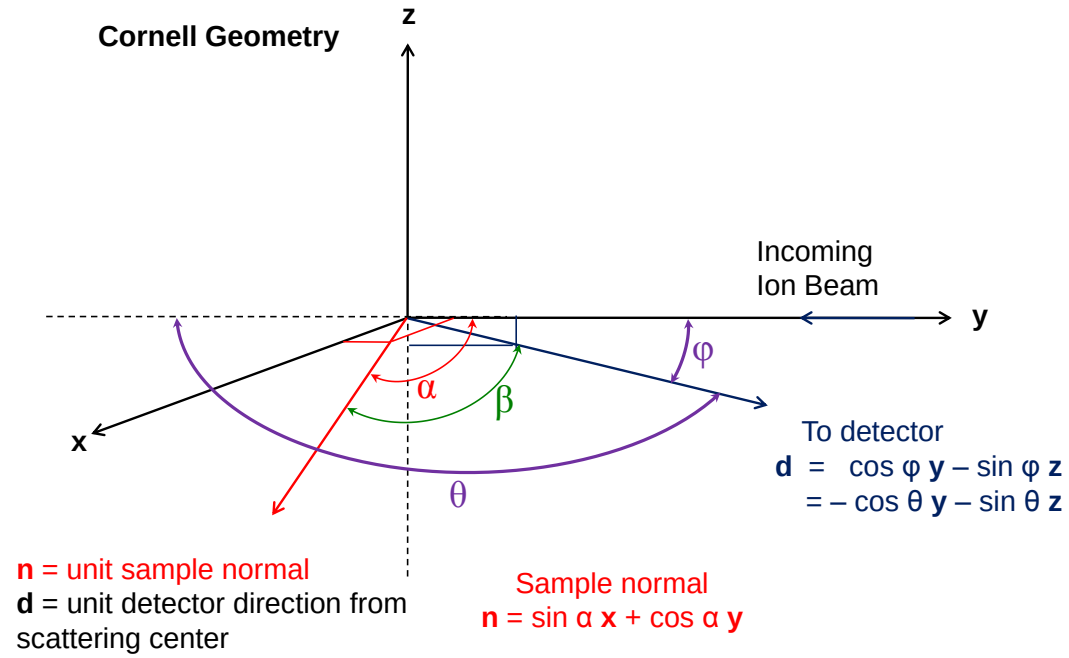

Figure 2.3: Cornell scattering geometry.

The scattering geometry relations are

$$\begin{aligned} \hat{n} &= \sin\alpha\,\hat{x} + \cos\alpha\,\hat{y} \ \text{ and} \\ \hat{d} &= \cos\phi\,\hat{y} - \sin\phi\,\hat{z} = -\cos\theta\,\hat{y} - \sin\theta\,\hat{z}. \end{aligned} \tag{2.1}$$

The angle between the sample normal $\hat{n}$ and the the direction vector $\hat{d}$ along the line joining the sample scattering center and the detector, is β. The angle β can be found using the expression $\hat{n} \cdot \hat{d}$ giving $\cos\beta$ which evaluates to

$$\cos\beta = -\cos\theta \ \cos\alpha. \tag{2.2}$$

LEIS spectra obtained in the old chamber gave results dependent on the added complication of a 3-D versus a simpler 2-D scattering geometry. This complicated spectra analysis. Hence we were motivated to construct a chamber that put the incident ion beam and detected scattered ions in the same plane, i.e. the horizontal plane of the laboratory floor. The corresponding ion-scattering analysis geometry is called IBM [14] geometry and is depicted in Figure 2.4.

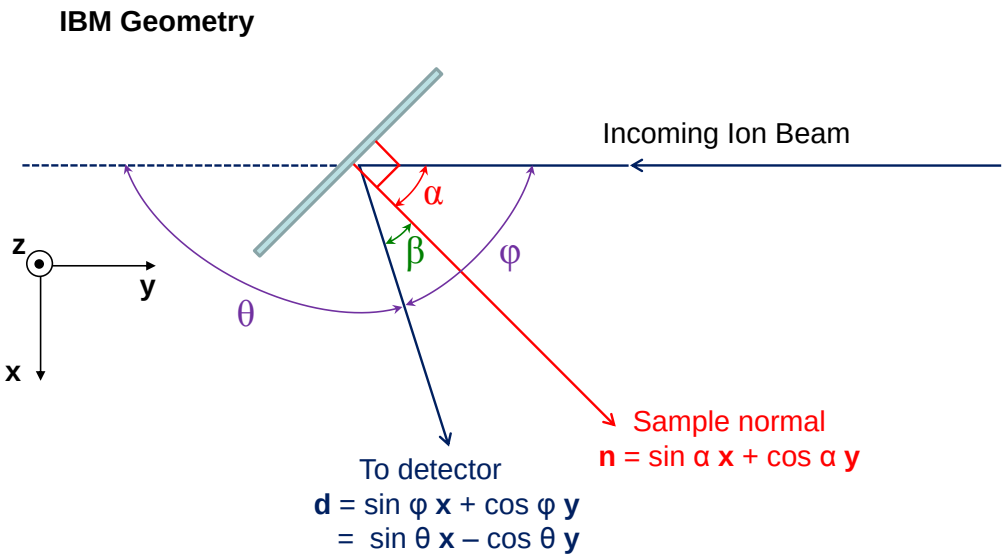

Figure 2.4: IBM scattering geometry.

Here the expression for β is greatly simplified and can be found directly from the geometry to be

$$\beta = |\pi - \theta - \alpha| \,. \tag{2.3}$$

We take an absolute value since from the argument alone, β can be positive or negative depending on whether α (the angle that the incoming ion beam makes with the sample normal) is greater or less than ϕ (the angle between the incoming ion beam and the detector).

2.3 Experimental Techniques

Here we list the experimental systems supported in the new chamber as well as some supporting peripheral equipment.

- RBS (Rutherford Backscattering Spectrometry). The chamber has a connection through a differentially pumped beam line to a 2 MV van de Graaff accelerator, giving RBS capability for determining deposited thin-film coverage on the sample surface.

- LEIS (Low Energy Ion Scattering Spectrometry). The LEIS system is comprised of a 100 mm hemispherical electrostatic energy analyzer (VSW HA-100) and controller (VSW HAC-5000), and an ion gun (3M Minibeam Ion Gun) and associated control unit (3M 430) with a raster/gate supplementary unit connected. The scattering angle for LEIS between the ion gun and analyzer is 150°. The LEIS system was configured in the ion-detection mode during the experiments.

- RGA (Residual Gas Analyzer). The composition of the chamber residual gas was assessed using an electrostatic gas analyzer system (Dycor M100M Quadrupole Gas Analyzer).

- LEED (Low Energy Electron Diffraction). The LEED system consists of a reverse-view optics instrument (Princeton Research Instruments Inc., Reverse View LEED Optics RVL 8-120) with controller (Perkin Elmer 11-20 LEED Electronics).

- Elemental e-beam evaporator for vanadium deposition (Focus GmbH).

- Elemental evaporative filament for titanium deposition. Ti deposition onto the Al(001) crystal surface was accomplished via evaporation using a resistively heated wire filament, composed of three W wires (0.2 mm in diameter) braided together, and then wrapped with a Ti wire (0.25 mm in diameter).

- UHV (Ultra-high vacuum) Pumping System. A base pressure of 5×10^{-10} Torr was maintained by an 8" flanged ion pump (Varian Noble Triode Pump 912-7014, pumping speed of 220 l/s) with control unit (Varian 921-0066). LEIS or sputter sample cleaning was done under a He^+ or Ar^+ environment maintained at a pressure of $\sim 10^{-8}$ or 10^{-6} Torr respectively using a 6" flanged turbo pump (Pfeiffer-Balzers TPH240) with pumping speed of 230 l/s, backed up by a mechanical pump (Varian DS402).

Figure 2.5 is a photo of the new chamber in operation installed on the beam line.

2.4 Goniometer Sample Positioning Device

A schematic of the ion-scattering geometry for LEIS and RBS is depicted in Figure 2.6. Varying the polar angle allows sample rotation about the $\hat{y}$ axis, varying the azimuth angle allows rotation about the $\hat{z}$ axis, and a third degree of movement not shown allows for varying the tilt angle about the $\hat{x}$ axis. Also shown is the path of a high energy ion from our linear accelerator towards our sample for RBS studies.

Figure 2.5: New UHV chamber in operation installed on the beam line.

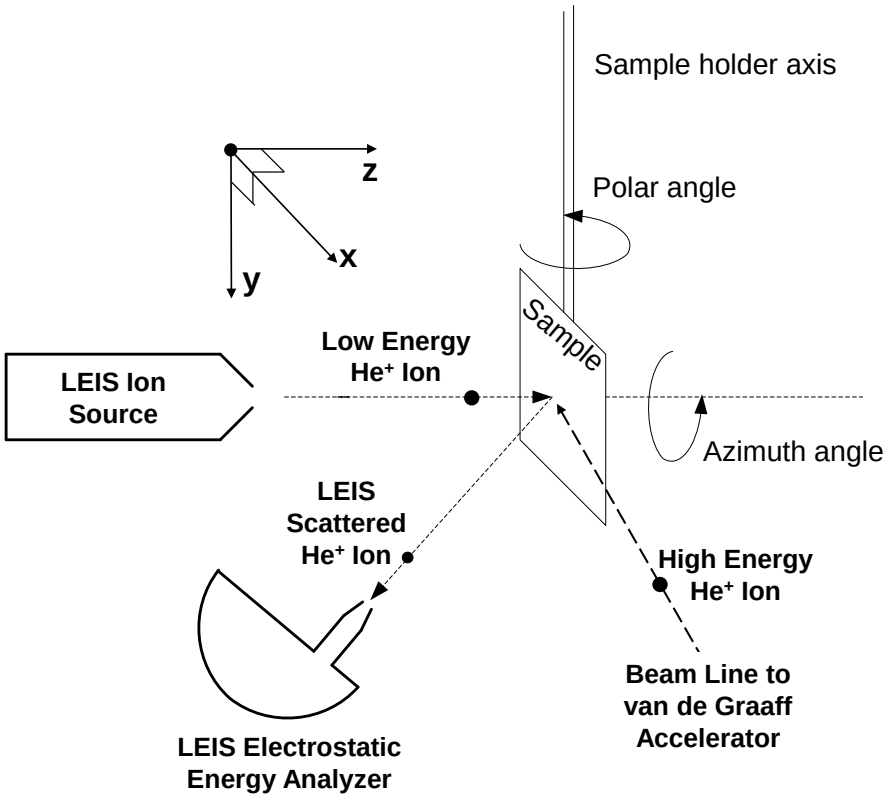

Figure 2.6: Schematic of the chamber scattering geometry.

To vary the angles described in the ion-scattering geometry, the chamber is equipped with a high precision 3-axis goniometer for sample positioning. Figure 2.7 shows a photograph of the goniometer from various orientations. Figure 2.7(a) shows the full goniometer sitting inverted on a stand. The sample holder is at the top of the photo and three rotatable shafts with gear mechanisms are shown at the bottom which allow the operator to vary the three axes of movement. Figure 2.7(b) is a photo of the front view of just the sample holder and its relation to the concentric ring support which gives it the freedom of movement. The outer ring is the azimuth angle adjust, center ring is the tilt angle adjust and central ring has no freedom of movement but is secured to the tilt ring at initial mechanical mounting. Figure 2.7(c) shows the view of the goniometer assembly that resides inside the chamber and a back view of the sample holder. Figure 2.7(d) is a similar view as in (c) but instead a front view of the sample holder.

The sample, an Al(001) crystal, is approximately 10 mm in diameter and is mounted in the goniometer sample holder. The sample holder also contains a resistively heated W wire filament for annealing and a Pt-resistor thermometer to monitor sample temperature, both mounted directly underneath the sample-holder surface. Figure 2.8 shows the sample mounted in the sample holder inside of the new UHV chamber. In the photo a portion of the LEED optics screen is at left, and at right we see portions of the electrostatic hemispherical analyzer unit and the LEIS ion gun.

2.5 Old versus New Chamber LEIS Spectra

Upon collection of LEIS spectra, we compared the quality of the data collected from the old chamber with that from the new chamber. Here we present a sampling

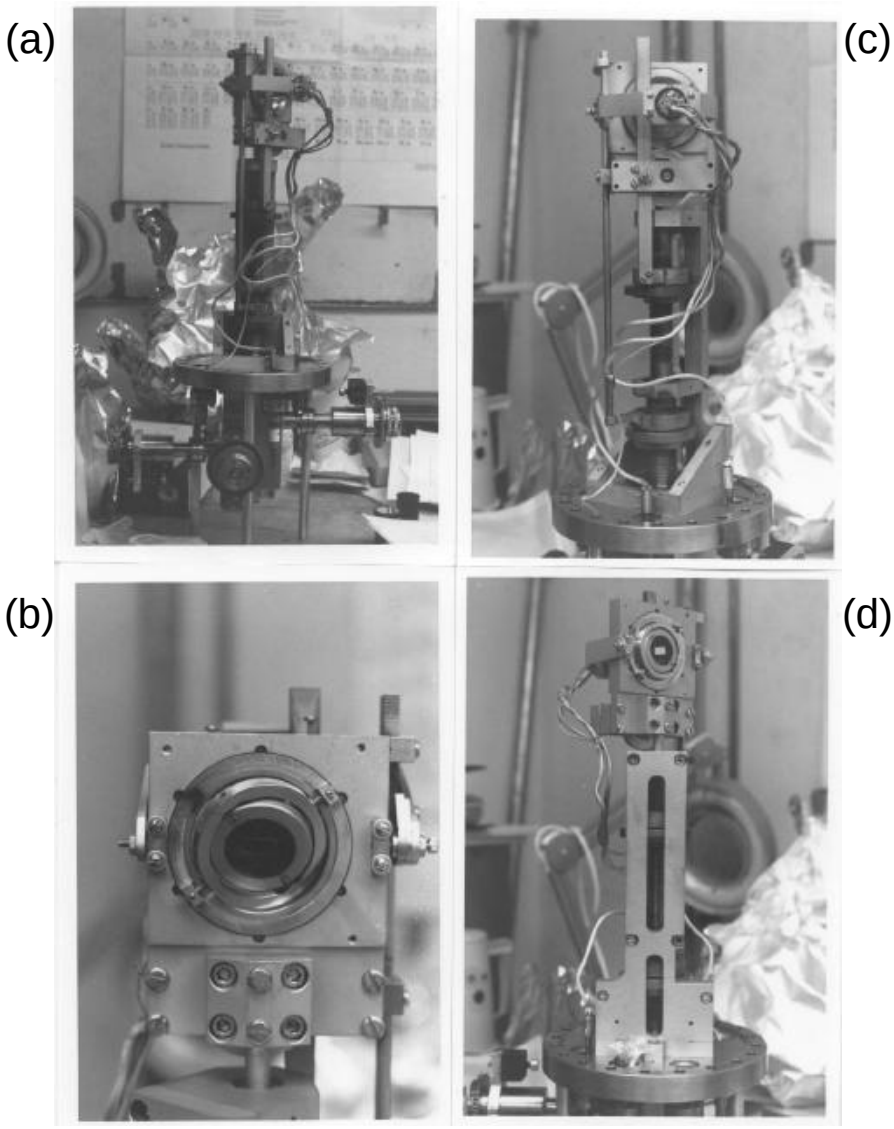

Figure 2.7: Three-axis positioning goniometer used in the new UHV chamber. (a) Full view. (b) Sample holder 3-axis movement concentric-ring assembly. (c) Goniometer section that resides in the chamber, back view of sample holder. (d). Goniometer section that resides in the chamber, front view of sample holder.

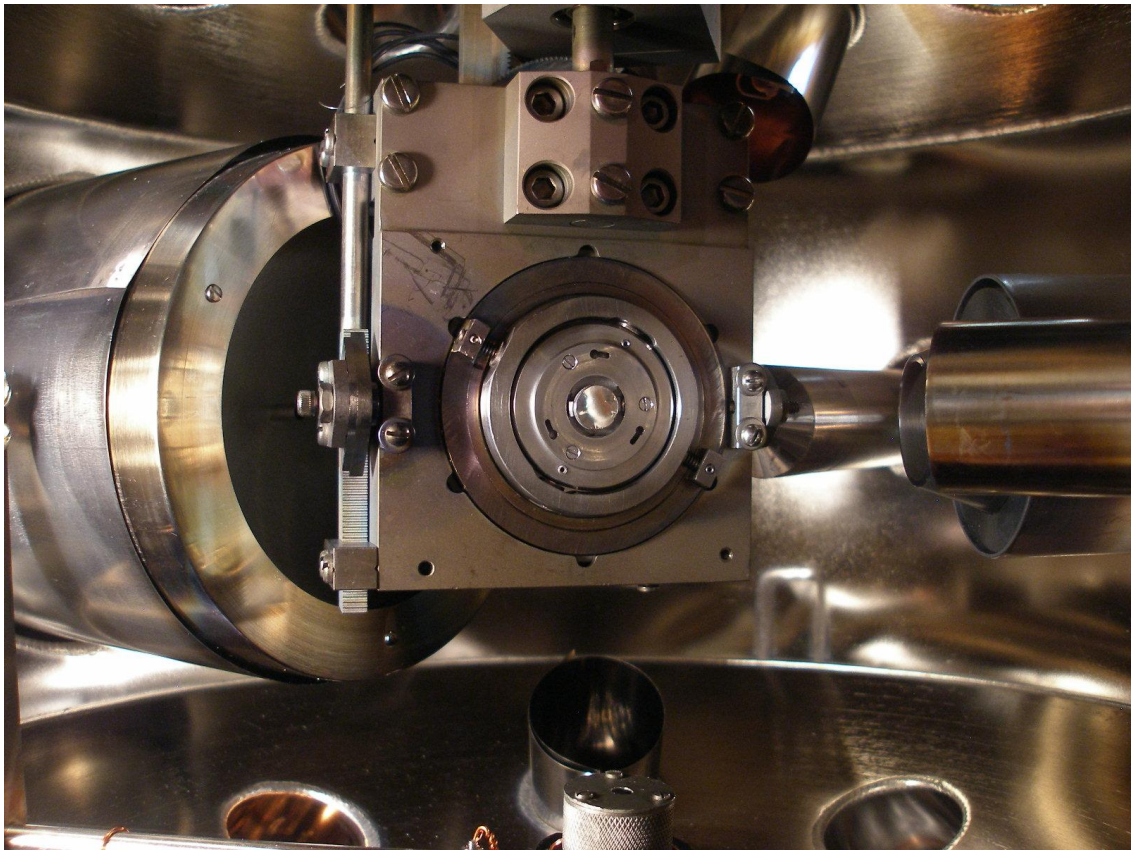

Figure 2.8: Al(001) crystal sample mounted on the goniometer sample holder as installed inside the new UHV chamber.

of LEIS polar angle scans (details of these spectra will be covered in the section dedicated to LEIS).

Figure 2.9 shows two sets of LEIS polar angle scans collected in the (a) [100] and (b) [110] azimuth directions for our cleaned and annealed Al(001) crystal. The solid line plots are the spectra from the old chamber that we were using as a standard and the dashed line plots are the corresponding spectra collected in the new chamber. The data shown were plotted using a 25-point Adjacent-Averaging smoothing method provided in the *Origin* graphing software package (v.8.0, *OriginLab Corporation)*. The difference between the old and new sets was quite pleasing to us, as LEIS analysis necessitates that peaks in the spectra be reasonably distinctive.

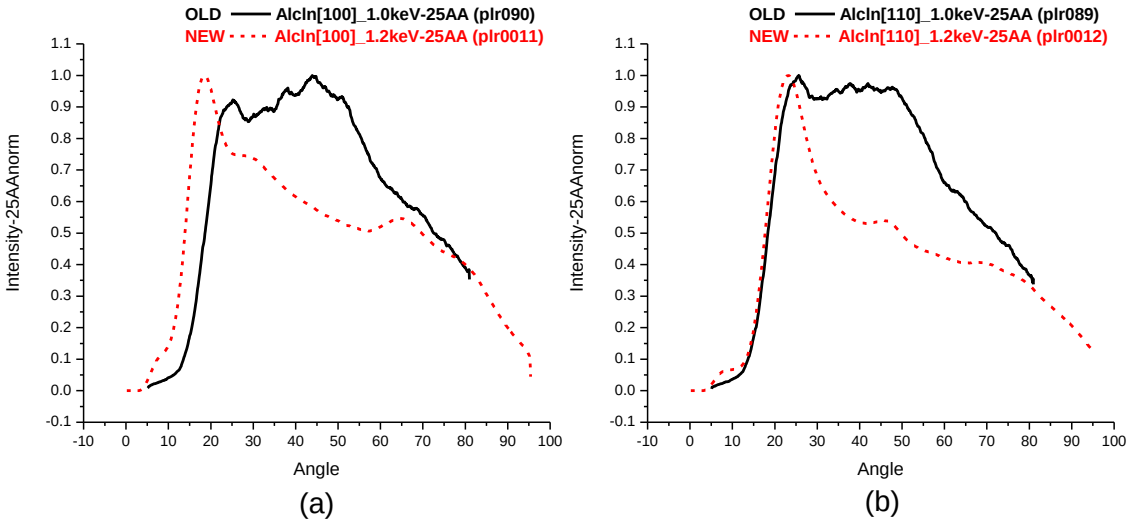

Figure 2.9: LEIS polar angle scan spectra comparing those collected in the old chamber to those from the new UHV chamber. (a) [100] azimuth. (b) [110] azimuth.

During LEIS data collection in the old chamber, another set of clean Al(001) scans in the two azimuths was collected as shown in Figure 2.10. The Al(001) sample for this set was Ar^+ sputter cleaned but not annealed yet a very crisp LEED pattern was displayed. These data appear to give a better match to the corresponding spectra

collected in the new chamber compared to the previous old set, when considering only general shapes and peak placements.

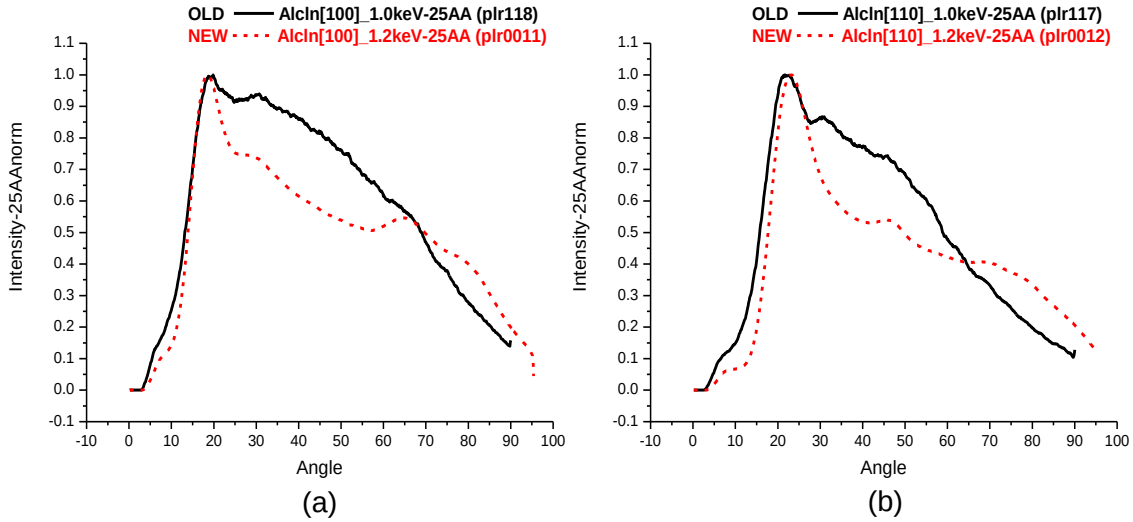

Figure 2.10: Another set of LEIS polar angle scan spectra comparing those collected in the old chamber to those from the new UHV chamber. (a) [100] azimuth. (b) [110] azimuth.

The quality of the spectra collected in the new chamber is much better than that from the old chamber, as peaks are more distinct. The distinct peaks observed aided our geometrical shadow-cone analysis, the details of which will be covered in the section on LEIS.

CHAPTER 3

RBS

3.1 Introduction to RBS

Rutherford Backscattering Spectroscopy (RBS) is a spectroscopic technique consisting of elastic collisions between incident light ions and heavier target atoms to determine target composition and concentration-depth profiles. A complete treatment of RBS would include the particulars for the kinematic factor, absolute angular scattering cross section, straggling and stopping power. For our work, RBS was used to measure the deposition coverage of Ti and V on the Al(001) surface. Thus only an understanding of the kinematic factor and scattering cross section were needed and our treatment will be limited to these two.

Incident ions in RBS have energies in the range of MeV (He^+ ion velocities on the order of 10^7 m/s), and can penetrate several microns (10^{-6} m) into the bulk of a target.

To perform RBS, we need a source of energetic ions focused into a beam. High energy ions are generated in a van de Graaff accelerator at energies of $\sim$ 1 MeV and directed outward through a beam line connected to an UHV chamber containing a target to be analyzed. In our setup, multiple vacuum chambers can receive the accelerator ion beam which is directed to the desired line via a bending magnet located at the output port of the accelerator.

RBS was used in our study to analyze the elemental composition of our sample from the perspective of determining the thickness of the deposited transition metal (TM) thin films Ti and V onto our Al(001) crystalline metal substrate.

In order to find deposited film thickness we directed a He^+ ion beam at a nominal energy of 1.3 MeV to the sample surface and counts of backscattered ions were collected using a silicon surface barrier detector positioned at a backscattering angle of 112°. The sample surface normal was oriented at approximately 22° with respect to the ion beam to minimize channeling effects. The counting electronics was configured in the pulse height analysis (PHA) mode, which yields a spectrum of counts as a function of channel number. The abscissa is calibrated in units of energy. As backscattered ions enter the detector, the counting electronics places a count into the proper channel of the spectrum dependent on the energy of the ion detected.

Determining the RBS *yield* for the deposited element is part of elemental composition analysis and leads to a value for the deposition thickness. The meaning of kinematic factor and absolute scattering cross section are important foundations which will be covered as an introduction to the yield calculation.

3.2 RBS Elemental Composition Analysis

3.2.1 Kinematic Factor

Figure 3.1 depicts a schematic of a binary collision between an incident light ion such as He^+ of mass M_1 and incident energy E_0 with a stationary heavy target atom of mass M_2. The scattered ion leaves the collision at the scattering angle θ and energy E_1. The target atom recoils at angle φ and energy E_2.

The *kinematic factor* K is expressed in terms of the incident ion energy E_0 and corresponding backscattered energy E_1 by the following relation

$$E_1 = K\,E_0. \tag{3.1}$$

Since the backscattered energy of the ion is always less than that for the incident ion, K must be in the range $0 < K \leq 1$. In RBS we treat the collision dynamics

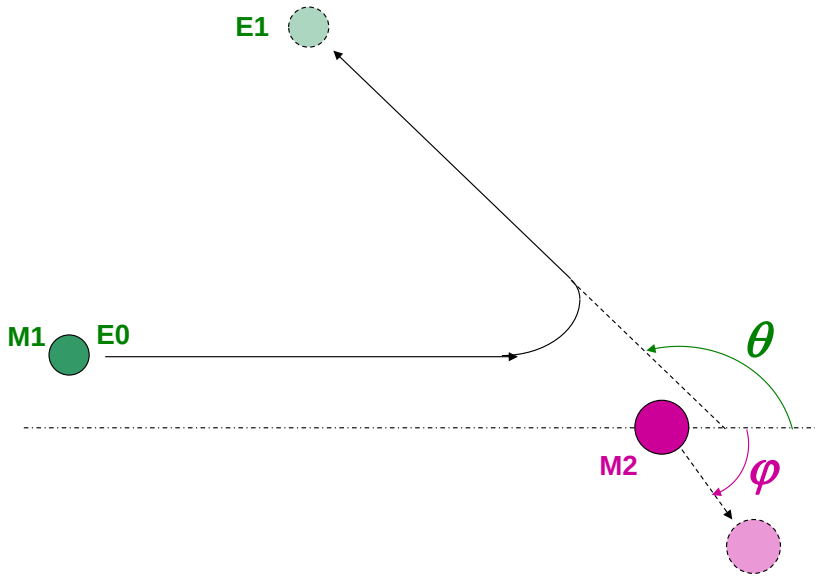

Figure 3.1: Scattering geometry for RBS.

between the ion and target atom as an *elastic* binary collision. Thus we use conservation of energy together with conservation of momentum to arrive at a quantitative expression of the kinematic factor K as a function of the scattering angle θ and the ion and target atom masses M_1 and M_2 [15] which gives

$$K = \frac{\mathrm{E}_1}{\mathrm{E}_0} = \left(\frac{\frac{M_1}{M_2}\cos\theta \pm \sqrt{1 - \left(\frac{M_1}{M_2}\sin\theta\right)^2}}{1 + \frac{M_1}{M_2}} \right)^2 . \tag{3.2}$$

Note that K is a function only of θ, M_1 and M_2, and does not depend on the respective electric charge Z_1 and Z_2 of the particles.

3.2.2 Scattering Cross Section

In ion-target interactions, it is helpful to consider the probability of an ion entering a detector after having undergone an elastic collision with a target atom. This general concept is made quantitative by the value of the absolute angular scattering cross section $\sigma(\theta)$. The essential meaning of this quantity is an effective area surrounding

the target nucleus (central force field origin) causing an incoming ion projectile to deflect from its initial direction of travel. The greater the value of $\sigma(\theta)$ for a particular scattering angle θ, the higher the probability that an ion will scatter into this angle. These concepts translate into experiment by counting scattered ions that enter a detector positioned at this specific scattering angle. The ratio of the number of scattered ions detected to the total number of incident ions hitting a target substrate, is directly related to the absolute angular scattering cross section $\sigma(\theta)$.

First consider the angular differential scattering cross section $d\sigma(\theta)/d\Omega$. For an incident ion scattered by a target atom towards a detector into a differential solid angle $d\Omega$, the angular differential scattering cross section $d\sigma(\theta)/d\Omega$, is defined as [16]

$$\frac{d\sigma(\theta)}{d\Omega} \equiv \left\{ \begin{array}{l} \text{differential scattering cross section of a target atom} \\ \text{per differential solid angle } d\Omega \text{ for scattering an incident} \\ \text{particle at an angle } \theta \text{ into } d\Omega \text{ centered about } \theta \end{array} \right\}. \tag{3.3}$$

In the literature, there are many treatments for the derivation of the expression for $d\sigma(\theta)/d\Omega$ the differential scattering cross section per differential solid angle [15, 17, 18]. It is generally expressed as

$$\frac{d\sigma(\theta)}{d\Omega} = \frac{d\sigma(\theta, \mathrm{E}_0)}{d\Omega} = \left(\frac{Z_1 Z_2 e^2}{2\mathrm{E}_0 \sin^2\theta} \right)^2 \frac{\left[\cos\theta + \sqrt{1 - \left(\frac{M_1}{M_2} \sin\theta \right)^2} \right]^2}{\sqrt{1 - \left(\frac{M_1}{M_2} \sin\theta \right)^2}}, \tag{3.4}$$

where

$$\begin{aligned} Z_1 &= \text{atomic number of incident ion,} \\ Z_2 &= \text{atomic number of target atom,} \\ E_0 &= \text{energy of incident ion,} \\ M_1 &= \text{atomic mass of incident ion, and} \\ M_2 &= \text{atomic mass of target atom.} \end{aligned}$$

If we let the differential solid angle become finite $d\Omega \rightarrow \Omega$ to a typical value covering the surface area of a ion detector (this value is still relatively small $\sim 10^{-2}$ steradians), we can define an *average* scattering cross section per unit solid angle as [16]

$$\sigma_{ave}(\theta) \equiv \frac{1}{\Omega} \int \frac{d\sigma(\theta)}{d\Omega}\, d\Omega. \tag{3.5}$$

As a good approximation we can consider the probability of scattering incident particles from target atoms into the area of the detector as not varying much over θ since Ω, the solid angle of the detector, is relatively small. So $d\sigma/d\Omega$ throughout the detection area will essentially be the same and thereby approximately equal to an *average* scattering cross section per unit solid angle called $\sigma_{ave}(\theta)$, i.e.

$$\sigma_{ave}(\theta) \quad \simeq \quad \frac{d\sigma(\theta)}{d\Omega} \quad \simeq \quad \sigma(\theta). \tag{3.6}$$

Usually the descriptor *average* is dropped from the designation and $\sigma(\theta)$ is simply called the *scattering cross section*.

The cross section can be likened to the probability of scattering, with units of area expressed in *barns* (1 barn = 10^{-24} cm^2). To compare spectroscopic techniques, values for cross sections for RBS are typically in *barns* while for NRA (nuclear reaction analysis) the values are typically in *mbarns*, i.e. 1000 times smaller, and in contrast for LEIS the values are extremely large and typically about 10^6 *barns*.

To get a better sense of the size of $\sigma(\theta)$, we can model it as an effective *area* at whose center is the target nucleus. Using the area of a disk (πr^2), we can compare the radius r of this disk for these three spectroscopic techniques, and summarized in Table 3.1. These values are in the typical range for interactions between a He^+ and Al target nucleus.

Table 3.1: Comparison of radius r of disk with effective area of $\sigma(\theta)$ for three spectroscopic techniques.

$\sigma(\theta) \simeq$ **disk of area** πr^2		
Spectroscopy	$\sigma(\theta)$ **in *barns***	r **in Å**
NRA	10^{-3}	10^{-6}
RBS	1	10^{-4}
LEIS	10^{6}	0.1

With this background, let us turn to analyzing a typical RBS spectrum to find the yield as seen in our study as it relates to the thickness of a TM deposited onto our Al sample.

3.2.3 RBS Yield

Our discussion is motivated by the desire to find the thickness of a deposited elemental thin film on a crystalline metal substrate. A typical RBS spectrum for a sub-monolayer deposition of V on Al(001) is shown in Figure 3.2 showing the Al substrate plateau and a tiny V peak at a higher energy. For more detail the inset figure shows the V peak re-scaled. The kinematic factor for V is greater than that for Al due to its greater mass. This puts its peak to the right of the Al rising edge. For the Al crystal, backscattered ions undergo more of an energy loss the deeper they penetrate the sample, thus these form a plateau on the spectrum, whose right edge is from ions with the most energy, scattered from the surface. The V peak on the other hand, resembles a gaussian since it is a thin layer.

Let us now consider *RBS yield*. The total counts detected corresponding to the deposited element is obtained by integrating the area under its corresponding surface peak in the RBS spectrum. This is defined as the *yield* for that element and we call it A_{sp}. The following expression allows us to determine the thickness of the deposited

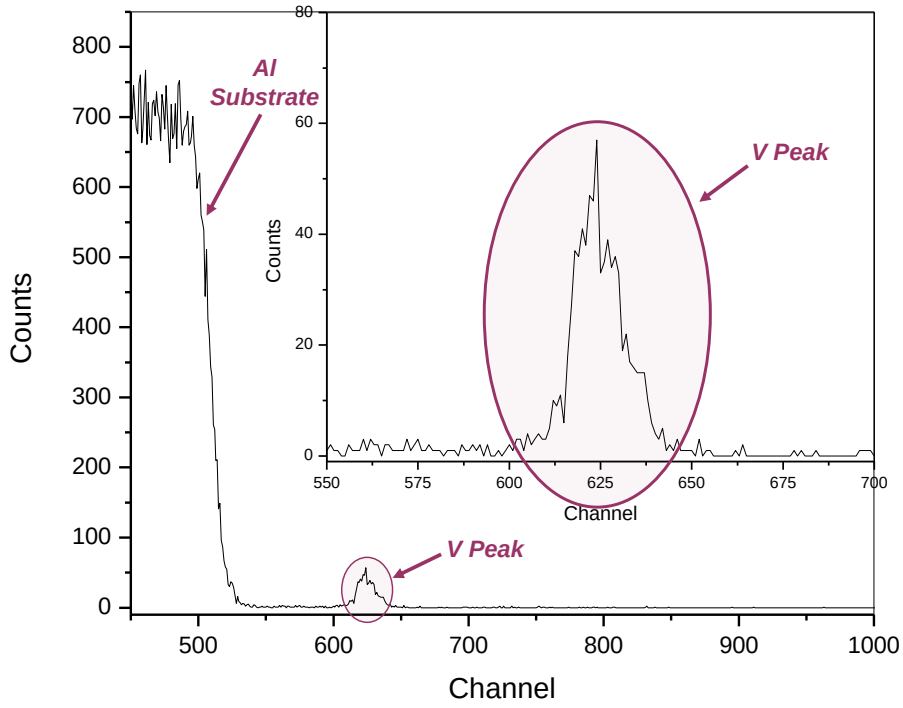

Figure 3.2: RBS spectrum for 2.5 ML V on the Al(001) surface.

element,

$$A_{sp} = \mathrm{Y}\ (yield) = Q_{det} = Q_{inc}\,\sigma\,\Omega\,(Nt), \tag{3.7}$$

where

$$(Nt) = A_{sp}/(Q_{inc}\,\sigma\,\Omega). \tag{3.8}$$

(Nt) is the value for the areal density for the deposited elemental thin film. The specific terms are

$$\begin{aligned} Q_{det} &= \#\text{ of scattered ions detected,} \\ Q_{inc} &= \#\text{ of incident ions,} \\ \sigma &= \text{average scattering cross section per unit solid angle,} \\ \Omega &= \text{solid angle of detector,} \\ N &= \text{atomic volume density in \# atoms/cm}^3\text{ for target atoms,} \end{aligned}$$

$$t = \text{linear thickness of thin film (cm), and}$$

$$(Nt) = \text{TM atomic areal density in \# atoms/cm}^2 \text{ for film atoms.}$$

Let us verify the *units* of (Nt).

$$[(Nt)] = \left[\frac{A_{sp}}{Q_{inc}} \cdot \frac{1}{\sigma} \cdot \frac{1}{\Omega}\right]$$
$$= \left[\frac{\text{\# detected ions}}{\text{\# incident ions}} \cdot \frac{\text{(solid angle)}}{\text{area}} \cdot \frac{1}{\text{solid angle}}\right].$$

The ratio of detected counts to incident ions gives a pure number fraction leaving the units of (Nt) as atoms per area, as expected.

In Figure 2.3 depicting Cornell [14] scattering geometry, the angle between the incident ion beam and surface normal is designated as α. The above expression for (Nt) assumes that the incoming ion beam is at normal incidence to the sample surface for the case where $\alpha = 0$, which is a common practice. Our sample has an ordered structure such that the value for the yield can be affected by the incoming ion beam channeling in the empty space between rows of atoms in the crystal. To avoid this the orientation of the sample is adjusted by making α non-zero. Thus the expression for (Nt) must account for this and becomes

$$(Nt) = \cos\alpha \; A_{sp}/(Q_{inc}\,\sigma\,\Omega) \tag{3.9}$$

It is convenient to express TM deposition thickness in terms of the number of layers of the element put down onto the sample surface. In order to do this we reference this value to the areal density of atoms in the substrate. The term *monolayer* (ML) is the unit of measure used where 1 ML *for the Al(001) crystal substrate* is

$$1 \text{ ML } (Al(001)) = \text{areal density of } \; 1.22 \times 10^{15} \text{ atoms/cm}^2. \tag{3.10}$$

Therefore, (Nt) can be expressed in ML units as a direct comparison with that of 1 layer of atoms in the Al(001) substrate. This terminology will be used throughout the discussion when referring to coverage of Ti or V on Al(001).

CHAPTER 4

LEIS

4.1 LEIS - Introduction and Theory

4.1.1 Overview and Comparison with RBS

Low-energy Ion Scattering Spectroscopy (LEIS) spectra, as in Rutherford Backscattering Spectroscopy (RBS), consist of counts of backscattered ions incident on target atoms in some sample material. Incident ions in RBS have energies in the range of MeV (He^+ ion velocities on the order of 10^7 m/s), while in LEIS the corresponding energies are in the keV range (He^+ ion velocities on the order of 10^5 m/s).

With RBS one detects backscattered particles whether they remain as ions or become neutralized in the collision process. RBS detected backscattered ions can originate from atomic layers far beneath the target surface and still achieve detection either as ions or as neutrals. The type of detector used in LEIS determines whether neutrals and ions or just ions are detectable. In our setup, we use an electrostatic energy analyzer which is sensitive only to backscattered ions which remain in the ionized state. Ion-neutralization probabilities are very high for both the incident-incoming and backscattered-outgoing paths of the ion projectile, which makes LEIS a highly surface sensitive technique [15, 19, 20]. Thus only the top few layers of the target sample surface are considered in the analysis of gathered spectra.

RBS and LEIS differ in another very important aspect. The interaction of the ion and target atom in the collision process in RBS is governed by a Coulomb potential, since incident ions at MeV energies can penetrate the electron shells of target atoms and interact directly with the nucleus. The low energy incident ions in LEIS however, see a target nucleus screened by the inner shell electron clouds and thus

the collision dynamics must take into account a screened-Coulomb potential. This makes the calculation of the absolute scattering cross section in LEIS very complicated compared to the relatively straightforward calculation in RBS. The relative ease of determining the absolute scattering cross section in RBS makes it a useful technique to quantitatively determine the thickness of elemental thin films deposited onto a substrate surface, whereas LEIS cannot be used for this purpose. Furthermore such quantitative analysis in LEIS is limited by the lack of knowledge of the neutralization probability of the backscattered ion as mentioned above.

Conversely, LEIS is a useful technique when surface sensitivity is required in analyzing both the elemental composition and structural morphology of surface layers. Three types of LEIS spectra can be collected. These are the energy scan, azimuth-angle and polar-angle scan spectra. We will use the term *scans* interchangeably with the term *spectra* and the *-angle* descriptor may be dropped for simplicity. Energy scans are used to determine elemental composition of the sample surface layers while azimuth and polar scans give us information regarding the structural makeup of the surface layers. These will be covered in more detail after presenting some groundwork information needed to support analysis of these spectra.

4.1.2 Al(001) Crystal Coordinate System

For analysis of LEIS spectra, especially for LEIS azimuth- and polar-angle scans, it is useful to define the coordinate system in which we represent our Al(001) crystal lattice. In Figure 4.1 we depict the 3-dimensional schematic of a clean Al-*fcc* lattice whose surface is the (001) plane.

We define the x, y and z axes to be respectively in the [100], [010] and [001] directions with respect to the Al(001) surface plane as shown in Figure 4.1. The [100] and [110] azimuth directions are in the plane of the sample surface and the [001]

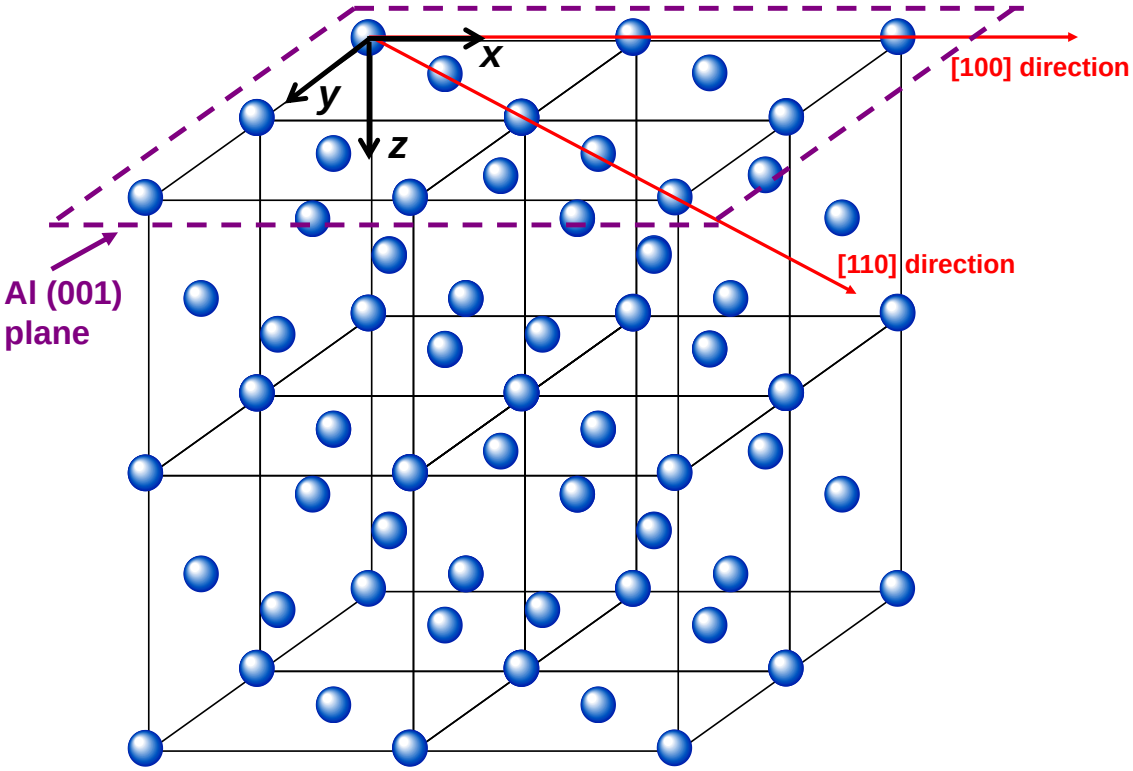

Figure 4.1: Three-dimensional representation of the Al crystal *fcc* lattice with a characteristic Al(001) surface plane.

direction points into the bulk. Note the direction vectors shown for the [100] and [110] directions are perpendicular to the {100} and {110} families of planes. We will use the [100] and [110] directions to define the azimuth angle setting of the crystal face. The orientation and geometry of the Al(001) surface plane as referenced to these low-index azimuth directions is the foundation of the analysis of LEIS azimuth-angle scan spectra. Similarly the orientation and geometry of the Al{100} and Al{110} family of planes are at the heart of analysis of spectra collected for LEIS polar-angle scans.

4.2 LEIS Experimental Setup

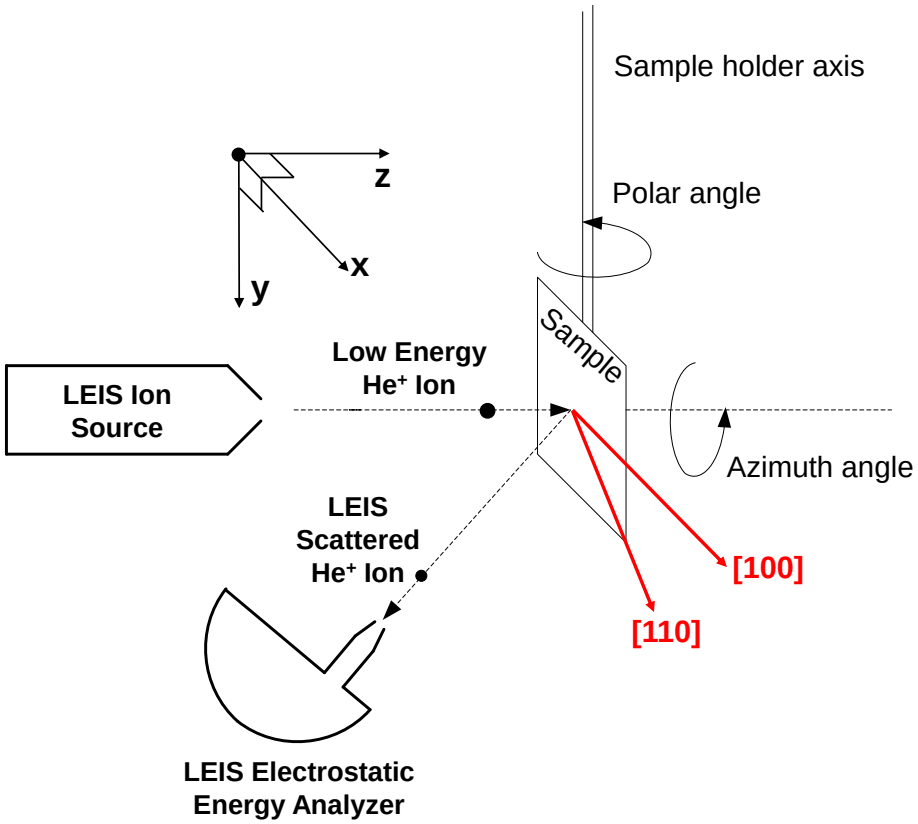

Figure 4.2: LEIS experimental setup schematic.

Figure 4.2 shows a schematic of our experimental LEIS setup depicting the scattering geometry for LEIS. Depending on instrument configuration, LEIS energy scans, azimuth- or polar-angle scans can be collected. We have previously defined a coordinate system describing the orientation of our Al(001) crystal substrate. Applying this to our experimental setup sample geometry in our UHV chamber, places the plane formed by the incident ion beam from the He^+ ion gun and its corresponding backscattered ion flux as it enters the electrostatic analyzer, parallel to the lab floor which we will call the horizontal plane. In our LEIS study, the Al(001) sample crystal surface plane was always perpendicular to the horizontal plane of the lab floor. Sample rotation about the $\hat{z}$ axis varies the azimuth angle and sample rotation about the $\hat{y}$ axis varies the polar angle. For our discussion, counter to usual convention, we define the polar angle as measured with respect to the sample surface plane rather than with respect to the surface normal. A third degree of movement not shown allows for varying the tilt angle about the $\hat{x}$ axis, which was not used in our LEIS experiments.

LEIS experiments were done in an ultra-high vacuum (UHV) chamber equipped with a high precision 3-axis goniometer for sample positioning. The sample, an Al(001) crystal, has an approximate diameter of 10 mm and is mounted in the goniometer sample holder. Transition metal (TM) elemental deposition onto the Al(001) crystal surface was accomplished either using an evaporative process using a resistively heated wire filament or via an e-beam evaporation system. The chamber also has a connection through a differentially pumped beam line to a 2 MV van de Graaff accelerator, giving RBS capability for determining deposited thin-film coverage on the sample surface.

As depicted in the schematic, LEIS uses an ion gun with associated controller. LEIS is configured in the ion-detection mode and is accomplished using a 100 mm hemispherical electrostatic energy analyzer (VSW HA-100) which contains a high

gain *Channeltron* electron multiplier which receives the detected ions and provides the corresponding signal to the counting electronics. The counting electronics consists of a multi-channel analyzer configured in the multi-channel scaling (MCS) mode. In this mode, the channel 'bins' contain counts of detected backscattered ion events. The channels are scanned beginning at the first, one after another to the last channel (usually 1024 in total), until a full spectrum is collected. For energy scans, the channels are calibrated in units of energy. For azimuth and polar scans, channels are calibrated in units of angle corresponding to specific orientations of the sample surface with respect to the incident ion beam. The scattering angle between the ion gun and analyzer was 150°. LEIS was conducted using a He^+ incident ion beam at nominal energies of 1.0 or 1.2 keV and chamber He^+ pressure of approximately 5×10^{-7} Torr. Ion currents were kept relatively low in order to minimize the damage to the sample surface which occurs from sputtering by the incident He^+ ion beam.

4.3 Binary-Particle Collision Dynamics in LEIS

In this section we will introduce primary topics in LEIS, including the kinematic factor, yield and scattering cross section, the screened-Coulomb potential, and the concept of the shadow cone.

4.3.1 Kinematic Factor

The scattering geometry in LEIS is similar to that in RBS (see Figure 3.1). A binary collision occurs between an incident light ion such as He^+ of mass M_1 and incident energy E_0 with a stationary heavy target atom of mass M_2. The scattered ion leaves the collision at energy E_1. As in RBS, we also treat such interactions as *elastic* collisions. Because the kinematic factor K, as we defined for RBS (see

Equation 3.2), does not depend on the electric charge Z_1 and Z_2 of the particles, we can use the same relation to describe the binary collision in LEIS, namely $\mathrm{E}_1 = K\,\mathrm{E}_0$.

4.3.2 LEIS Yield and Scattering Cross Section

The non-dependence on the charge Z of either particle makes the kinematic factor K the same for RBS and LEIS. The scattering cross section however, is dependent on the charge of the interacting particles. The binary collision dynamics in LEIS is governed by a screened-Coulomb potential. This effectively modifies the magnitudes of the charge of the particles in regards to the collision interaction. Thus determining the scattering cross section in LEIS is not a straightforward calculation.

In RBS the ion and target nucleus interact directly since the electron cloud of the target nucleus has little effect on the incoming ion's trajectory due to its relatively high incident energy and corresponding high magnitude of velocity. In LEIS however, the energy of the incoming ion is low enough so that its trajectory is affected by the electron cloud of the target atom, so simply using the Z values of the ion and target nuclei is incorrect since the target nucleus is screened by its inner shell electrons. Thus in examining the ion-target collision dynamics in LEIS, numerical methods must be employed, for instance to find the scattering angle that the ion undergoes in a collision event. Numerous researchers have proposed analytical expressions for screening functions applied to the Coulomb potential to simplify calculations. This topic will be addressed later.

Determining the yield in LEIS is not a clear cut calculation as the yield depends upon the scattering cross section $\sigma(\theta)$. In addition, the atoms of the deposited species may reside in layers below those visible to LEIS. Furthermore, incident-ion neutralization probabilities for the visible layers (at or just below the surface) are dependent upon the incoming ion angle of incidence and upon the azimuth angle position of the

crystal surface [21]. Moreover, structure related effects due to shadowing and blocking, influence backscattered ion count intensities, especially in low-index azimuthal directions such as the [100] and [110] azimuths. These complications do however give LEIS a high level of surface sensitivity. Thus for determining quantitative metal deposition coverage we rely on RBS measurements. Nevertheless qualitatively, we get a sense of relative deposited metal coverage by using successive LEIS energy scans collected at similar parameter settings [22] from the rise in the intensity of the peak associated with the deposited metal as deposition continues.

4.3.3 Screened-Coulomb Potential

Our primary goal in examining the effects of a screened-Coulomb potential in ion-target collisions in LEIS is to obtain the value for the scattering angle of the ion having undergone such an event. In this section we present the supporting information required to attain this goal.

4.3.3.1 Overview of the Interaction Potential in LEIS:

In a two-body collision between an incoming energetic ion and a target atom in a crystal lattice, we must consider the separation distances between these two particles to understand the dynamics of the collision. Typical atomic distances of interest when working with collision dynamics are

$$\begin{aligned} a_0 &= 0.53 \text{ Å ; Bohr radius,} \\ a &\sim 3-4 \text{ Å ; lattice constant for typical crystalline metal,} \\ r_0 &\sim 2-3 \text{ Å ; nearest neighbor separation for typical crystalline metal.} \end{aligned} \tag{4.1}$$

Specifically for our Al(001) crystal

$$\begin{aligned} a &= 4.05 \text{ Å ; lattice constant for } \textit{fcc} \text{ Al, and} \\ \tfrac{a}{\sqrt{2}} &= 2.86 \text{ Å ; nearest neighbor for } \textit{fcc} \text{ Al.} \end{aligned} \tag{4.2}$$

For interactions between two atomic nuclei in the range where the separation distance $r \ll a_0$, the incident ion projectile does not 'see' the electron cloud surrounding the target nucleus. The collision dynamics between the two is thus governed by the standard Coulomb potential and is given by [16]

$$V(r) = \frac{Z_1 Z_2\ e}{r}, \tag{4.3}$$

where,

$$\begin{aligned} Z_1 &= \text{nuclear charge of the ion in multiples of } e, \\ Z_2 &= \text{nuclear charge of the target atom in multiples of } e \text{ , and} \\ e &= \text{charge on electron.} \end{aligned} \tag{4.4}$$

In the range where $r_0 \geq r > a_0$, the inner shell electrons of the target nucleus do influence the interaction dynamics in the collision. The electronic charge of the target nucleus is screened by its inner shell electrons making its nuclear charge appear to have a smaller value. We can model this screening effect by multiplying the standard Coulomb potential by another function that depends on the distance of separation between the atoms. We call this other function the *screening function* $\chi(r)$. The expression therefore for the effective potential of interaction becomes

$$V(r) = \left(\frac{Z_1 Z_2\ e}{r}\right) \chi(r). \tag{4.5}$$

Hence $V(r)$ is a *screened-Coulomb potential*. $\chi(r)$ should therefore modify the Coulomb potential properly for all values of separation distance between the incoming ion and target atom. Its value therefore in the extreme limits should be [16]

$$\begin{aligned} \chi(r) &\rightarrow 0, \text{ for large distances, and} \\ \chi(r) &\rightarrow 1, \text{ for very small distances.} \end{aligned} \tag{4.6}$$

4.3.3.2 Thomas-Fermi Screening Function $\chi(x)$: For our work in LEIS, the screening function we chose to describe the collision dynamics between an incoming ion and target atom, was based on the Thomas-Fermi statistical model. Nastasi, et al. [16] provide a good treatment in the derivation of this model. The TF screening function then is the solution of the dimensionless Thomas-Fermi (TF) differential equation and stated here for completeness

$$x^{\frac{1}{2}}\frac{d^2\chi}{dx^2} = \chi^{\frac{3}{2}}, \tag{4.7}$$

where a change of variables is made where $x = r/a$. The variable a is a quantity called the *screening radius* or *screening length*.

A typical numerical solution to the TF differential equation above is in the form of a series expansion. For values of $x \leq 0.44$, the solution is

$$\chi(x) = 1 + a_2 x + a_3 x^{\frac{3}{2}} + a_4 x^2 + \cdots = \sum_{k=1}^{\infty} a_k x^{\frac{k}{2}}. \tag{4.8}$$

This is called the Baker series and the coefficients are listed in the reference [16]. This solution is called the TF *screening function*.

To make use of the screening function, such a series solution is unwieldy and analytic approximations are sought which have sufficient accuracy in the regions of interest for typical values of r in collision events for LEIS. In our study, we chose an approximation to the TF screening function as derived by Molière. The Thomas-Fermi-Molière (TFM) approximation to the TF screening function has the form of three exponentials. We will refer to this expression simply as the TFM screening function which is given by [16]

$$\chi(x) = 7pe^{-qx} + 11pe^{-4qx} + 2pe^{-20qx}, \quad \text{where} \begin{cases} p = & 0.05 \\ q = & 0.3 \end{cases} \tag{4.9}$$

where $x = r/a$ is the dimensionless argument of the TF differential equation shown previously.

4.3.3.3 The Screening Length a: There are various expressions for the screening length [16]. One suggested by Bohr is

$$a_{\mathrm{B}} = \frac{a_0}{\left(Z_1^{2/3} + Z_2^{2/3}\right)^{1/2}}, \tag{4.10}$$

where a_0 is the Bohr radius and Z_1 and Z_2 are the atomic numbers of the atoms.

Lindhard suggested the form

$$a_{\mathrm{L}} = \frac{0.8853\ a_0}{\left(Z_1^{2/3} + Z_2^{2/3}\right)^{1/2}}. \tag{4.11}$$

Firsov suggested a value of

$$a_{\mathrm{F}} = \frac{0.8853\ a_0}{\left(Z_1^{1/2} + Z_2^{1/2}\right)^{2/3}}, \tag{4.12}$$

where 0.8853 is calculated from the Thomas-Fermi atom [16]. This value for the screening length is typically used in the TFM screening function.

To reach our goal of determining the scattering angle of an incident ion as a result of a collision event, we used the TFM screening function and a_{F} for the screening length. The concept of the *shadow cone* must be examined to arrive at a value for the scattering angle.

4.3.4 The Shadow Cone

Critical to analysis of LEIS azimuth- and polar-angle scan spectra is an understanding of shadow-cone dimensions and parameters. Figure 4.3 depicts a 2-dimensional schematic cutout of a shadow cone (which is a 3-dimensional object) produced from the scattering of an incident ion from a target atom.

Due to the Coulomb type interaction of incident ions with target atoms, ions are scattered at angles dependent upon the impact parameter of each incident ion

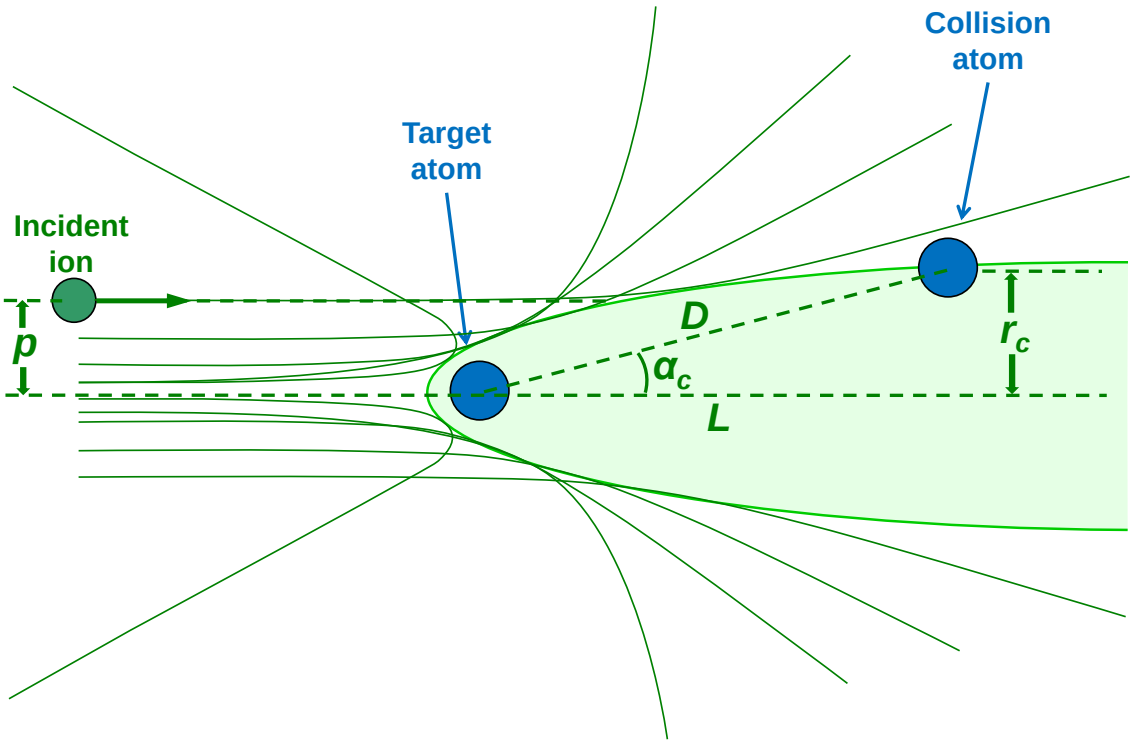

Figure 4.3: Schematic of shadow cone.

trajectory, shown as p in the figure. In our LEIS experimental setup, we have an ion flux incident on a crystal substrate surface. This gives a distribution of impact parameters p, and each incident ion scatters at a unique angle with respect to its incoming direction. This process produces a volume around the ion's target atom which is empty of incident ions, called the *shadow cone*. The ions that would have been in this empty space, are now displaced to the region of the shadow cone boundary. This is called the *focusing effect*. By changing the angle of the incident ion beam with respect to the sample surface, this shadow cone boundary moves in such a way as to form atom interaction pairs, i.e. as the higher concentration of incident ions at the shadow cone boundary intersects another atom in the substrate, the target atom is 'paired' with this other atom in the collision process. The paired atom, called the collision atom, is located in the wake of the shadow cone boundary. In the figure, the target and collision atoms are shown separated by a distance D. Due to the focusing effect, as the shadow cone boundary intersects collision atoms, an increase in the number of detected backscattered-ion counts will result, thus giving rise to corresponding peaks in collected LEIS angular spectra. If sample orientation places whole ordered rows of lattice atoms within the shadow cone, substantially less target-collision atom pairs are formed, dropping the number of detected backscattered ion counts, and resulting in valleys in the spectra. This is referred to as the shadow-cone *shadowing effect*.

LEIS azimuth and polar scans are spectra of backscattered ion counts vs. the corresponding sample orientation angle controlled by the goniometer. Insight into at what angle to expect peaks in azimuth and polar scan spectra comes from a knowledge of the critical angle α_c as seen in the figure. The critical angle α_c is the angle between the target atom's shadow-cone axis and the line joining the target atom to the center of the circle whose circumference lies along the shadow-cone boundary of radius r_c,

at which point a potential collision atom may reside. Our goal is to determine α_c for specific target-collision atom pairs.

Crucial to finding α_c is knowledge of the geometrical parameters of the shadow cone, such as its radius r_c, which in turn are functions of element type and distance from the target atom. We used equations given by O. S. Oen [23] whose work derives universal shadow cone expressions for atoms in an ion beam, to find the needed parameters. In his work, Oen derived empirical formulas for calculating the critical shadow-cone radius r_c and critical impact parameter s_c (notation by O. S. Oen) for a binary collision between an incoming ion and a target atom. The expressions are as follows:

- Critical Shadow-cone Radius r_c

$$\frac{r_c}{2\sqrt{bL}} = \begin{cases} 1.0 - 0.12\alpha + 0.01\alpha^2 & ; \quad 0 \leq \alpha \leq 4.5 \\ 0.924 - 0.182\ln\alpha + 0.0008\alpha & ; \quad 4.5 \leq \alpha \leq 100 \end{cases} \tag{4.13}$$

- Critical impact parameter s_c

$$\frac{s_c}{\sqrt{bL}} = \begin{cases} 1.0 & ; \quad 0 \leq \alpha < 0.6 \\ 1.03 - 0.04\alpha + 6 \times 10^{-6}\alpha^4 & ; \quad 0.6 \leq \alpha < 10 \\ 1.093 - 0.1785\ln\alpha & ; \quad 10 \leq \alpha \leq 100 \end{cases} \tag{4.14}$$

where

$$\begin{aligned} \alpha &= \tfrac{2\sqrt{bL}}{a} = \text{ dimensionless parameter,} \\ a &= \text{ screening length,} \\ b &= \sqrt{\tfrac{Z_1 Z_2 e^2}{E}}, \\ L &= \text{ distance from target atom along the axis of the} \\ &\quad \text{shadow cone perpendicular to the line marking } r_c. \end{aligned} \tag{4.15}$$

The critical angle α_c follows then from the relation

$$\alpha_c = \tan^{-1}\left(\frac{r_c}{L}\right). \tag{4.16}$$

In geometrical shadow-cone analysis, predictions can be made for the appearance of peaks in both azimuth- and polar-angle scan spectra by considering the known distance D between a chosen target atom and collision atom in the Al-*fcc* crystal-lattice substrate. The distances D and L, shown in Figure 4.3, are involved in an iterative calculation to arrive at a value for α_c. Thus we can compare the location of peaks in our experimental azimuth and polar LEIS scans with predictions we get from calculations of α_c.

The value found for α_c gives us a good indication of where to expect peaks in our LEIS angular spectra. However, due to the nuances of ion-target binary collisions [24], the actual experimental spectrum peaks occur slightly after the point where α_c marks the intersection of the shadow-cone boundary with the collision atom. Results of research in the field places α_c as occurring at the angle corresponding to a point at 50–80% of the amplitude of leading edge of the experimental peak [19, 24, 25, 26]. A reasonable percentage of this amplitude to use is 80% [25].

4.4 LEIS Spectra

Three types of spectra are collected in LEIS, the *energy* scan, the *azimuth-angle* scan and the *polar-angle* scan. Each has its particular purpose and method of analysis of spectral counts.

Energy scans are used to determine elemental composition of the sample surface layers while azimuth- and polar-angle scans give us information as to the structural morphological makeup of the surface layers.

4.4.1 LEIS energy scans

Energy scans depict counts of backscattered ions plotted as a function of the ion's energy, the ordinate being counts and the abscissa in units of energy. In our experimental setup, He^+ ions are incident on our sample at energies in the range of 1.0–1.2 keV. The analyzer acceptance energy is swept approximately from 300-1000 eV and counts of backscattered ions are recorded. This results in a spectrum of counts vs. backscattered ion energy and shows peaks at energies corresponding to ions backscattered from Al atoms from our sample, and other elements which are present in the surface layers resulting from the TM deposition process. The backscattered ions are at energies determined by the kinematic factor K of the backscattered He^+ ion from each respective element in the target. The value of the kinematic factor K (see Equation 3.2) for a given incident ion mass, increases as the mass of the target atom increases. Qualitatively, the height and width of each peak will correspond to the relative amounts of the elements present in the surface layers.

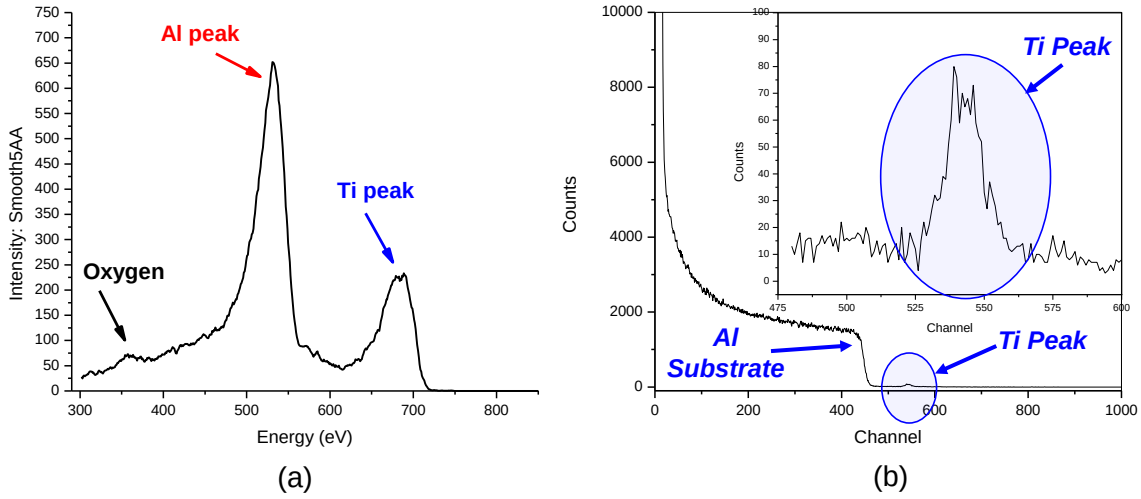

Figure 4.4: (a) LEIS energy scan post Ti deposition onto Al(001) surface. (b) Corresponding RBS spectrum used to determine Ti coverage at 0.8 ML.

Figure 4.4 shows typical LEIS and RBS spectra collected from our sample after the deposition of Ti atoms onto the Al(001) crystal substrate. Since Ti is a heavier atom, its corresponding value for K will be greater than the respective value for Al. We therefore find in both spectra a peak corresponding to Ti at a higher energy than a peak collected from ions backscattered from Al atoms. Fig. 4.4(a) depicts a LEIS energy scan post Ti deposition onto the Al(001) surface. The corresponding RBS spectrum is shown in Fig. 4.4(b) which was used to calculate the Ti coverage at 0.8 ML.

4.4.2 Azimuth-angle Scans

When the acceptance energy of the hemispherical-electrostatic energy analyzer is fixed to correspond to the energy of ions backscattered from atoms of a particular element in our sample, we can collect LEIS azimuth- and polar-angle spectra to obtain information about the structural morphology of the surface layers. We have previously defined a coordinate system in which we represent our Al(001) crystal lattice to aid us in analysis of these spectra.

Refer to the experimental setup schematic in Fig. 4.2. In performing an LEIS azimuth angle scan, we fix the polar angle to a relatively small angle of incidence of ion beam with respect to the Al(001) surface plane. A typical value for this small angle is 12°. The sample surface azimuth angle is then changed at a regular rate where the range of the scan includes the [100] and [110] directions. At these major azimuth angle directions, we expect to see valleys in the spectrum due to the shadow-cone shadowing effect. In our experimental setup, we used either a DC motor to vary the azimuth-angle setting continuously, or incremented the setting manually. The azimuth angle was swept through a range of approximately 135°.

We used geometrical shadow cone analysis to examine results of experimental LEIS azimuth scans. A two-dimensional schematic of the Al(001) surface plane is shown in Figure 4.5(a). Surface atoms are represented by dark solid circles and 2nd layer atoms below the surface by light gray circles. Note the depiction of the two-dimensional slice of the shadow cone (not drawn to scale) created by the interaction of the incident He^+ ion with its initial target atom at the lower left corner. The focusing effect at the shadow cone boundary gives rise to a high density ion flux which can potentially intersect substrate paired collision atoms labeled a, b, c, d, e, g and h.

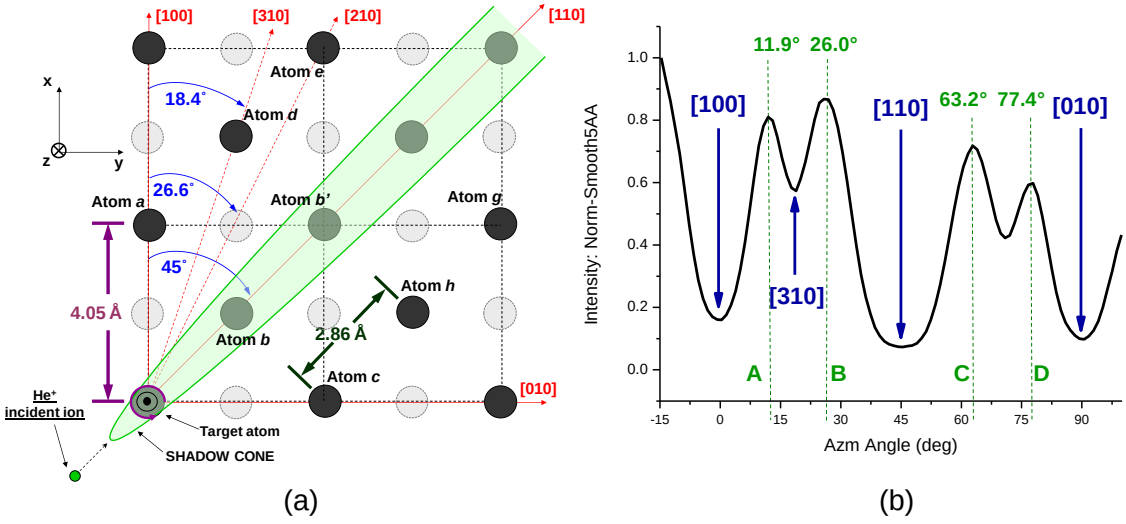

Figure 4.5: (a) Schematic of Al(001) surface plane. (b) Azimuth scan: Al-clean signal.

Figure 4.5(b) shows an azimuth scan of the clean Al(001) surface, the curve depicts counts of ions backscattered from Al atoms. Shown is the smoothed and normalized spectrum data. Valleys are labeled at the major low-index azimuth directions, which occur due to shadowing of Al atoms as they are arranged in rows in the crystal. Clear valleys in the spectrum are present in the [100], [110] and [310] azimuth directions.

As the azimuth angle changes, peaks appear as the higher concentration of incident ions at the shadow-cone boundary intersects collision atoms in the ordered rows of

the surface. The four dotted reference lines *A*–*D* mark the position of peaks in the Al-clean signal. Note also the clear four-fold symmetry of the Al-clean signal whose signal shape repeats every 90°.

The results of geometrical shadow-cone analysis are shown in Table 4.1 which lists the surface layer collision atoms from which the backscattered ions could originate. All entries in the table are based on the interaction of the incoming ion with the lower-left-most atom as target and origin of the shadow cone as depicted in Fig. 4.5(a).

Table 4.1: Al-clean azimuth scan, contributing surface layer collision atom for reference-line peaks. Refer to peak labels in Fig. 4.5(b).

Peak	**Contributing Surface-Layer Atom**
A	a, d
B	b, d
C	b, h
D	c, h

4.4.3 Polar-angle Scans

Polar-angle scans are collected by a similar method as done for azimuth scans, except now the azimuth angle is fixed with either the [100] or [110] azimuth direction vectors in the horizontal plane. The goniometer polar angle setting is varied using either a DC motor or incremented manually. The polar angle sweeps through a range of approximately 0° to 90°.

4.4.3.1 Polar Scan in the [100] Azimuth: Figure 4.6(a) depicts the Al(100) crystal plane at a side view of the crystal along the [100] azimuth. This plane is perpendicular to the crystal surface whose top row is made up of the surface atoms in the [100] azimuth direction.

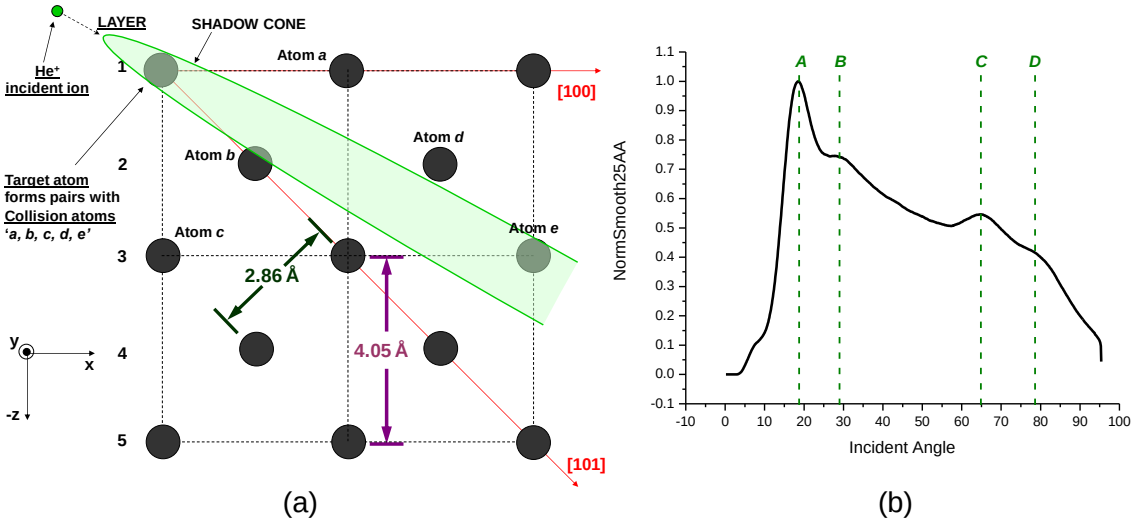

Figure 4.6: (a) Schematic of Al(100) plane perpendicular to crystal surface. (b) Polar scan along [100] azimuth: Al-clean signal.

At the left side of the figure are label references for the substrate layers beginning with the surface as layer *1*, and proceeding downward into the substrate bulk. Note also the depiction of the two-dimensional slice of the shadow cone (not drawn to scale) created by the interaction of the incident He^+ ion with its initial target (upper-left-most atom) located in the 1^{st} (surface) layer. The focusing effect at the shadow cone boundary gives rise to a high density ion flux which can potentially intersect substrate paired collision atoms labeled a, b, c, d and e.

In Figure 4.6(b) we show the resulting spectra from LEIS polar-angle scans taken in the fixed [100] azimuth. Shown is the smoothed and normalized spectrum data. Note the four dotted reference lines A–D located at the approximate position of major peaks or prominences in the Al-clean signal. Geometrical shadow cone analysis was used to analyze these peaks, the results of which are shown in Table 4.2 which lists the layer number and collision atom (in parentheses) from which the backscattered ions could originate. All entries in the table are based on the interaction of the incoming

ion with the upper-left-most atom as target and origin of the shadow cone as depicted in Fig. 4.6(a).

Table 4.2: [100] azimuth, contributing layer and collision atom for Al-clean scan reference-line peaks. Refer to peak labels in Fig. 4.6(b).

Peak [100]	**Contributing Layer & (Atom)**
A	1 (a); 3 (e)
B	2 (b, d)
C	2 (b)
D	3 (c)

4.4.3.2 Polar Scan in the [110] Azimuth: Figure 4.7(a) depicts a schematic of the Al(110) crystal plane. This plane is perpendicular to the crystal surface whose top row is made up of surface atoms in the [110] azimuth, in which direction the goniometer was fixed for this set of polar scans.

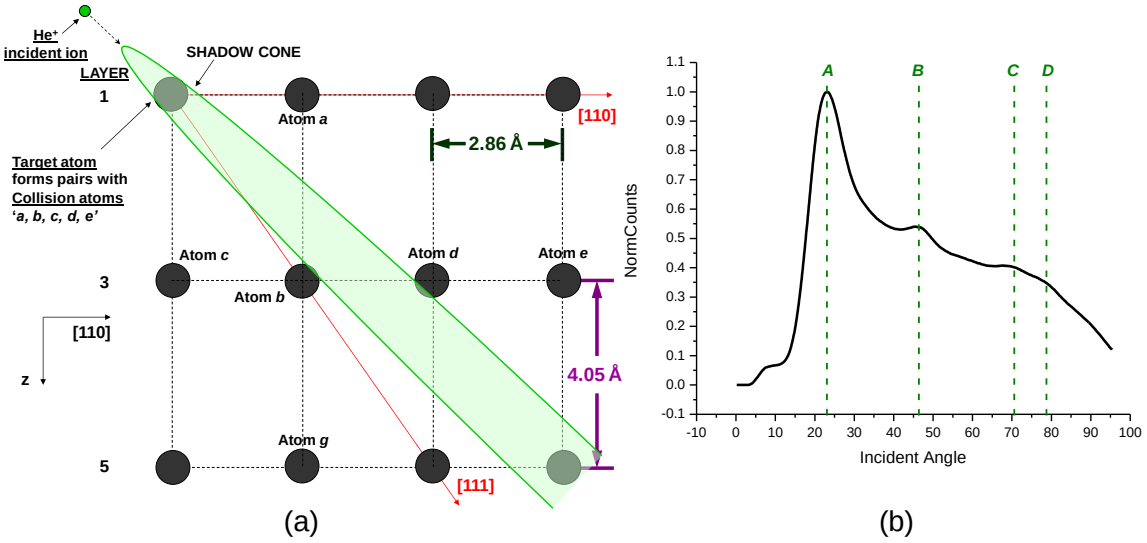

Figure 4.7: (a) Schematic of Al(110) plane perpendicular to crystal surface. (b) Polar scan along [110] azimuth: Al-clean signal.

Note the reference labels of the substrate layers at the left side of the figure. The surface layer is labeled *1* and the lower two layers are labeled *3* and *5* respec-

tively. When viewing the *fcc* crystal-lattice structure of Al, looking down onto the surface into the bulk along the surface [110] azimuth direction, the {110} family of vertical planes are comprised of atoms from odd-numbered or even-numbered layers. Figure 4.8(a) illustrates this concept. The (110) plane comprised of atoms from even-numbered layers (light-gray circles) is behind the (110) plane made of atoms (dark circles) from odd-numbered layers. The shadow cone is shown superimposed on the top row of atoms in this former plane (light-gray circles) in the 2^{nd} layer. Figure 4.8(b) is a depiction of two unit cells of the three-dimensional al-*fcc* lattice. Note the highlighted (110) plane (odd-numbered layer atoms) as seen in the $[1\bar{1}0]$ azimuth direction (equivalent structurally to the [110] azimuth direction) shows the top shadow cone shadowing its top row of atoms. The lower shadow cone in the 2^{nd} layer is shown shadowing the top row of the adjacent (110) plane made of even-numbered layer atoms. The main point here is that adjacent (110) planes are comprised of atoms having their top rows in either the 1^{st} or 2^{nd} layer giving the incident ion beam an equal probability of targeting either 1^{st} or 2^{nd} layer atoms. This will be a key point to our analysis when applied to polar scans for the Ti-Al and V-Al systems.

Figure 4.7(b), shows the smoothed and normalized Al signal resulting from an LEIS polar-angle scan in the [110] azimuth direction. A new set of reference lines *A*–*D* mark the positions of peaks and prominences in the Al-clean signal. For each reference line, Table 4.3 lists the contributing layers and corresponding collision atoms (in parentheses) from which backscattered ions could originate. All entries in the table are based on the interaction of the incoming ion with the upper-left-most atom as target and origin of the shadow cone as depicted in Figure 4.7(a).

The motivation behind the geometrical shadow-cone analysis covered in this chapter, is to understand the origin of peaks in LEIS azimuth and polar scans regarding which atoms in which layers in our sample substrate can contribute to such peaks.

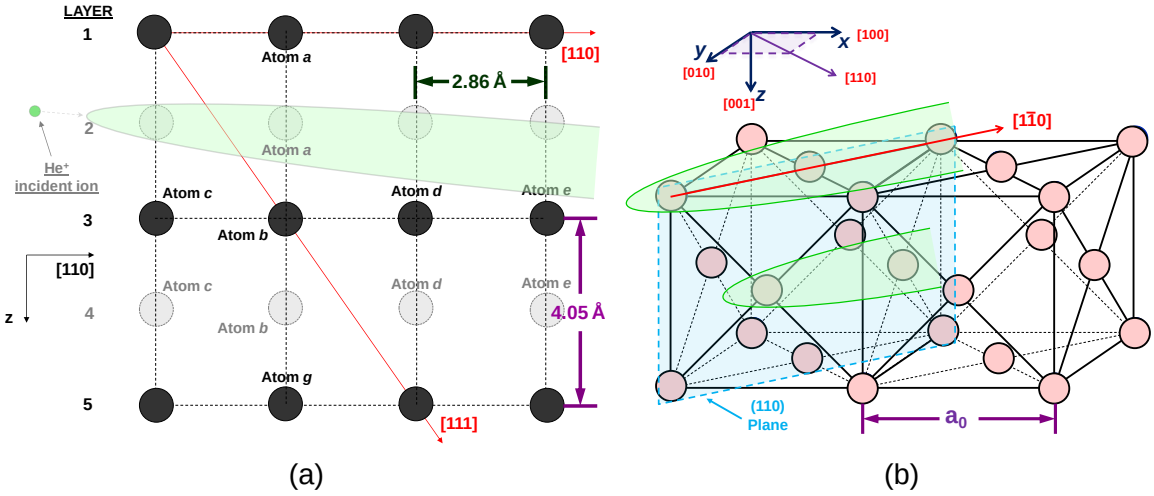

Figure 4.8: (a) Schematic of two (110) planes perpendicular to crystal surface, one with dark colored atoms and one with light-gray colored atoms. (b) Three-dimensional representation of the Al(001) crystal showing two unit cells.

Table 4.3: [110] azimuth, contributing layer and collision atom for Al-clean scan reference-line peaks. Refer to peak labels in Fig. 4.7(b).

Peak [110]	**Contributing Layer & (Atom)**
A	1, 2 (a); 3, 4 (d)
B	3, 4 (b, d)
C	3, 4 (b)
D	3, 4 (c)

Experimental azimuth- and polar-angle spectra we collect for the clean-Al(001) surface substrate are examined to see if corresponding peak locations agree with our geometrical calculations. These clean-Al(001) spectra then will then act as references to which we can compare corresponding spectra collected for post-TM deposition on the Al(001) surface.

CHAPTER 5

LEED

5.1 An Introduction to LEED

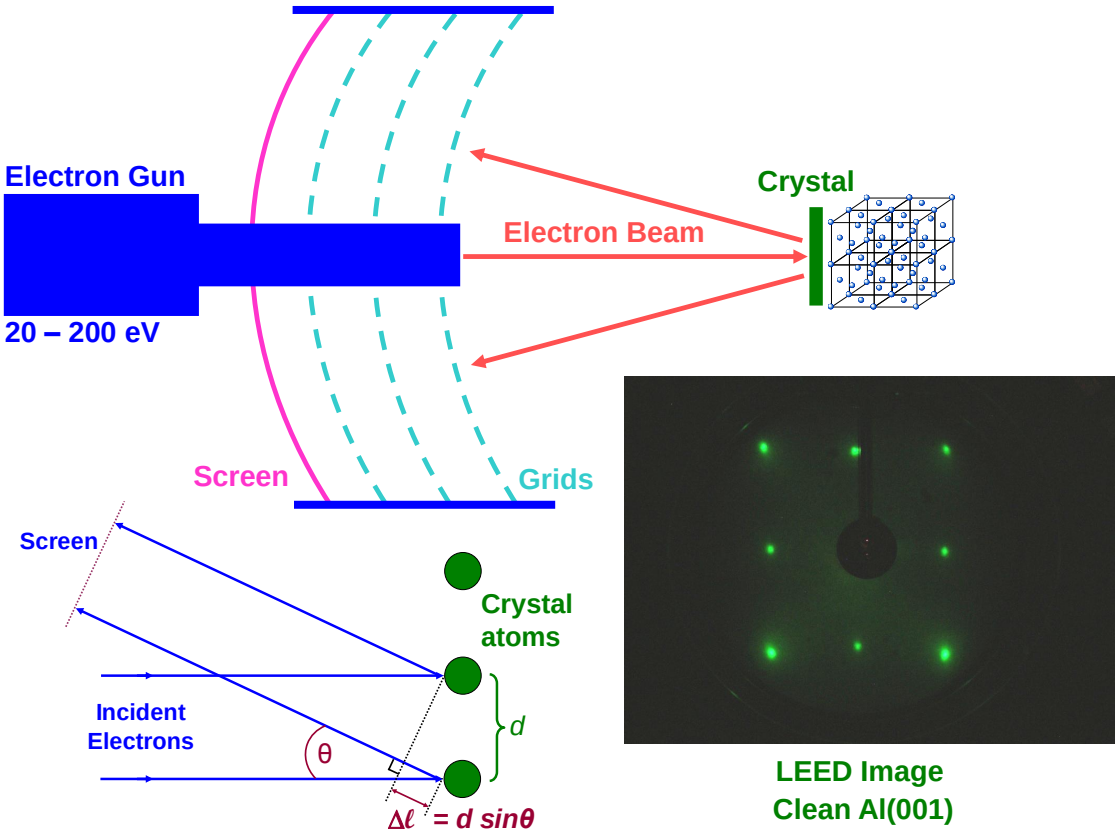

Figure 5.1: Schematic representation of a LEED system showing electron gun, filtering grids and phosphor screen. In the lower left corner is a representation of the Bragg law of diffraction. To the lower right is an actual LEED image for the clean Al(001) surface.

A schematic of a low-energy electron diffraction system (LEED) is shown in Figure 5.1. LEED is performed in a UHV chamber. The LEED mechanism is an electron gun which emits electrons monochromatically from a heated filament, focused into a beam and accelerated towards the sample under study which has a crystalline struc-

ture. The energy of the beam of electrons is in the range of 20–200 eV, adjustable by the operator. The collimated monochromatic beam of electrons incident on a crystalline target surface of atoms, backscatters as from point objects towards a phosphor screen whose center of curvature is located at the sample target. On their way towards the phosphor screen, the electrons are filtered by a series of 3–4 grids biased to allow only elastically scattered electrons to pass. The wave nature of these backscattered electrons sets up an interference pattern, a spot appearing on the screen where there is constructive interference and dark areas where there is destructive interference.

The interference image follows the Bragg Law of Diffraction. As shown in Figure 5.1, the diffracted beams having a path difference Δl of integer multiples of λ interfere constructively at the screen and a bright area will be displayed. The Bragg Law of Diffraction giving constructive interference is expressed as

$$n\lambda = d\sin\theta, \tag{5.1}$$

where d is the separation between atoms in the crystal lattice and λ is the wavelength of the electrons comprising the beam. For electrons accelerated to an energy of 100 eV, the wavelength will be on the order of 1 Å, which is also the order of the lattice constant in typical crystals. The lattice constant of an Al-*fcc* crystal is 4.05 Å and the nearest-neighbor distance is 2.86 Å.

5.2 Geometry and Basis Vectors

In order to begin a structure factor analysis of a crystal to calculate what a LEED pattern should look like theoretically, we must define a set of basis vectors both in real and reciprocal space. This treatment will be limited to two dimensions in both

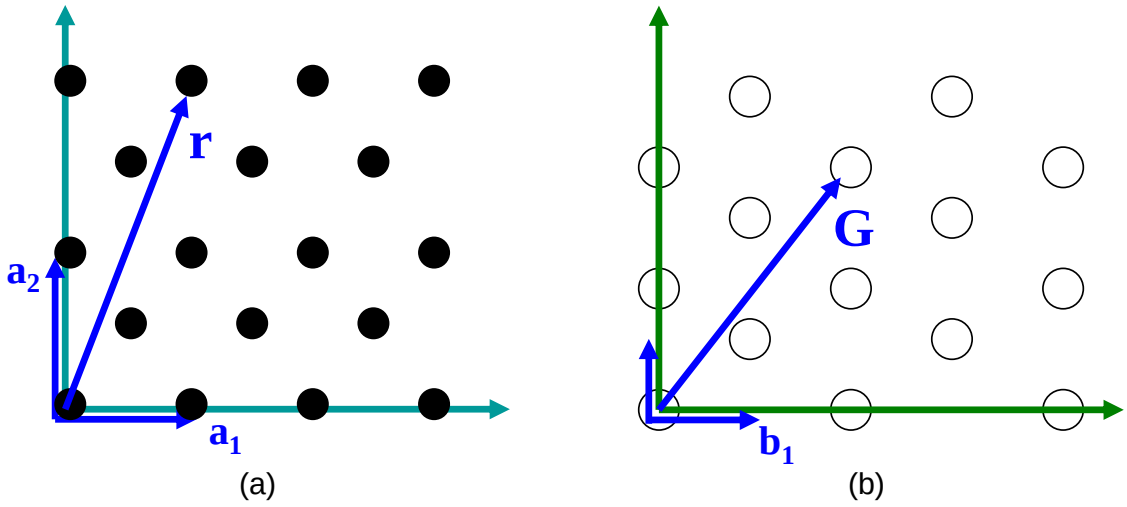

Figure 5.2: Position vector representation (a) real space, (b) reciprocal space.

spaces, considering atoms in a plane in real space and the LEED screen in reciprocal space.

Figure 5.2(a) shows a representation of an an Al-*fcc* lattice cut in the (001) plane. The position vectors for each atom are designated as $\vec{r_j}$ for the j^{th} atom. We define the position vectors in real space as

$$\vec{r_j} = p_j \hat{a}_1 + q_j \hat{a}_2, \tag{5.2}$$

where $\hat{a}_1$ and $\hat{a}_2$ are the real space basis vectors and p_j, q_j are real numbers.

Figure 5.2(b) shows a depiction in reciprocal space, the space where we form an image on the LEED screen. Basis vectors $\hat{b}_1$ and $\hat{b}_2$ and the position vector $\vec{G}_{hk}$ marks the place where a potential spot on the screen can form, given the condition of constructive interference is present. We define this vector as

$$\vec{G}_{hk} = h\hat{b}_1 + k\hat{b}_2, \tag{5.3}$$

where h, k are integers and the reciprocal space basis vectors are defined in terms of real space basis vectors as

$$\hat{b}_1 = 2\pi \frac{\hat{a}_2 \times \hat{a}_3}{\hat{a}_1 \cdot \hat{a}_2 \times \hat{a}_3} \quad \text{and} \quad \hat{b}_2 = 2\pi \frac{\hat{a}_3 \times \hat{a}_1}{\hat{a}_1 \cdot \hat{a}_2 \times \hat{a}_3}. \tag{5.4}$$

5.3 Construction of LEED Image - Structure Factor Analysis

Structure Factor Analysis is the mathematical process behind the construction of a LEED image. The formula for the structure factor S_{hk} in reciprocal space at position $\vec{G}_{hk}$ is

$$S_{hk} = \sum_j f_j \; e^{-i\,\vec{G}_{hk}\cdot\vec{r}_j}, \tag{5.5}$$

where the sum accounts for each position vector $\vec{r}_j$ in real space for each atom j in one unit cell of the crystal lattice. The *form factor* f_j has a unique value for each element present in the unit cell and is approximately equal to the atomic number Z of atom j. The actual intensity of the spot on the LEED screen is found from the expression

$$\text{Spot Intensity} = I_{hk} \propto S^*_{hk} S_{hk}, \tag{5.6}$$

where S^*_{hk} is the complex-conjugate of S_{hk}.

Figure 5.3 shows the real-space two-atom basis unit cell for an Al(001) surface plane where we have designated $\vec{r}_1$ and $\vec{r}_2$ as the position vectors of these atoms. In general

$$\vec{r}_j \;\; = \;\; p_j\hat{x} + q_j\hat{y}, \tag{5.7}$$

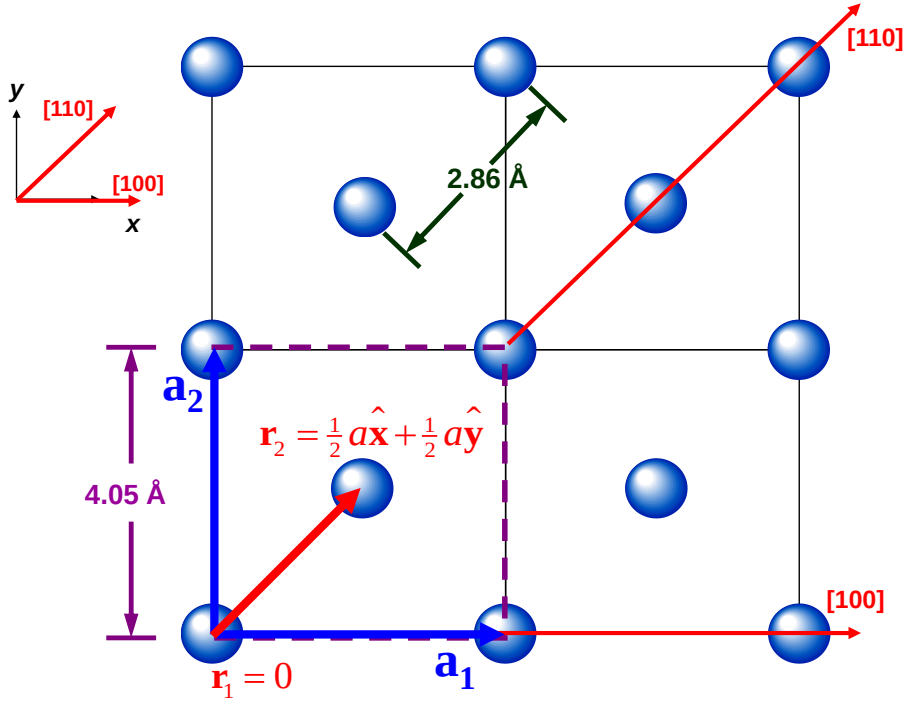

Figure 5.3: Real space representation of the Al(001) crystal surface showing two-atom unit cell.

and specifically

$$\begin{aligned} \vec{r}_1 &= 0, \\ \vec{r}_2 &= \tfrac{1}{2}\, a\hat{x} + \tfrac{1}{2}\, a\hat{y}, \end{aligned} \tag{5.8}$$

where we have replaced $\hat{a}_1, \hat{a}_2$ with $a\hat{x}, a\hat{y}$ respectively. For the Al(001) crystal surface $a = 4.05$ Å, the lattice constant. With these coordinate dimensions, $\vec{G}_{hk}$ is

$$\vec{G}_{hk} = h\, \tfrac{2\pi}{a}\, \hat{x} + k\, \tfrac{2\pi}{a}\, \hat{y}. \tag{5.9}$$

Figure 5.4(a) shows the reciprocal-space representation of the LEED screen with $\vec{G}_{hk}$ as the position vector at coordinates (h, k) where a potential spot can be imaged under constructive interference of the diffracted electron waves.

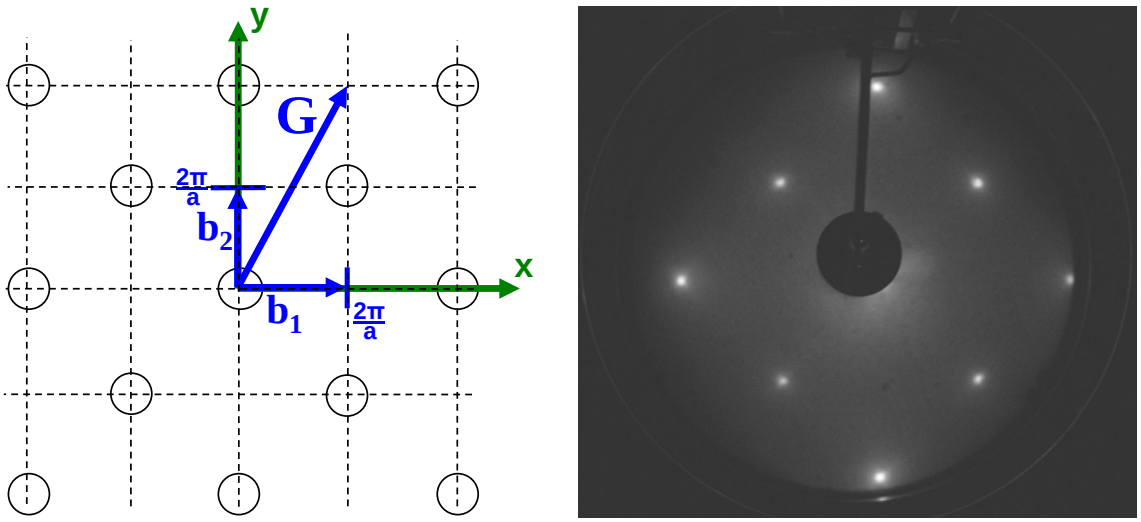

Figure 5.4: (a) Reciprocal space representation of LEED screen for construction of LEED image for an Al(001) crystal surface, and (b) corresponding LEED image.

Evaluating the dot-product of $\vec{G}_{hk}$ and $\vec{r}_j$ in the exponential for $\vec{r}_1$ and $\vec{r}_2$ with all possible values of $\vec{G}_{hk}$ for (h,k) integers, yields the result

$$S_{hk} = \sum_j f_j \; e^{-i\,\vec{G}_{hk}\cdot\vec{r}_j} = f_{Al}\left(1 + e^{-i\pi(h+k)}\right). \tag{5.10}$$

Considering all integer values for h and k yields

$$S_{hk} = \begin{cases} 2f_{Al} & ; \quad (h+k) \text{ even} \\ 0 & ; \quad (h+k) \text{ odd} \end{cases} . \tag{5.11}$$

As we choose values for h and k corresponding to potential spot locations in reciprocal space appearing on the LEED screen, $S^*_{hk}S_{hk}$ is proportional to the intensity of the spot at reciprocal coordinate (h,k). Figure 5.4(b) is a photo of the LEED image corresponding to the above treatment of an Al(001) crystal surface showing the expected $p(1\times 1)$ pattern. The main-central spot is not visible as it is covered by

the LEED gun mechanism. The Al(001) crystal sample was oriented with the [100] azimuth in the horizontal plane of the floor.

5.4 Ti on Al(001)

With a similar treatment we now look at deposited Ti on the Al(001) surface.

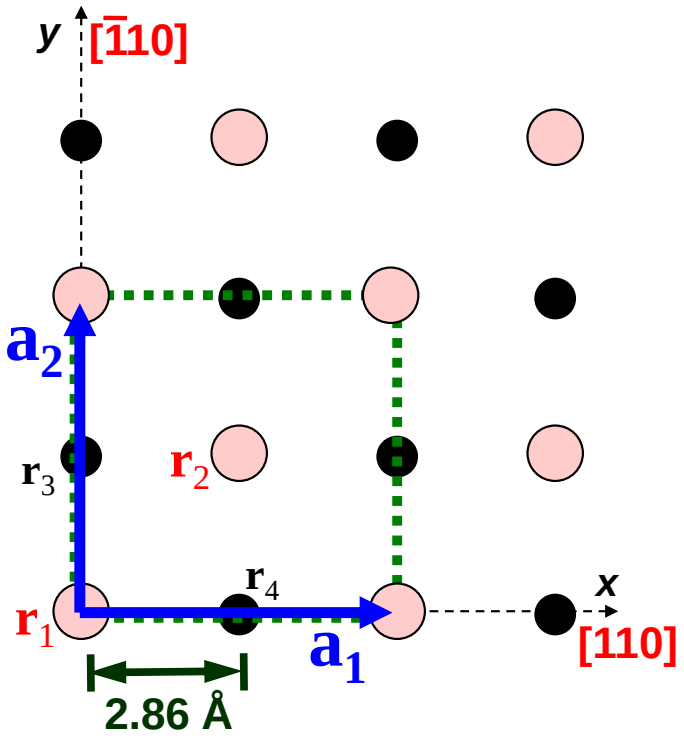

Figure 5.5: Real-space representation of Ti on the Al(001) crystal surface showing the four-atom unit cell. Small dark circles denote Al atoms and large lighter circles denote Ti atoms.

Figure 5.5 shows the real-space representation of an ultra-thin layer of Ti on the Al(001) surface. Note the $\hat{x}, \hat{y}$ axes are the [110] and [$\bar{1}$10] azimuth directions respectively.

We observed a $c(2 \times 2)$ pattern in the LEED image upon completion of the deposition process. A $c(2 \times 2)$ LEED pattern presumes that Ti atoms occupy every-other

Al-lattice site in the surface layers of the substrate. In the figure we show a four-atom unit cell of Ti and Al atoms on the Al(001) surface plane with the corresponding real-space position vectors $\vec{r}_1$ – $\vec{r}_4$ shown and whose values are in general

$$\vec{r}_j \;=\; p_j\, 2a\hat{x} + q_j\, 2a\hat{y}, \tag{5.12}$$

and specifically

$$\begin{aligned} \vec{r}_1 &= 0, \\ \vec{r}_2 &= a\hat{x} + a\hat{y}, \\ \vec{r}_3 &= a\hat{x}, \text{ and} \\ \vec{r}_4 &= a\hat{y}, \end{aligned} \tag{5.13}$$

where $a = 2.86$ Å, the nearest-neighbor lattice spacing of the Al(001) crystal surface. Identical adsorption sites for each four-atom unit cell are repeated every two Al lattice spacings, horizontally and vertically. Thus $\hat{a}_1, \hat{a}_2$ are $2a\hat{x}, 2a\hat{y}$ respectively.

The solution for the expression for S_{hk} in this case is

$$\begin{aligned} S_{hk} &= \textstyle\sum_j f_j\, e^{-i\,\vec{G}_{hk}\cdot\vec{r}_j} \\ &= f_{Al}\left(e^{-i\pi h} + e^{i\pi k}\right) + f_{Ti}\left(1 + e^{-i\pi(h+k)}\right). \end{aligned} \tag{5.14}$$

Considering all integer values for h and k yields

$$S_{hk} = \begin{cases} 2f_{Ti} + 2f_{Al} & ;\;\; h,k \text{ even} \\ 2f_{Ti} - 2f_{Al} & ;\;\; h,k \text{ odd} \\ 0 & ;\;\; h \text{ even},\ k \text{ odd} \quad \text{or} \quad h \text{ odd},\ k \text{ even}. \end{cases} \tag{5.15}$$

The two different form factors used are

$$\begin{aligned} f_{Ti} &= \text{form factor for Ti atom} = 22, \\ f_{Al} &= \text{form factor for Al atom} = 13. \end{aligned} \tag{5.16}$$

We normalized these values with respect to the atomic number of Al giving

$$\begin{aligned} f_{Al} &\Rightarrow 1, \text{ and} \\ f_{Ti} &\Rightarrow \tfrac{22}{13} = 1.69. \end{aligned} \tag{5.17}$$

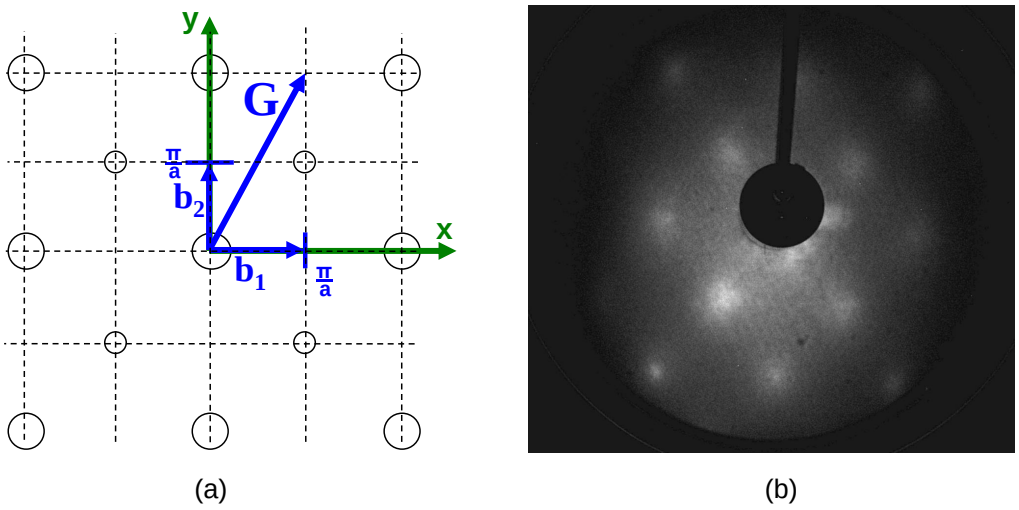

Figure 5.6: (a) Reciprocal space representation of the Ti-Al(001) system and (b) LEED image for ≈ 2.4 ML Ti on Al(001).

Figure 5.6(a) depicts the reciprocal-space representation of this Ti-Al(001) system and (b) shows the LEED photo taken for this system for ≈ 2.4 ML Ti on the Al(001) surface.

Figure 5.7 shows a LEED schematic depicting the $c(2 \times 2)$ pattern with the additional smaller spots, distinct from the Al-clean $p(1 \times 1)$ pattern. Larger spots represent greater brightness, and have higher numeric values as seen in the table accompanying the schematic. Proportional degrees of spot brightness comes from Equation. 5.6 above. Resulting table entries are solutions for S_{hk} given the form factor values used above.

The Al(001) crystal sample was oriented with the [110] azimuth in the horizontal plane of the floor. Given the fuzziness of the LEED image we must conclude that the

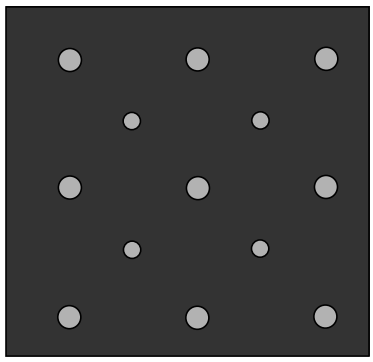

f(Ti)	1.69
f(Al)	1.00

h	k	$\lvert S_{hk}\rvert$	h	k	$\lvert S_{hk}\rvert$	h	k	$\lvert S_{hk}\rvert$	h	k	$\lvert S_{hk}\rvert$	h	k	$\lvert S_{hk}\rvert$
-2	-2	5.38	-2	-1	0.00	-2	0	5.38	-2	1	0.00	-2	2	5.38
-1	-2	0.00	-1	-1	1.38	-1	0	0.00	-1	1	1.38	-1	2	0.00
0	-2	5.38	0	-1	0.00	0	0	5.38	0	1	0.00	0	2	5.38
1	-2	0.00	1	-1	1.38	1	0	0.00	1	1	1.38	1	2	0.00
2	-2	5.38	2	-1	0.00	2	0	5.38	2	1	0.00	2	2	5.38

Figure 5.7: $c(2 \times 2)$ LEED schematic with accompanying table listings of solution values from Eqn. 5.14

ideal structure of Ti atoms present at every-other Al-lattice site is in actuality, not fully developed. We conclude that only small patches of Ti are so arranged thereby resulting in this inherently blurred image.

5.5 Ag on Al(001)

We now turn to a similar treatment of the deposited TM Ag on the Al(001) surface, an example of a more complex structure analysis showing the utility of structure factor analysis. D. S. Choi [12] determined the structure of an ultra-thin layer of Ag on Al(001), upon which we base this analysis.

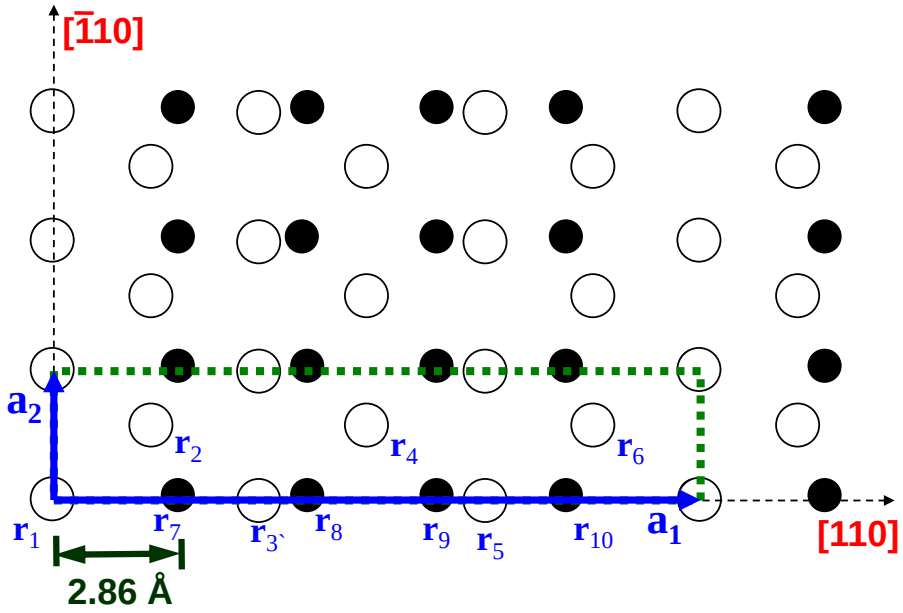

Figure 5.8: Real-space representation of Ag on the Al(001) crystal surface showing the ten-atom unit cell.

Figure 5.8 shows the real-space representation of an ultra-thin layer of Ag on the Al(001) surface. The $\hat{x}, \hat{y}$ axes are the [110] and [$\bar{1}$10] azimuth directions respectively.

We observed a $p(5 \times 1)$ pattern in the LEED image upon completion of the deposition process. D. S. Choi analyzed the results for LEIS performed on this system

and theorized that Ag on the Al(100) surface forms a quasi-hexagonal structure in a (5×1) coincidence lattice with the *fcc*-structure of the Al(100) substrate surface, i.e. the surface layer of Ag atoms is coincident with the Al(100) surface unit cell, having a repeat distance of 5 Al(100) interatomic spacings in the [110] direction [12]. The LEED pattern shows a double-domain $p(5 \times 1)$ structure with additional intensity in those spots corresponding to a (111) close-packed hexagonal layer. In the figure we show a ten-atom unit cell of Ag and Al atoms on the Al(001) surface plane with the corresponding real-space position vectors $\vec{r}_1$ through $\vec{r}_{10}$ whose values are in general

$$\vec{r}_j = p_j \, 5a\hat{x} + q_j \, a\hat{y}, \tag{5.18}$$

and specifically

$$\begin{aligned}
\vec{r}_1 &= 0, \\
\vec{r}_2 &= \tfrac{1}{6}(5a\hat{x}) + \tfrac{1}{2}a\hat{y}, \\
\vec{r}_3 &= \tfrac{2}{6}(5a\hat{x}), \\
\vec{r}_4 &= \tfrac{3}{6}(5a\hat{x}), + \tfrac{1}{2}a\hat{y}, \\
\vec{r}_5 &= \tfrac{4}{6}(5a\hat{x}), \\
\vec{r}_6 &= \tfrac{5}{6}(5a\hat{x}), + \tfrac{1}{2}a\hat{y}, \\
\vec{r}_7 &= \tfrac{1}{5}(5a\hat{x}), \\
\vec{r}_8 &= \tfrac{2}{5}(5a\hat{x}), \\
\vec{r}_9 &= \tfrac{3}{5}(5a\hat{x}), \text{ and} \\
\vec{r}_{10} &= \tfrac{4}{5}(5a\hat{x}).
\end{aligned} \tag{5.19}$$

where in this case $a = 2.86$ Å, the nearest-neighbor lattice spacing of the Al(001) crystal surface. Identical adsorption sites for each ten-atom unit cell are repeated

every five Al lattice spacings horizontally and one Al lattice space vertically. Thus $\hat{a}_1, \hat{a}_2$ are $5a\hat{x}, a\hat{y}$ respectively. In Figure 5.8 $\vec{r}_1$ through $\vec{r}_{10}$ are not drawn in but the descriptor is placed near its respective atom, the position vector for each begining at the origin and terminating on the respective atom.

The solution for the expression for S_{hk} in this case is

$$\begin{aligned} S_{hk} &= \textstyle\sum_j f_j \; e^{-i\,\vec{G}_{hk}\cdot\vec{r}_j} \\ &= f_{C1} + f_{Al}\left(e^{-\frac{2}{5}i\pi h} + e^{-\frac{4}{5}i\pi h} + e^{-\frac{6}{5}i\pi h} + e^{-\frac{8}{5}i\pi h}\right) \\ &\quad + f_{Ag}\left(e^{-\frac{1}{3}i\pi(h+3k)} + e^{-\frac{1}{3}i\pi(2h)} + e^{-\frac{1}{3}i\pi(3h+3k)} + e^{-\frac{1}{3}i\pi(4h)} + e^{-\frac{1}{3}i\pi(5h+3k)}\right). \end{aligned} \tag{5.20}$$

Due to the greater permutations of appropriate integer values for h and k the calculated values for S_{hk} are best expressed in a table as shown in Figure 5.9 below.

The three different form factors used are

$$\begin{aligned} f_{C1} &= \text{form factor for Ag atom above Al atom,} \\ f_{Ag} &= \text{form factor for Ag atom} = 47, \\ f_{Al} &= \text{form factor for Al atom} = 13. \end{aligned} \tag{5.21}$$

We normalized these values with respect to the atomic number of Al giving

$$\begin{aligned} f_{Al} &\Rightarrow 1, \\ f_{Ag} &\Rightarrow \tfrac{47}{13} = 3.62, \\ f_{C1} &\Rightarrow \text{ choose } 3.00. \end{aligned} \tag{5.22}$$

The form factor f_{C1} for the ag atom directly above an Al atom at position $\vec{r}_1$ is not simply the atomic number of a Ag atom, its value being influenced by the close proximity of the Al atom below. For a qualitative treatment, we choose 3.00 as its normalized value, simply a place holder guess as a combination of the two species.

Figure 5.9 depicts the reciprocal-space representation of this Ag-Al(001) system with a LEED schematic showing spots of varying size. These spots are represented

f_{C1}	3.00
f_S	3.62
f_{Al}	1.00

LEED Schematic →

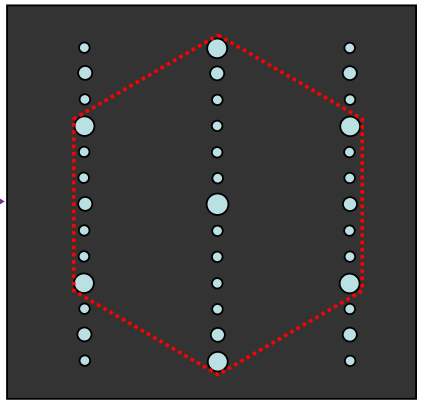

h	*k*	$\|S_{hk}\|$	*h*	*k*	$\|S_{hk}\|$	*h*	*k*	$\|S_{hk}\|$
-6	1	1.6	-6	0	20.1	-6	-1	1.6
-5	1	3.4	-5	0	3.4	-5	-1	3.4
-4	1	1.6	-4	0	1.6	-4	-1	1.6
-3	1	20.1	-3	0	1.6	-3	-1	20.1
-2	1	1.6	-2	0	1.6	-2	-1	1.6
-1	1	1.6	-1	0	1.6	-1	-1	1.6
0	1	3.4	0	0	25.1	0	-1	3.4
1	1	1.6	1	0	1.6	1	-1	1.6
2	1	1.6	2	0	1.6	2	-1	1.6
3	1	20.1	3	0	1.6	3	-1	20.1
4	1	1.6	4	0	1.6	4	-1	1.6
5	1	3.4	5	0	3.4	5	-1	3.4
6	1	1.6	6	0	20.1	6	-1	1.6

Figure 5.9: Reciprocal space representation of the Ag-Al(001) system, table listings of solution values from Eqn. 5.20 and inset LEED schematic.

by numeric values in the table, the higher number representing a brighter spot. Proportional degrees of spot brightness are expressed in Equation 5.6 and values for S_{hk} from Equation 5.20. Resulting table entries are solutions given the form factor values used above.

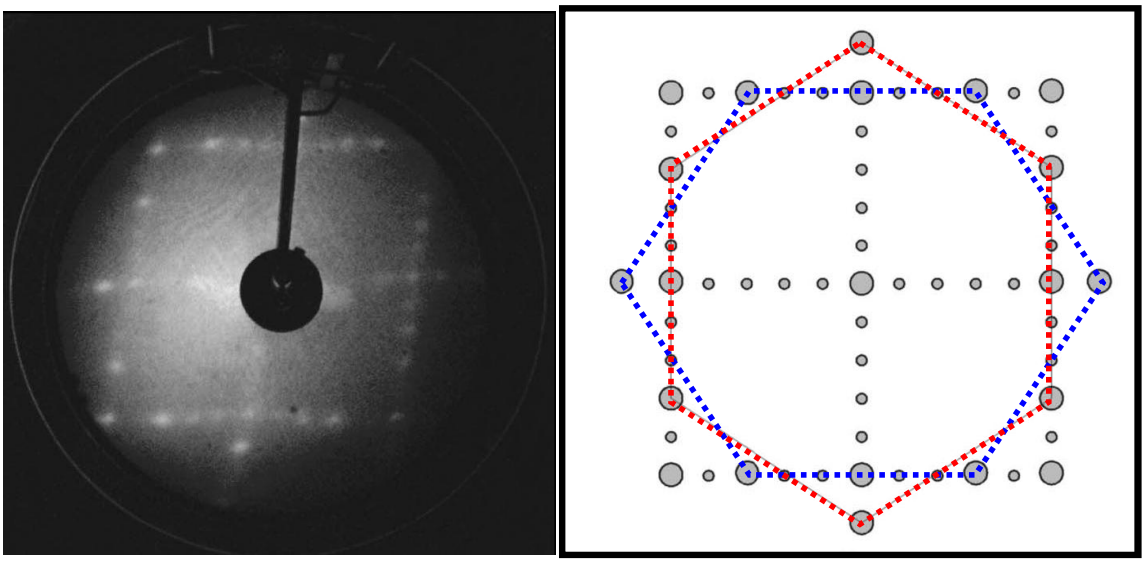

Figure 5.10: (a) LEED image for 0.7 ML Ag on Al(001) with (b) accompanying schematic drawing for clarity.

Figure 5.10(a) shows the actual LEED photo taken for this system for 0.7 ML Ag on the Al(001) surface. The Al(001) crystal sample was oriented with the [110] azimuth in the horizontal plane of the floor. To the right of the actual photo in Figure 5.10(b) is a schematic representation of the LEED image showing the double-domain $p(5 \times 1)$ pattern with connecting lighter and darker dotted lines to clarify the superimposed quasi-hexagonal pattern.

CHAPTER 6

THE BFS MODEL FOR ALLOYS

6.1 BFS Model for Analysis of TMs on Metal Substrates

Bozzolo et al. [8] created the BFS Method for Alloys to determine the affinity of one metal to form an alloy with another. Implementing first principles calculations utilizing a linear-augmented plane wave approach (LAPW), where parameters for metals, including the transition elements, are determined. G. Bozzolo and his collaborators determine these specific parameters. Parameter sets are labeled as LAPW-J and LAPW-H, depending upon the specifics of the approach used. The interested reader can study the references for more detail.

The BFS Model program is named *adwTools* [27]. Using this program, the energies of formation ΔH of a binary alloy are calculated by taking into account the energy contribution from the individual atoms involved, e_A and e_B for atoms A and B forming the alloy. The motivation for our group in using this approach is whether this method can aid us to find a suitable ultra-thin interlayer element C from the transition metals (TM) to place between element A and substrate element B to prevent diffusion of A into B and vice-versa, and forming a stable structure overall.

The motivation to study V on Al(001) in this thesis is based on the subsequent analysis of the specific case of Ti as an interlayer between Fe and an Al substrate, and the prediction that V falls into the same category as Ti. Thus we look into the Fe-Ti-Al interlayer system as an introduction to our work with V.

6.1.1 Ti Interlayer for the Fe-Al System

Addressed here is an analysis by Bozzolo [1] for Fe deposited on Al(100)-*bcc* using Ti as an interlayer. It is appropriate for our work with Ti on Al(001)-*fcc* since looking at the characteristics of thin-film Ti on Al from an energy of formation standpoint leads to insight on how the two elements interact structurally. Though we cannot apply the quantitative results to our specific case, it is worthwhile to consider the results of this BFS study qualitatively.

Garcés and Bozzolo [8] describe the theoretical treatment for calculating the energy of formation ΔH of an alloy in their work presenting the BFS Method. ΔH is the energy difference of elements involved in a binary interaction, compared to the equilibrium energies of the two when they are apart. The equation for ΔH [8] is

$$\Delta H = \sum_i e_i, \tag{6.1}$$

where e_i is the energy of formation of each individual atom i in the alloy. This e_i is the superposition of two energy contributions calculated separately, a strain energy term e_i^S and a chemical energy term e_i^C. Both are calculated in a lattice structure where contributions from surrounding atoms are limited to nearest-neighbor (NN) and next-nearest-neighbor (NNN) interactions. The strain energy e^S calculation environment places atom i in a strained lattice structure whose lattice constant is determined by the alloy, but surrounded strictly by atoms of its own chemical identity. The calculation of the chemical energy term e^C is done in a lattice structure whose lattice constant is that of a pure crystal of atom i while retaining the specific chemical identities of all surrounding atoms. The contribution by e^C is scaled by a factor g_i (referred to as the 'glue') that accounts for the separation distance between an interaction pair that

would diminish the effect of the chemical interaction as separation distances become large. The expression for e_i [8] is

$$e_i = e_i^S + g_i(e_i^C + e_i^{C_0}), \tag{6.2}$$

where $e_i^{C_0}$ is a reference chemical energy contribution that ensures a complete decoupling between the structural and chemical aspects of the alloy.

This analysis utilizes the B2 CsCl *bcc*-like structure, composed of two elements each fully populating alternate layers in the crystal.

The TMs divide into five groups in their binary interaction with Al. Table 6.1 lists the results of the BFS calculations. e_X and e_{Al} are the energy contributions to the

Table 6.1: BFS Method results as applied to Al substrate and listed TM overlayers [1].

Group	e_X	X $\cdots$ Al	e_{Al}	Al $\cdots$ X	ΔH	Alloy	Element X (TM)
1	> 0	repels	< 0	attracts	< 0	yes	Ni,Co,Cu,Pd,Fe,Pt,Hf
2	> 0	repels	< 0	attracts	> 0	no	Cr
3	< 0	attracts	< 0	attracts	< 0	yes	Zr,Ru,Au
4	< 0	attracts	> 0	repels	> 0	no	Ta,W
5	< 0	attracts	> 0	repels	< 0	yes	Ti,Mo,Nb,V

formation energy for element X (the TM) and Al respectively. The sign of e_X and e_{Al} determines whether the atom contributes an attractive or repulsive component to the net force of interaction. ΔH then is the total energy of formation of the binary alloy accounting for the individual contributions of e_X and e_{Al}. A negative ΔH indicates that alloy formation is likely at equilibrium conditions, while a positive value indicates that alloying is not likely.

Consider the specific case of Fe deposited on Al. Fe belongs to Group 1, where the attraction of Al dominates and ΔH is negative indicating that alloy formation is likely. We ask which of the other elements X could be considered as a suitable

interlayer to prevent interdiffusion of Fe and Al? We dismiss those in Groups 1–3 since Al attracts these, but Al repels all elements in Groups 4 and 5 making these possible candidates.

To stress the main point and objective, let us state the desired characteristics of a suitable interlayer. A suitable interlayer element must *attract* the substrate and overlayer elements, while the substrate and overlayer elements must *repel* the interlayer element.

As an example, Ti was chosen as a possible interlayer element. The next step in the process considers the interaction of Ti with all the other TMs. The BFS calculations are repeated pairing all TMs with Ti instead of Al. This gives two groups, an α group where Ti attracts X (TM) but X repels Ti, and a β group where Ti repels X but X attracts Ti. All the TM's in the original Groups 1–3 fall into the α group, and those in Groups 4 and 5 fall into the β group with the exception of V which ends up being in the α group (V appears to have some quality which differentiates it from the other Groups 4 and 5 elements, which will not be pursued but yet interesting to note). Fe as well as Al are in the α group.

To bring all these ideas together, we must consider the binary interaction of all combinations from the three elements and how this then affects Fe as the overlayer. We treat this by looking at a subset of results of the two sets of BFS calculations. Table 6.2 gives the interactions of Al with X (Fe and Ti), and Table 6.3, the interactions of Ti with X (Fe and Al).

Table 6.2: BFS Method results pairing Al with Fe and Ti [1].

X	e_X	X $\cdots$ Al	e_{Al}	Al $\cdots$ X	ΔH	Alloy
Fe	+1.12	repels	-1.64	attracts	-0.26	yes
Ti	-1.48	attracts	+0.64	repels	-0.42	yes

Table 6.3: BFS Method results pairing Ti with Fe and Al [1].

X	e_X	X $\cdots$ Ti	e_{Ti}	Ti $\cdots$ X	ΔH	Alloy
Fe	+1.43	repels	-1.95	attracts	-0.26	yes
Al	+0.64	repels	-1.48	attracts	-0.42	yes

Checking the main objective, does Ti satisfy the characteristics of a suitable interlayer, i.e. does Ti *attract* Al and Fe, and do Al and Fe *repel* Ti? Table 6.3 verifies this mandate with the results

- Ti attracts Fe (-1.95)
- Ti attracts Al (-1.48)
- Al repels Ti (+0.64)
- Fe repels Ti (+1.43)

6.1.2 Layer Examples of the Ti Interlayer Fe-Al System

The steps that follow provide more detail to this analysis with Ti as the interlayer between Fe and the Al substrate. Tables are used placing specific elements in specific layers, listing BFS results for e_i^S the strain energy, g, e_i^C the chemical energy, and finally e_i the total energy contribution for any atom in layer i as one table row entry. Each layer contains only one element type i. Table row entries represent crystal layer order from top to bottom.

We begin by placing an Fe overlayer on an Al substrate.

Adding the e_i contributions from each layer in the table, gives us a values for the total energy of the system, which we then can compare to other systems of different arrangements, and examine which arrangement will lower the total energy and thus

Table 6.4: First example Fe/Al/Al [1].

Layer i	e_i^S	g	e_i^C	e_i
Fe	3.50	0.07	0.63	3.54
Al	0.00	0.98	-0.14	-0.14
Al	0.00	1.00	0.00	0.00

be considered to be the most likely arrangement to occur. This total energy will be called the *cell energy*.

Next we place Fe one layer below the surface on an Al substrate.

Table 6.5: Next Al/Fe/Al/Al [1].

Layer i	e_i^S	g	e_i^C	e_i
Al	1.85	0.16	-0.25	1.81
Fe	1.31	0.36	1.28	1.77
Al	0.00	1.00	-0.16	-0.16
Al	0.00	1.00	0.00	0.00

Fe/Al/Al $\rightarrow$ Al/Fe/Al/Al shows a reduction in 1$^{\text{st}}$ layer surface e_{Fe} = +3.54 eV to e_{Al} = +1.81 eV which tells us Fe prefers subsurface occupancy. A 2$^{\text{nd}}$ layer Fe has a high e_{Fe}^S (+1.31 eV) and high e_{Fe}^C repulsion of neighboring Al (+1.28 eV). However looking at the *cell* energy ($\sum_i e_i$) over all Layers i for each case, yields approximately the same result (+3.40 and +3.42 eV). However, with Fe in the 2$^{\text{nd}}$ layer, the surface energy of the top Al layer is less which makes the Al/Fe/Al/Al combination the favored one.

Next we do the same thing with Ti in place of Fe.

Ti/Al/Al $\rightarrow$ Al/Ti/Al/Al shows a substantial lowering of the cell energy (compare cell energy for Ti/Al/Al at +1.87 eV with Al/Ti/Al/Al at +0.81 eV). This decrease primarily stems from 2$^{\text{nd}}$ layer Ti having e_{Ti}^S at 0.0 eV and a decrease in e_{Ti}^C from 1$^{\text{st}}$ layer at -0.54 eV to 2$^{\text{nd}}$ layer -1.30 eV. This shows that Ti likes to surround itself with

Table 6.6: Ti/Al/Al [1].

Layer i	e_i^S	g	e_i^C	e_i
Ti	1.92	0.30	-0.54	1.76
Al	0.00	0.98	0.21	0.21
Al	0.00	1.00	0.00	0.00

Table 6.7: Al/Ti/Al/Al [1].

Layer i	e_i^S	g	e_i^C	e_i
Al	1.85	1.85	0.40	1.92
Ti	0.00	1.01	-1.30	-1.31
Al	0.00	1.00	0.20	0.20
Al	0.00	1.00	0.00	0.00

Al atoms (see $\Delta H_{Ti-Al} = -0.42eV$ in Table 6.3). This corroborates the Ti-Al LEIS analysis results that Ti prefers subsurface occupancy with Al as the surface layer.

Now place an Fe layer in the place of the Al surface. Compared to the previous

Table 6.8: Fe/Ti/Al/Al [1].

Layer i	e_i^S	g	e_i^C	e_i
Fe	3.50	0.07	0.76	3.55
Ti	0.00	1.01	-1.44	-1.45
Al	0.00	1.00	0.20	0.20
Al	0.00	1.00	0.00	0.00

case, the energies of the Ti 2$^{\text{nd}}$ layer are not changed significantly by replacing the surface Al atoms with Fe. That is with the Fe surface, Ti strain energy e_{Ti}^S remains at 0.0 eV and Ti chemical energy e_{Ti}^C drops from -1.30 eV with the Al surface to -1.44 eV with the Fe surface. Similarly Ti 2$^{\text{nd}}$ layer e_{Ti} drops from -1.31 eV to -1.45 eV. The Fe 1$^{\text{st}}$ layer energies are much higher than the corresponding ones for Al, but Ti definitely prefers to be in the 2$^{\text{nd}}$ layer for both cases.

For contrast, the next step places Ti in the 1st layer, Fe in the 2nd layer and Al below.

Table 6.9: Ti/Fe/Al/Al [1].

Layer i	e_i^S	g	e_i^C	e_i
Ti	1.92	0.30	-0.57	1.75
Fe	1.31	0.36	1.49	1.84
Al	0.00	1.00	-0.16	-0.16
Al	0.00	1.00	0.00	0.00

This combination is energetically unfavorable, with a Ti 1st layer high e_{Ti}^S at +1.92 eV and Fe 2nd layer high e_{Fe}^S at +1.31 eV and high e_{Fe}^C at +1.49 eV. There is a small Al attractive e_{Al}^C at -0.16 eV, but this is insignificant compared to the unfavorable energy gains experienced by Ti and Fe.

We now add another Fe layer to the Fe/Ti/Al/Al case making an Fe/Fe/Ti/Al/Al stack. Adding a second Fe top layer barely changes the energetics of the subsurface

Table 6.10: Fe/Fe/Ti/Al/Al [1].

Layer i	e_i^S	g	e_i^C	e_i
Fe	3.50	0.07	0.00	3.50
Fe	1.30	0.36	0.67	1.54
Ti	0.00	1.02	-1.58	-1.61
Al	0.00	1.00	0.20	0.20
Al	0.00	1.00	0.00	0.00

Fe/Ti/Al structure, e_{Ti} is still low at -1.61 eV (a decrease from -1.45 eV) and the addition of the new Fe layer added only an additional strain e_{Fe}^S to the cell.

To sum this up, Ti interacts with Fe and Al producing different compound formation effects so as to form a stable Ti interlayer.

It is interesting to note that in Groups 4 and 5, Ta, W, Mo, Nb and V all have a native *bcc* structure while the remaining element Ti is the only one with a different

native structure of *hcp*. The analysis here utilized the B2 (*bcc-like*) structure which is not native to Ti, nor to Al. Ti is found to take on the *fcc* structure of Al when deposited on the Al(001) surface [28, 29]. Bozzolo based this analysis on the assumption that structural effects are secondary to energy considerations and that many Al-TM compounds have the B2 CsCl structure.

6.1.3 Basis for Ti and V as Interlayers via the BFS Model

The study of V in this thesis is motivated by the analysis presented above which focused on the specific case of Ti as an interlayer between Fe and an Al substrate. Previous work by our group confirmed through experiment that Ti is a suitable interlayer for the Fe-Ti-Al system [10]. V is placed in the same category by the BFS Model as Ti, belonging to Group 4 as detailed above, which leads to the prediction that V should be an effective interlayer as is Ti between Fe and Al.

To summarize the calculations by G. Bozzolo for this prediction, Table 6.11 shows the energy of formation ΔH using Al as the substrate element paired with Ti and V respectively. The contributions of each atom are listed as e_X where X is Ti or V, and e_{Al} for Al. The lattice constant a_0 for the B2 *bcc*-type structure for the respective pairing with Al is also listed.

Table 6.11: BFS Method results pairing substrate Al with transition elements Ti and V [1].

X	e_X (eV)	e_{Al} (eV)	a_0 (Å)	ΔH (eV/atom)
Ti	-1.48	+0.64	3.187	-0.42
V	-2.67	+2.60	3.064	-0.04

Note that the formation energy for each pair is negative, indicating the likelihood for alloying. The same process was repeated replacing Al with Fe as the substrate

element and it was found that Ti and V were again in the same subgroup with the same properties as in their interaction with Al.

Reiterating the requirements of an effective interlayer as stated in Section 1.2, the total formation energy for the interlayer/substrate and interlayer/overlayer pairs must be negative, indicating a likelihood for alloying. Next the interlayer must 'attract' both the substrate and overlayer (the interlayer's contribution to the formation energy must be negative). Finally both the substrate and the overlayer must 'repel' the interlayer (the substrate's and overlayer's contribution to the formation energy must be positive).

From the above BFS Model calculations we have the prediction that V and Ti are both suitable interlayers between Al and Fe. This thesis addresses the question of whether V is as effective in this role as Ti, motivating our work with the Ti-Al and V-Al systems.

6.2 BFS Method Analysis of Ti and V on Al

In this section the Ti-Al and V-Al systems are treated using the BFS Method for Alloys. Both Ti and V atoms placed on an Al(100)-*bcc* substrate will be analyzed. Ti on an Al(100)-*fcc* substrate will only be analyzed, as the required parameters for V in this system are not currently supported by the program. The use of Ti and V as an interlayer is not addressed here, but rather an analysis of the Ti-Al and V-Al systems is studied to gain insight into the results of our experimental work using LEIS and LEED in studying these two systems.

6.2.1 Ti on an Al-bcc (100) Substrate

We configured adwTools with parameters for an Al substrate *bcc*-(100)-surface structure creating a cell of $9 \times 9 \times 9$ atoms in size (81 atoms/layer), with the Al lattice constant $a_0 = 3.24$ Å for *bcc*-Al and utilizing the LAPW-H (constant) parameter set.

6.2.1.1 1 ML Ti on Al-bcc:

Table 6.12 gives the cell energy (159.411 eV) of a full Ti layer first placed just in the surface (S) of the Al(100)-*bcc* substrate. Next this full Ti layer is placed just one layer below the surface (1b) giving a cell energy of 65.386 eV. This Ti layer placement is repeated at two layers below the surface (2b) and finally at three layers below the surface (3b) with respective cell energies found.

Table 6.12: BFS Method calculated cell energies for successive top four layers for 1 ML Ti on Al(100)-*bcc*.

Ti 1 ML on Al(100)-*bcc*		
Ti Structure	Ti Layer	Cell Energy (eV)
$p(1 \times 1)$	S	159.411
$p(1 \times 1)$	1b	65.386
$p(1 \times 1)$	2b	65.788
$p(1 \times 1)$	3b	64.971

The results of table 6.12 show that the minimal cell energy occurs for a full layer of Ti atoms in the 3b layer. The cell energies of layers 1b, 2b and 3b are similar with a drastic gain from the energy of Ti in the surface. This suggests that a layer fully populated with Ti prefers subsurface placement, and ultimately prefers a bulk environment (recall $\Delta H_{Ti-Al} = -0.42eV$ in Table 6.3).

6.2.1.2 0.5 ML Ti on Al-bcc:

Table 6.13 gives the cell energies of 0.5 ML Ti placed successively in the S, 1b, 2b and 3b layers in the Al(100)-*bcc* substrate. Each

trial was done in two ways, one placing the Ti atoms in a $c(2 \times 2)$ pattern and in the other, done randomly. Each trial placed a total of 41 Ti atoms in the layer out of 81 total lattice sites possible. The remaining 40 lattice sites in the layer were filled with Al atoms.

Table 6.13: BFS Method calculated cell energies for successive top four layers for 0.5 ML Ti on Al(100)-*bcc*.

Ti 0.5 ML on Al(100)-*bcc*		
Ti Structure	Ti Layer	Cell Energy (eV)
$c(2 \times 2)$	S	151.783
random	S	152.260
$c(2 \times 2)$	1b	100.835
random	1b	102.415
$c(2 \times 2)$	2b	97.598
random	2b	99.766
$c(2 \times 2)$	3b	96.961
random	3b	99.162

The results of table 6.13 show that the minimal cell energy occurs for Ti atoms in the 3b layer with the $c(2 \times 2)$ pattern slightly energetically favored over the random placement. This suggests that a layer half populated with Ti prefers subsurface placement.

6.2.2 Ti on an Al-fcc (100) Substrate

We configured adwTools with parameters for an Al substrate *fcc*-(100)-surface structure creating a cell of $9 \times 9 \times 9$ atoms in size (162 atoms/layer), with the Al lattice constant $a_0 = 4.04595$Åand utilizing the LAPW-J (canonical) parameter set.

6.2.2.1 1 ML Ti on Al-fcc: Table 6.14 gives the cell energies of a full Ti layer placed successively in the S, 1b, 2b and 3b layers in the Al(100)-*fcc* substrate.

Table 6.14: BFS Method calculated cell energies for successive top four layers for 1 ML Ti on Al(100)-*fcc*.

Ti 1 ML on Al(100)-*fcc*		
Ti Structure	Ti Layer	Cell Energy (eV)
$p(1 \times 1)$	S	206.503
$p(1 \times 1)$	1b	-31.751
$p(1 \times 1)$	2b	-7.399
$p(1 \times 1)$	3b	-7.691

The results of table 6.14 show that the minimal cell energy occurs for a full layer of Ti atoms in the 1b layer. The cell energies of layers 2b and 3b are similar and not as energetically favorable as for 1b, but all subsurface layer Ti placements give a drastic gain from the energy of Ti in the surface. This suggests that a layer fully populated with Ti prefers subsurface placement.

6.2.2.2 0.5 ML Ti on Al-fcc: Table 6.15 gives the cell energies of 0.5 ML Ti placed successively in the S, 1b, 2b and 3b layers in the Al(100)-*fcc* substrate. Each trial was done in two ways, one placing the Ti atoms in a $c(2 \times 2)$ pattern and in the other, done randomly. Each trial placed a total of 81 Ti atoms in the layer out of 162 total lattice sites possible, with the remaining 81 sites occupied by Al.

The results of table 6.15 show that the minimal cell energy occurs for Ti atoms in the 3b layer with the random placement slightly energetically favored over the $c(2 \times 2)$ pattern. This suggests that a layer half populated with Ti prefers subsurface placement.

It is interesting to note here that experimental deposition of a thin-film of Ti on the Al(001) surface produced a $c(2 \times 2)$ LEED pattern. It was hoped that BFS results would have supported this, but this is not the case.

Table 6.15: BFS Method calculated cell energies for successive top four layers for 0.5 ML Ti on Al(100)-*fcc*.

Ti 0.5 ML on Al(100)-*fcc*		
Ti Structure	Ti Layer	Cell Energy (eV)
$c(2 \times 2)$	S	186.184
random	S	175.225
$c(2 \times 2)$	1b	44.279
random	1b	29.609
$c(2 \times 2)$	2b	37.869
random	2b	28.657
$c(2 \times 2)$	3b	37.632
random	3b	25.979

6.2.3 V on an Al-bcc (100) Substrate

We configured adwTools with parameters for an Al substrate *bcc*-(100)-surface structure creating a cell of $9 \times 9 \times 9$ atoms in size (81 atoms/layer), with the Al lattice constant $a_0 = 3.24$Åand utilizing the LAPW-H (constant) parameter set.

6.2.3.1 1 ML V on Al-bcc: Table 6.16 gives the cell energies of a full V layer placed successively in the S, 1b, 2b and 3b layers in the Al(100)-*bcc* substrate.

Table 6.16: BFS Method calculated cell energies for successive top four layers for 1 ML V on Al(100)-*bcc*.

V 1 ML on Al(100)-*bcc*		
V Structure	V Layer	Cell Energy (eV)
$p(1 \times 1)$	S	315.930
$p(1 \times 1)$	1b	102.115
$p(1 \times 1)$	2b	138.133
$p(1 \times 1)$	3b	137.825

The results of table 6.16 show that the minimal cell energy occurs for a full layer of V atoms in the 1b layer. The cell energies of layers 2b and 3b are similar and not as energetically favorable as for 1b, but all subsurface layer V placements give a drastic

gain from the energy of V in the surface. This is the same result as for 1 ML Ti on Al(001)-*fcc* as seen in Table 6.14, and we arrive at the same respective conclusion that a layer fully populated with V prefers subsurface placement.

6.2.3.2 0.5 ML V on Al-bcc: Table 6.17 gives the cell energies of 0.5 ML V placed successively in the S, 1b, 2b and 3b layers in the Al(100)-*bcc* substrate. Each trial was done in two ways, one placing the V atoms in a $c(2 \times 2)$ pattern and in the other, done randomly. Each trial placed a total of 41 V atoms in the layer out of 81 total lattice sites possible. The remaining 40 lattice sites in the layer were filled with Al atoms.

Table 6.17: BFS Method calculated cell energies for successive top four layers for 0.5 ML V on Al(100)-*bcc*.

V 0.5 ML on Al(100)-*bcc*		
V Structure	V Layer	Cell Energy (eV)
$c(2 \times 2)$	S	225.375
random	S	226.529
$c(2 \times 2)$	1b	110.864
random	1b	114.100
$c(2 \times 2)$	2b	118.705
random	2b	123.601
$c(2 \times 2)$	3b	117.906
random	3b	122.885

The results of table 6.17 show that the minimal cell energy occurs for V atoms in the 1b layer with the $c(2 \times 2)$ pattern slightly energetically favored over the random placement. The cell energies of layers 2b and 3b are similar and not as energetically favorable as for 1b, but all subsurface layer V placements give a drastic gain from the energy of V in the surface. This suggests that a layer fully populated with V prefers subsurface placement.

Note that experimental deposition of a thin-film of V on the Al(001) surface did not produced any distinctive LEED pattern. It was hoped that BFS results would have supported this instead of a $c(2 \times 2)$ pattern, but this is not the case.

6.2.4 Conclusion for BFS Model Results for Ti-Al and V-Al

The BFS Model for Alloys is a good tool to aid in the study of deposition of TM elements onto a metal substrate. Though quantitative results cannot be applied to the specific cases of our study of Ti and V on Al(001), qualitatively the method does support the idea that both Ti and V prefer subsurface occupancy in their respective systems.

CHAPTER 7
SIMULATION OF LEIS POLAR-ANGLE SCAN SPECTRA

7.1 Introduction and Overview

Computer simulation of ion-backscattering spectroscopic techniques has received a large investment of time and study in surface science and has carved a niche in the field where a great devoted effort by researchers has flourished. Numerous programs exist that simulate ion scattering such as MARLOWE [30], MATCH [31], SSIS-92 [32], and others. Many such programs are based on Monte-Carlo techniques operated on a three-dimensional model of the crystal substrate. This treatment is very thorough and includes within the program the treatment of thermal vibrations of atoms in the model crystal, simulating an incoming ion beam incident on an operator-chosen area of the substrate surface. Such techniques require considerable investment of computer time to generat a simulated spectrum. Much less computer time is required for simulation techniques of a two-dimensional nature, and though not as thorough, yield results that are sufficiently accurate for certain cases. We have implemented such a simpler method for the simulation of LEIS polar-angle scans that was created by Kim [33], based on a two-dimensional ion trajectory tracing method. The program is coded in the *C Programming Language* and is available in Dr. Kim's Ph. D. dissertation as cited. Slight modifications to the operator interface were made specific to our study.

7.2 Two-dimensional Trajectory Tracing Method

The method of the program successively fires an ion along a line, incrementing steps by an operator chosen increment, into a two-dimensional model of a plane of atoms in the crystal substrate that is perpendicular to the surface. Just as we gather

experimental polar scans in low-index azimuth directions, the models constructed for the simulation are planes of atoms to which (x, y) coordinates are assigned for atom placement mirroring these low-index azimuths. The incident ion searches for a target in this modeled plane and is deflected at a scattering angle computed as a function of the impact parameter of its found target. For each collision event, for any size of deflection angle the incident ion will undergo a loss of energy calculated from the usual relation using the kinematic factor. Having a new trajectory, a new search is done for the next target and the process repeats until the ion leaves the lattice model. As in actual LEIS where backscattered ions enter an electrostatic analyzer at a set angle to the incident ion beam determined by the system hardware configuration, an operator chosen detector angle and corresponding range about this nominal, is chosen. Simulated counts are registered for those trajectories that leave the model lattice within this acceptable simulated detector range.

The model crystal is constructed with approximately 10 atoms across the top and up to 5 rows into the bulk. For our purposes, we found it sufficient to model the lattice planes with about 10 atoms across the top and 3 rows into the bulk since we kept track of collision contributions only from the first three top layers. A schematic of this model with 7 atoms across the top and 5 rows into the bulk is depicted in Figure 7.1 representing the (100) plane perpendicular to the Al(001) surface and whose top row is in line with the [100] azimuth.

In Figure 7.1 we show the range of simulated incident ions directed to the top of this plane. The range of incoming ion trajectories, the width of the beam, is chosen and ions one at a time are directed to the target, each trajectory successively being incremented across the center of the model lattice covering a distance equal to about one lattice spacing. The incident polar angle of the incoming ions (referenced from the Al(001) surface plane) is swept over 90° in operator chosen increments. The

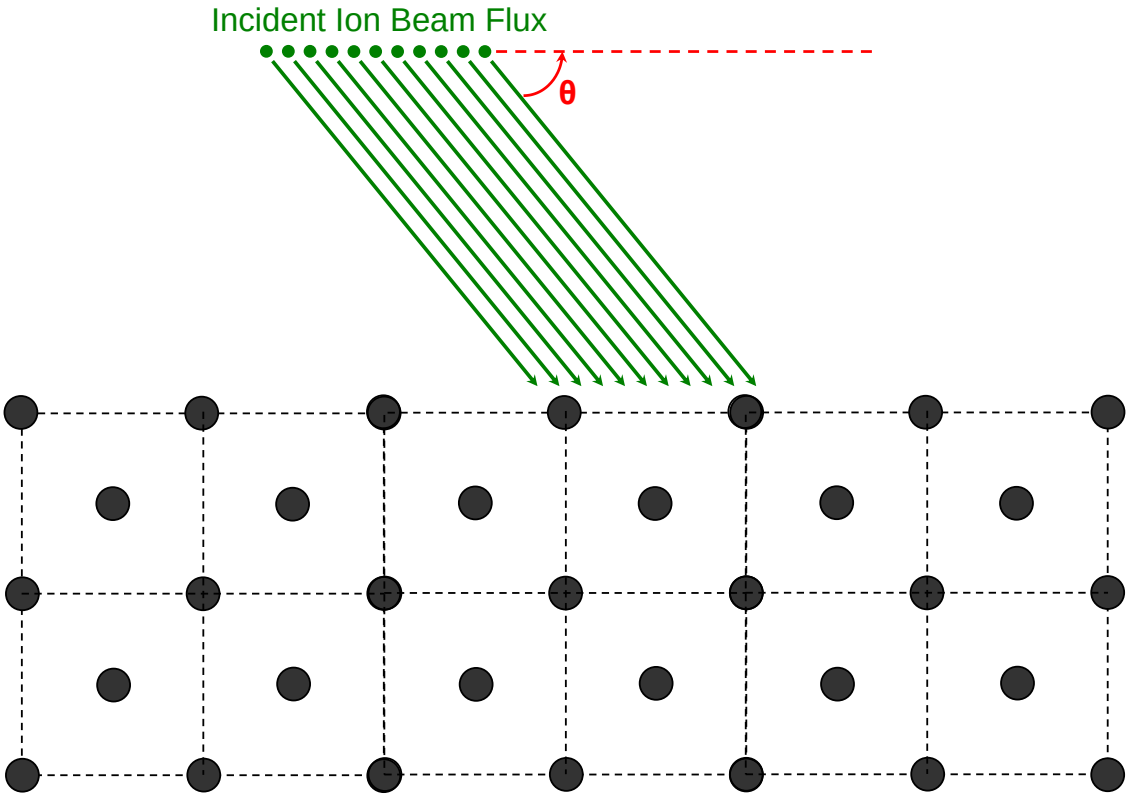

Figure 7.1: LEISsim Al (100) substrate plane model showing incident ion beam in [100] azimuth.

scattering process described above is repeated for each of these incremented incident polar angles.

7.2.1 Magic Formula Expressions and Coefficients

The heart of the two-dimensional trajectory tracing method is finding the scattering angle in the binary collision between the incoming ion and target atom. Analytically, a value for the scattering angle is found by solving the classical scattering integral. This is only practical if the potential of the target nucleus is described by the *Coulomb* potential.

The Magic Formula is a formulation by Biersack, Haggmark, Ziegler, et al. [2, 34] which reduces the scattering collision dynamics between an incident ion and a target atom to an analytical form. In LEIS, the classic scattering integral must be solved numerically to arrive at a solution for the scattering angle, since the potential of the target nucleus is described by a *screened-Coulomb* potential. Using the Magic Formula arriving at a value for the scattering angle as a function of the incoming ion's energy and impact parameter is easily implemented in the given expressions. The Magic Formula expressions and corresponding constant coefficients will be defined and are at the heart of the computing process in the LEISsim program.

In center-of-mass coordinates the value of the scattering angle Θ is found from the solution of the classical scattering integral given by [2]

$$\Theta = \pi - 2\int_{r_{min}}^{\infty} \frac{p\ dr}{r^2\left[1 - \frac{V(r)}{E_c} - \left(\frac{p}{r}\right)^2\right]^{1/2}}, \tag{7.1}$$

where E_c is the energy expressed in the center-of-mass system, p is the impact parameter, r is the separation distance between the incoming projectile and target atom and r_{min} is the distance of closest approach between the two. $V(r)$ is the expression for the screened-Coulomb potential energy.

The classical scattering integral must be solved numerically to find Θ. The Magic Formula reduces the expression for calculating Θ to an analytical form. Figure 7.2 shows the binary collision interaction in center-of-mass coordinates between an an incoming projectile and target atom making use of the 'scattering triangle' as described by Ziegler [2]. From the geometry of the scattering triangle, Θ can be expressed in the following relation

$$\cos\frac{\Theta}{2} = \frac{\rho + p + \delta}{\rho + r_0} \quad \text{, where} \begin{cases} \rho = & \rho_1 + \rho_2 \\ \delta = & \delta_1 + \delta_2 \end{cases} , \tag{7.2}$$

and in the figure

$$\begin{aligned} p &= \text{impact parameter,} \\ \Theta &= \text{center-of-mass scattering angle,} \\ M_1 &= \text{atomic mass of incident ion,} \\ M_2 &= \text{atomic mass of target atom,} \\ r_0 &= \text{distance of closest approach,} \\ \rho_1 &= \text{curvature at closest approach of incident ion,} \\ \rho_2 &= \text{curvature at closest approach of target atom,} \\ \delta_1 &= \text{small correction term for incident ion, and} \\ \delta_2 &= \text{small correction term for target atom.} \end{aligned}$$

The lengths used in Equation 7.2 are converted to dimensionless variables expressed in units of the screening length a by

$$B = p/a, R_0 = r_0/a, R_c = \rho/a, \Delta = \delta/a. \tag{7.3}$$

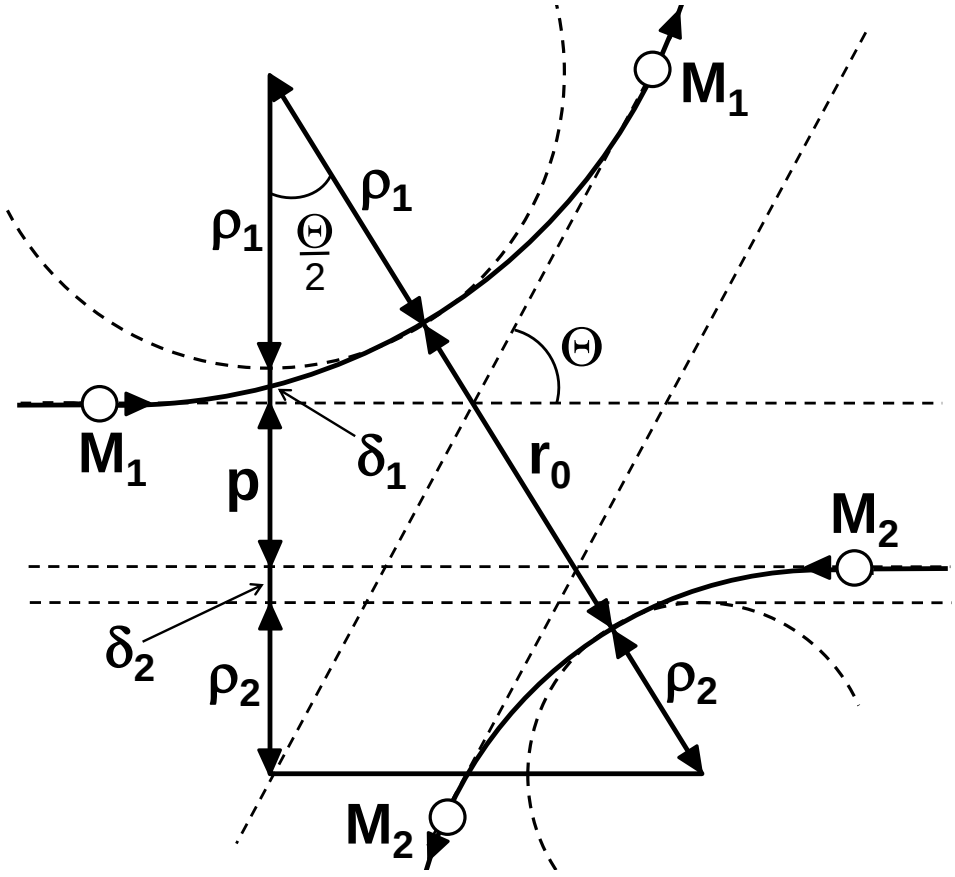

Figure 7.2: Scattering triangle for obtaining expressions to calculate the center-of-mass scattering angle Θ in a binary collision between an incoming ion and stationary target atom, as given by Ziegler [2].

which when substituted into Equation 7.2 gives

$$\cos\frac{\Theta}{2} = \frac{B + R_c + \Delta}{R_0 + R_c}. \tag{7.4}$$

The above equation is the Magic Formula for finding the scattering angle Θ expressed in the center-of-mass frame. Expressions for the terms on the right-hand side of this equation were derived by Biersack and Haggmark [2, 34] by the following steps.

The distance of closest approach r_0 of the ion-target interaction is calculated iteratively as the solution of the scattering angle integrand denominator

$$1 - \frac{V(r_0)}{E_c} - \left(\frac{p}{r_0}\right)^2 = 0, \tag{7.5}$$

where p is the impact parameter, $V(r_0)$ is the interaction screened-Coulomb potential energy evaluated at r_0, and E_c is the the energy available in the center-of-mass (CM) system given by

$$E_c = M_2 E_0/(M_1 + M_2). \tag{7.6}$$

The radius of curvature ρ of the trajectory of the two particles at the point of closest approach is

$$\rho = -2\,\frac{[E_c - V(r_0)]}{V'(r_0)}, \tag{7.7}$$

where $V'(r_0)$ is the spacial derivative of the screened-Coulomb potential energy evaluated at r_0.

Expressing E_c in units of $Z_1 Z_2 e^2/a$ (where a is the *screening length*) gives a dimensionless quantity called he *reduced* energy

$$\varepsilon = \frac{a E_c}{Z_1 Z_2 e^2}. \tag{7.8}$$

The above relations are used to obtain the desired terms in Equation 7.4 and are

$$\begin{aligned} \Delta &= A\,\frac{R_0 - B}{1+G}, \\ A &= 2\,\alpha\,\varepsilon\,B^{\beta}, \\ G &= \gamma\left[\left(1+A^2\right)^{1/2} - A\right]^{-1}, \end{aligned} \tag{7.9}$$

where

$$\begin{aligned} \alpha &= 1 + C_1\,\varepsilon^{-1/2}, \\ \beta &= \frac{C_2 + \varepsilon^{1/2}}{C_3 + \varepsilon^{1/2}}, \quad \text{and} \\ \gamma &= \frac{C_4 + \varepsilon}{C_5 + \varepsilon}. \end{aligned} \tag{7.10}$$

C_1–C_5 are constants fitted to the specific potential screening function used. Two sets of values for the coefficients C_1–C_5 are listed in Table 7.1 for the two screening functions, Molière and Universal.

Table 7.1: Values for constants in Equation 7.10 for the Molière and Universal screening functions [2].

	Molière	Universal
C_1	0.6743	0.99229
C_2	0.009611	0.011615
C_3	0.005175	0.007122
C_4	10.00	14.813
C_5	6.314	9.3066

The final step of the scattering angle calculation, is to convert the scattering angle Θ in the center-of-mass frame to the lab frame scattering angle θ using the expression [2]

$$\theta = \tan^{-1}\left[\frac{\sin\Theta}{(M_1/M_2) + \cos\Theta}\right]. \tag{7.11}$$

7.2.2 Universal Screening Function and Screening Length

Recall the expression for the screened-Coulomb potential energy

$$V(r) = \left(\frac{Z_1 Z_2 \ e^2}{r} \right) \chi(r). \tag{7.12}$$

The Universal screening function $\chi(r)$ as described by Ziegler, et al. [2] is

$$\chi_U(x) = 0.18175e^{-3.1998x} + 0.50986e^{-0.94229x} + 0.28022e^{-0.4029x} + 0.028171e^{-0.20162x}, \tag{7.13}$$

where $x = r/a_{\mathrm{U}}$ and a_{U} is the Universal screening length

$$a_{\mathrm{U}} = \frac{0.8854 \ a_0}{(Z_1^{0.23} + Z_2^{0.23})}. \tag{7.14}$$

The TFM screening function with associated screening length was defined in Chapter 4. We used both the TFM and Universal screening functions with the Magic Formula in the simulation program to find the scattering angles for ion-target interactions. The motivation behind using the TFM screening function was that the original program as designed by Y. W. Kim made use of these parameters. Communication with R. Bastasz [35] regarding simulation of LEIS spectra including ion neutralization effects, led to the implementation of the Universal screening function when neutralization effects were incorporated into the program.

A comparison of the TFM and Universal screening functions can be found in Figure (2-17) in reference [2]. Both are plotted over a wide range of $x = r/a_{\mathrm{U}}$ and in terms of r covers the range of $0 < r \leq 4$ Å. The two functions show a similar shape over this range. Our goal for simulating polar-angle spectra was not to replicate the experimental results, but rather to gain insight into the appearance of peaks at specific angles of the polar scans. A detailed comparison of the effects of using the TFM versus the Universal screening functions is a study suggested for future work and not covered here.

7.3 Simulation Program Components

Three compiled executable program files were used to generate the simulated LEIS polar-angle scan spectra. The first is called *LEISsim* which generates the intial data output in which backscattered ions passed the test of acceptable detection within the operator chosen detection angle range. The second stage is accomplished by *GenOut* which for each incremented value of incident polar angle gives the counts of backscattered ions detected, organized as counts contributed individually by each of the top three layers and the total sum of these three. The counts in each of the layer contributions allows us to keep track of which layer in the substrate was the origin of the primary binary collision that deflected the ion into the detector. The four raw data output spectra from *GenOut* have sharp peaks. Finally the last phase of processing is performing a convolution of the *GenOut* raw data with a Gaussian. This simulates the effects of random vibration of substrate atoms about their nominal positions due to temperature. A short summary of this process will be given below. The interested reader is encouraged to contact the author for a copy of the program code or for any details regarding program operation.

7.3.1 LEISsim Data Output and Convolution

The output of *LEISsim* generates the data file that contains each count of a 'hit' or successful ion-backscattered event into the acceptance angular-range of the detector. After this data is organized by *GenOut* assigning the total hits as a function of originating layer for each step-incremented value of polar incident angle, we have the raw data output simulated spectrum which has sharp peaks corresponding to the lining up of the shadow-cone boundary from a target atom as it intersects its paired-collision atom in the model substrate. In a Monte-Carlo simulation, the

random temperature-dependent fluctuations of positions of atoms in a model crystal are accounted for by assigning a vibrational amplitude to the atoms (usually around 0.1 Å) and program execution thereby randomly varies each atom's position in this way about its nominal value while performing the simulated binary collision dynamics. In our two-dimensional ion trajectory tracing simulation, we model the temperature-vibrational movements of the crystal model atoms more simply by not varying the atomic positions of the substrate atoms, but rather by taking the *GenOut* raw data output and performing a convolution with a gaussian, choosing appropriate values for the angular convolution range, σ (the standard deviation) and μ (the reference zero point on the abscissa).

In Figure 7.3 we show the generated spectra in the simulation process. In this preliminary trial the Molière approximation (TFM) was used for screening function as previously shown in equation 4.12. The associated screening length used was given by Firsov shown in Equation 4.12 which also was scaled by an additional factor called the screening length coefficient C_{SL} as given by Kim [33] and is expressed as

$$C_{\mathrm{SL}} = 0.3284 + 0.04505\,(Z_1 Z_2)^{1/3} + 0.004264\,E_0^{1/2}. \tag{7.15}$$

The raw data output shown in the figure is the sum of all count contributions from the three top layers of the crystal (i.e. individual layer counts are not shown) as generated by GenOut from the initial data output of LEISsim. The smooth curve is the convolution of this raw data with a gaussian, which is similar in shape to actual experimental results.

7.3.1.1 Simulated Ion Beam Step Sizes: As Figure 7.1 suggests, the incident ion beam is composed of ion projectiles directed to the model substrate surface incident over a specific range. Program operation directs a simulated ion trajectory, one

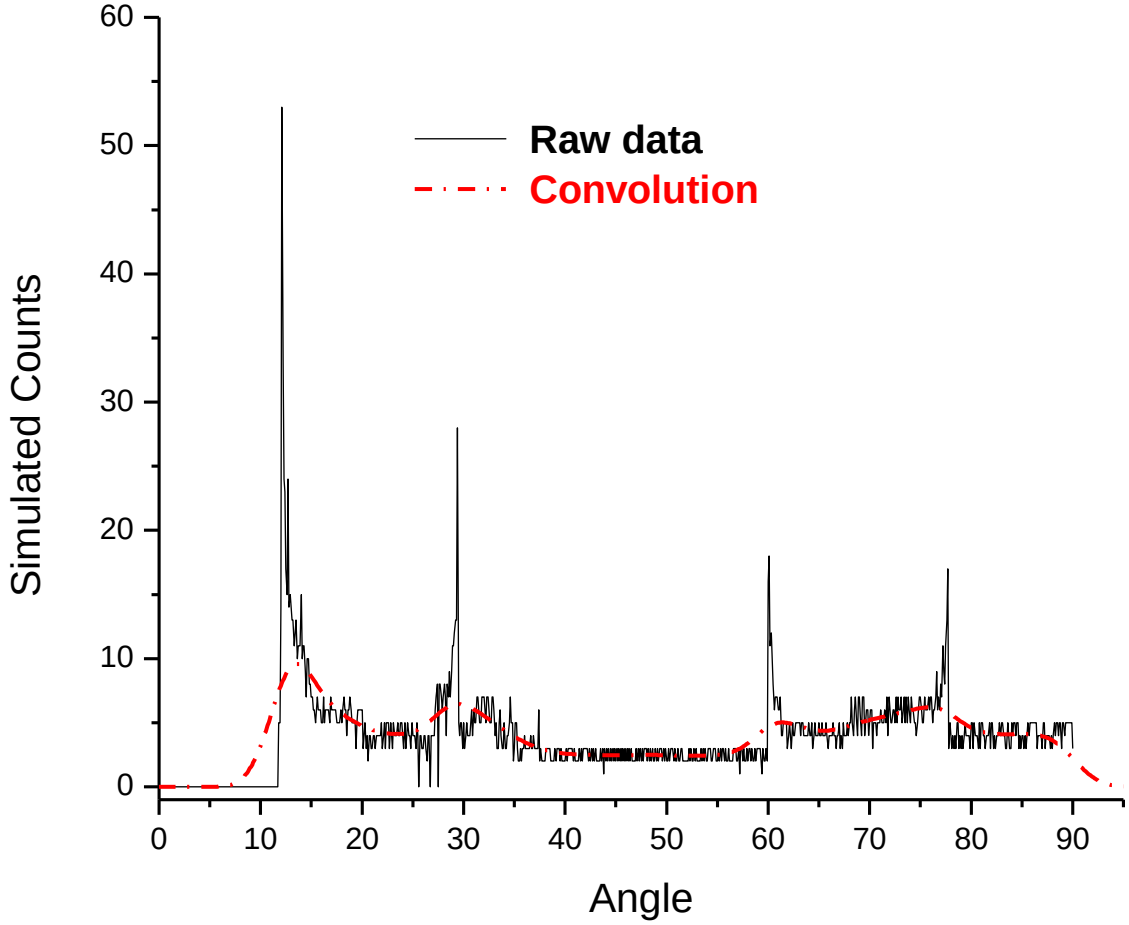

Figure 7.3: LEISsim data output as processed by *GenOut* (spectrum with sharp peaks) and convolution with a gaussian (smooth rounded-peak spectrum) for a simulated polar-angle scan. This simulation was generated for the Al (100) plane, perpendicular to the surface, along the [100] azimuth.

at a time, toward the model substrate surface beginning at a specific position to the left of nominal surface center. The ion undergoes the process of a binary collision with a target atom, detected if backscattered at an acceptable angle, and the next incident ion then repeats the process beginning at a small incremented distance to the right of the previous ion's initial incoming path. The process repeats until the distance covered by the width of the beam is completed. The incremental step, call it d, between successive incident ions can be set by the operator. The range of incident polar angle θ simulated was 0° to 90°. The polar angle θ is stepped in increments of $\Delta\theta$ through this entire range to complete the collecting of counts for creation of the polar-angle scan spectrum.

Running LEISsim with polar-angle step increments of $\Delta\theta = 0.1^\circ$ and an incident ion step size of $d = 0.001$ Å takes about two hours to complete a simulated polar scan. Keeping the same increment for $\Delta\theta$ but changing the ion increment step size to $d = 0.01$ Å, it takes only about 13 minutes to complete the scan. In Figure 7.4 we compare outputs of two runs for these values of step size d, each having been smoothed with 5-point adjacent averaging using the *Origin* software graphical package.

We can see that for testing purposes, for the raw data output in the figure at left, the $d = 0.01$Å normalized spectrum though noisier, follows the $d = 0.001$Å normalized spectrum fairly well. In the figure at right we perform a convolution of the raw data with a gaussian and when properly scaled, the two spectra are nearly indistinguishable. So an incident ion incremental step size of $d = 0.01$Å should be sufficient for our simulation purposes.

The data presented in Figure 7.4 is also a preliminary trial generated using the TFM screening function, Firsov screening length and the Kim screening length coefficient as explained in the previous section. Simulated spectra from this point forward

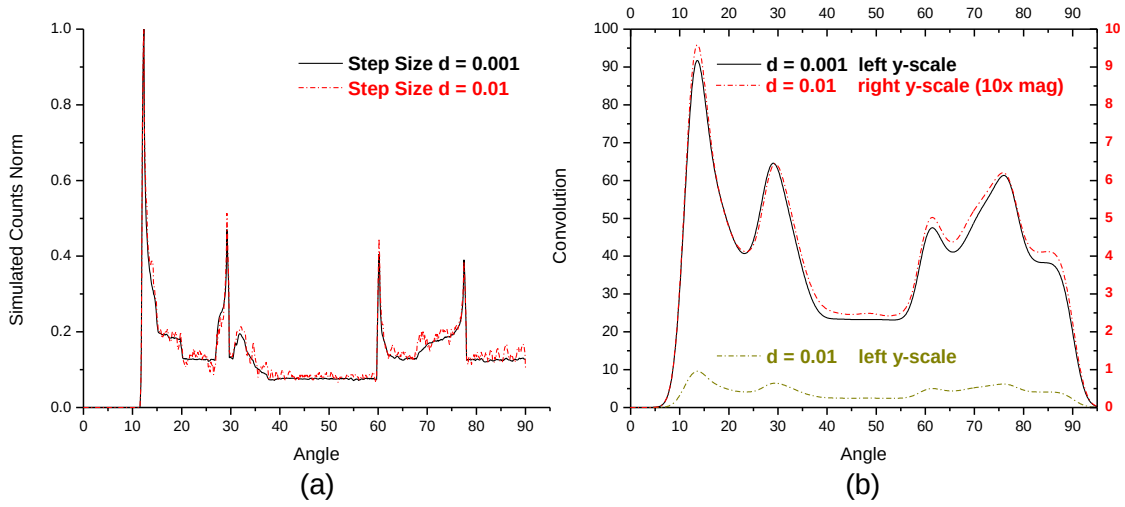

Figure 7.4: Comparing simulated spectrum generated by incoming ion step sizes of $d = 0.001$Å and $d = 0.01$Å. (a) Raw *GenOut* data, (b) Convolution of data with a gaussian.

are generated using the Universal screening function and Universal screening length, without the inclusion of the Kim screening length coefficient given in Equation 7.15.

7.4 LEIS Simulated Polar Scans for the Clean Al(001) Crystal

Al-*fcc* crystal models with approximately 10 atoms across the top and 3 rows into the bulk were created for clean Al in each of the two major low-index azimuths, [100] and [110]. Simulated polar scans were generated using LEISsim for each of these models. The *GenOut* raw data output for the [100] and [110] azimuths will be presented.

Each simulated spectrum is the sum of contributions from the top three rows of atoms in the model substrate planes. Recall from Figure 4.6 that in the [100] azimuth we are looking into the bulk at the Al (010) plane whose top three rows is comprised of atoms from layers 1, 2 and 3. Recall also from Figures 4.7 and 4.8 that in the $[1\bar{1}0]$ azimuth (equivalent structurally to the [110] direction), the (110)

planes perpendicular to the surface are made up of atoms in every-other layer as we go into the bulk and alternate adjacent planes are composed of atoms either in odd-numbered layers or even-numbered layers, i.e. in layers 1, 3 and 5 or layers 2, 4 and 6 respectively. The incoming ion has equal probability of hitting either of these alternate planes. For layer labeling purposes in the [110] azimuth, we will simply call these layers 1, 3 and 5.

7.4.1 Simulated Polar scan in [100] Azimuth

Figure 7.5 is the simulated polar scan in the [100] azimuth before convolution with a gaussian. Major peaks and prominences in the spectrum have been labeled to show which layer or layers contributed to the total counts.

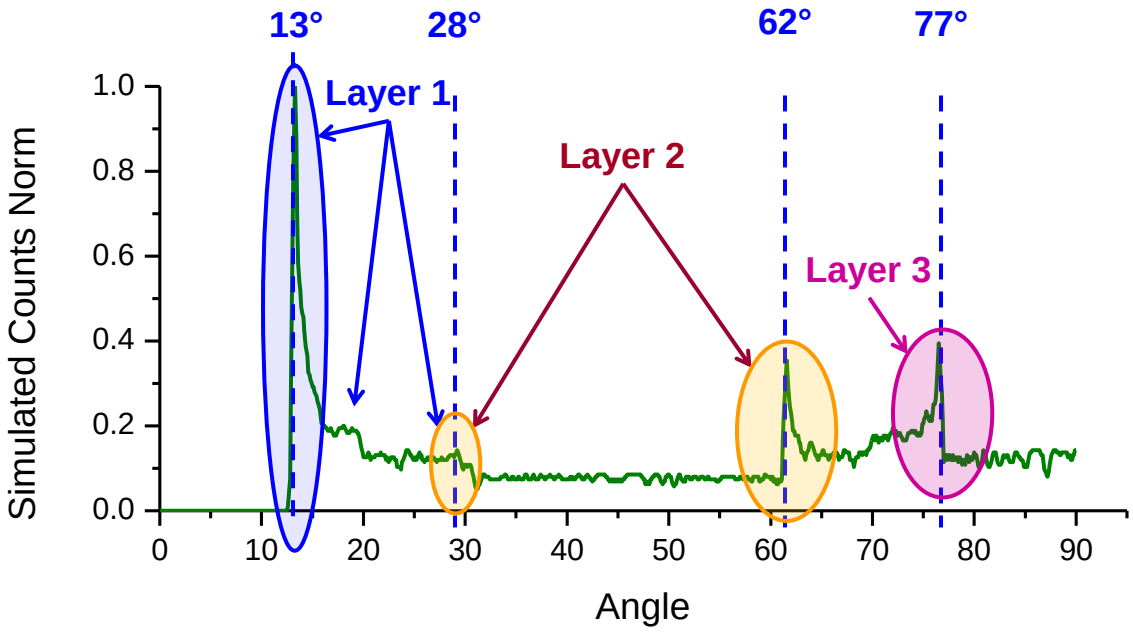

Figure 7.5: LEISsim polar-angle scan in [100] azimuth, spectrum is the sum of contributions from the top three layers (1, 2, 3).

7.4.2 Simulated Polar scan in [110] Azimuth

A repeat of the above process was done for the [110] azimuth with corresponding results depicted in Figure 7.6. As in the previous section, major peaks and prominences in the spectrum have been labeled to show which layer or layers contributed to the total counts.

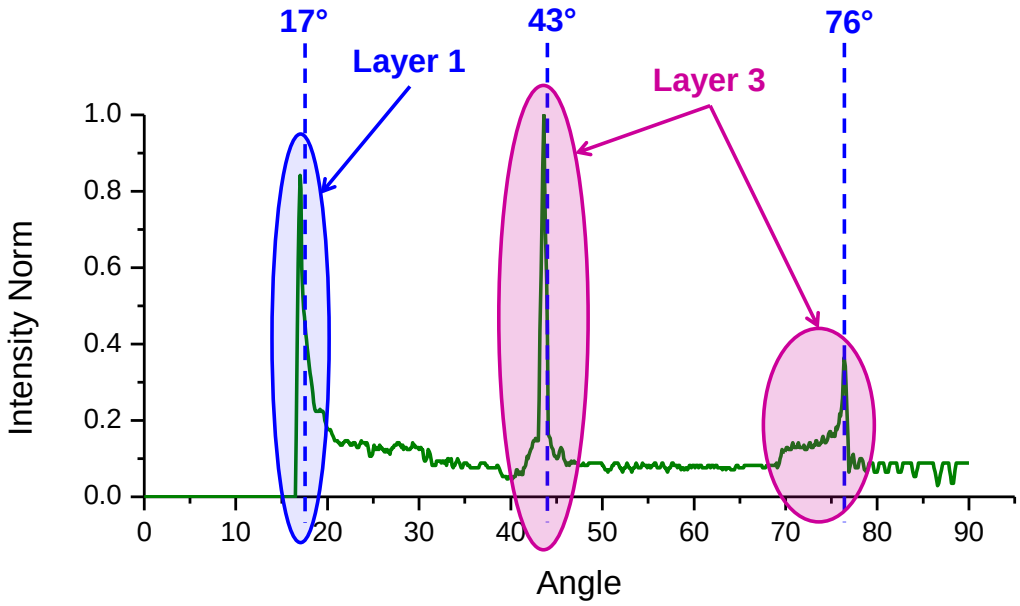

Figure 7.6: LEISsim polar-angle scan in [110] azimuth, spectrum is the sum of contributions from the top three layers (1, 3, 5).

7.5 Simulations Accounting for Neutralization Effects

LEISsim has the option of generating simulated LEIS polar-angle scans by taking into account neutralization of the incident ion from the top three layers of the substrate model. We used the method of R. Bastasz [35] of assigning a *neutralization constant* N (where $0 < N \leq 1$) to each collision event. If the event experiences an angular deflection at or greater than a user specified value and if detected the weight

of the event is adjusted by multiplying its count by N. If in its trajectory, the same ion experiences additional such deflections the final weight of its count is multiplied by N^i where i is the number of such deflections encountered before being detected. Thus this simulates the lesser probability of an ion staying ionized. In the experimental setup, an ion will either stay as an ion or become neutralized. Statistically in the actual experimental spectrum the counts collected are thereby affected by the probability of ion neutralization. Recall that this neutralization value is a function of the incident angle of the incoming ion with the plane of the target surface, as well as the layer of the substrate in which the collision event takes place [21]. The program does not take into account the former possibility, but only addresses the latter, by allowing a different value of N to be specified for each of the top three layers of the target substrate. Thus for a large number of counts collected, the neutralization processes, experimental and simulated, though different, should have a similar effect on the final output spectrum.

In this section we complete the process of simulation by performing a convolution of the raw data output with a gaussian.

7.5.1 Simulated Polar scan in [100] Azimuth

Let us now look at results of simulation for the clean Al(001) surface in the [100] azimuth.

It was found that the best combination of parameters needed to simulate an actual experimental spectrum was to use values for the neutralization constants of $N_1 = 0.9,\ N_2 = 0.9$ and $N_3 = 0.1$ for model substrate layers 1, 2 and 3 respectively in the [100] azimuth. Thus the contribution by the 1^{st} and 2^{nd} layers are reduced equally by a factor of 0.9 while the 3^{rd} layer's contribution is reduced by 10 times the original.

The convolution parameters used an angular convolution range of $\pm 10°$, $\sigma = 3.0$ and $\mu = 0.0$.

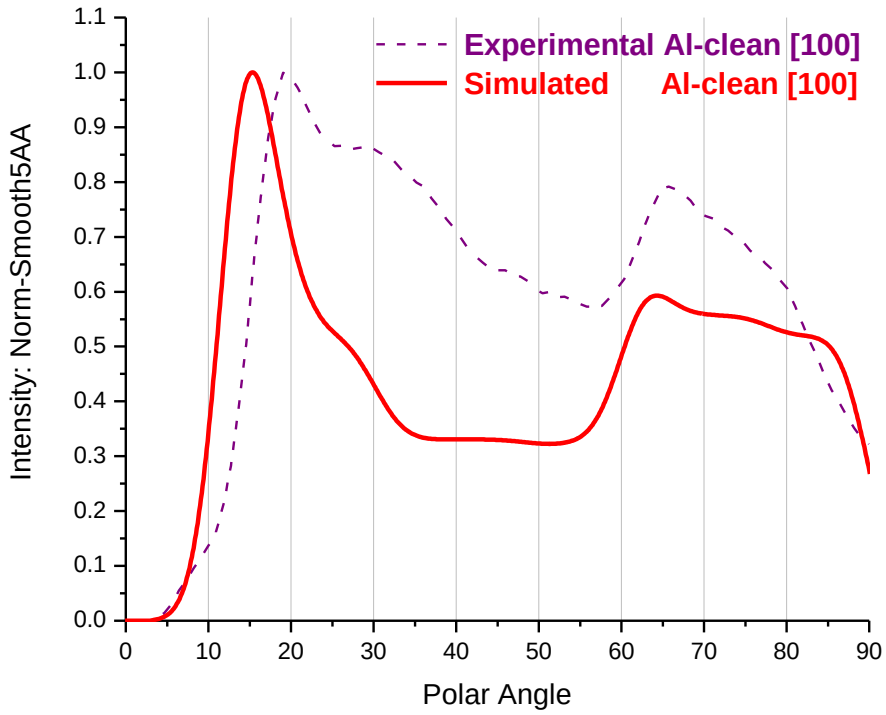

Figure 7.7: Simulated Al-clean polar-angle scan in the [100] azimuth as compared to a typical corresponding experimental spectrum.

Figure 7.7 shows the simulated polar-angle scan in the [100] azimuth compared to its corresponding standard experimental Al-clean signal. Though portions of the simulated spectrum vary greatly in height from the experimental counterpart, its general shape is similar and is something with which we can work.

7.5.2 Simulated Polar scan in [110] Azimuth

We now give the corresponding results of simulation for the clean Al(001) surface in the [110] azimuth.

The same gaussian convolution parameters were used in this azimuth as previously used. The neutralization constants were adjusted for best agreement with experimen-

tal spectra. The constants used were $N_1 = 0.9, N_3 = 0.2$ and $N_5 = 0.02$ for model substrate layers 1, 3 and 5 respectively (or layers 2, 4 and 6 for alternate planes) in the [110] azimuth. Recall in the [110] azimuth, the family of {110} planes are comprised of every other layer going into the bulk.

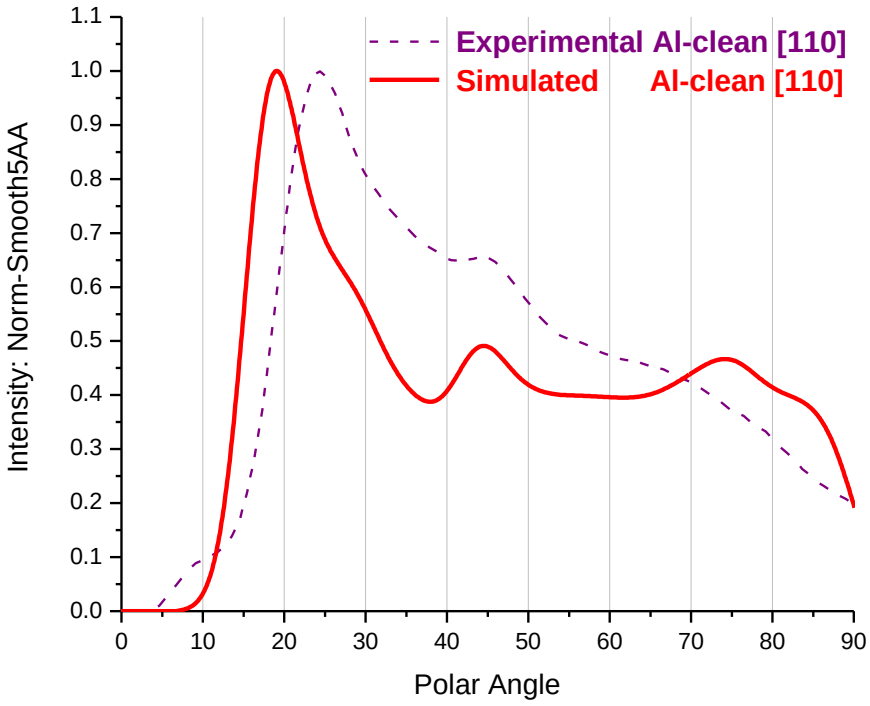

Figure 7.8: Simulated Al-clean polar-angle scan in the [110] azimuth as compared to a typical corresponding experimental spectrum.

Figure 7.8 shows the simulated polar-angle scan in the [110] azimuth compared to its corresponding standard experimental Al-clean signal. Once again portions of the simulated spectrum vary greatly in height from the experimental counterpart, but its general shape is similar.

7.6 Motivation for Using Simulated LEIS Spectra

The motivation for generating LEIS polar-angle simulated spectra in both the low-index major azimuths, is to use Al-clean models as standards of comparison for cases in modeling TM's deposited onto the the Al(001) surface. The neutralization coefficients found that gave the best match of simulated spectra to experimental spectra for the clean Al surface, will be kept for the case of modeling TM deposition onto Al(001).

Model crystals will be considered for Ti atoms present in the first three layers of the Al crystal, placed at specific Al lattice sites to test if a simulation can generate a spectrum which closely matches LEIS experimental data. This will be done for both low-index azimuths. The results of this simulation procedure will be found in the analysis section for Ti on Al(001).

CHAPTER 8

STRUCTURE OF ULTRA-THIN TI FILM ON THE AL(001) SURFACE

8.1 Introduction

Metal-on-metal interfaces have been studied extensively in an effort to understand the interaction between metals in alloying or their reluctance to alloy, and in epitaxial growth of deposited species. The structure of Ti on the Al(001) crystal surface however, is not well understood. Accordingly, experimental and theoretical studies have attempted to shed light on this structure. Resent interests in chemical storage of hydrogen in solid materials such as sodium alanate ($NaAlH_4$) has motivated the investigation of the role of Ti as a catalyst in such applications. O. Kircher, et al. [13] have performed experimental work with $NaAlH_4$ doped with different concentrations of a Ti-based catalyst to study the kinetics of the decomposition of the alanate. S. Chaudhury, et al., have added to the field of study, a theoretical treatment of Ti as a catalyst for hydrogen storage in sodium alanate [36]. Their theoretical model places Ti at next-nearest neighbor lattice sites on a quasi-hexagonal reconstructed Al(001) surface, which catalyzes hydrogen atoms to occupy spaces between Al atoms. R. Stumpf, et al. [22] have combined experimental work and DFT calculations to study the effects of adsorbed hydrogen on the stability of Ti atoms on Al surfaces, the results of which can apply to the effectiveness of Ti as a catalyst in the absorption of hydrogen in alanate hydrogen storage media.

This work is a follow up on previous work by our group studying the structure of Ti on the Al(001) surface [28, 29]. Whereas the previous work focused on Ti coverages up to 10 ML, this work focuses on the structural characteristics of Ti on the Al(001) surface for sub-monolayer and above but near 1 ML Ti coverage, and includes

experimental results from LEED and LEIS with subsequent analysis. Previous work done by Kim, et al., has suggested from partial QLEED (quantitative low-energy electron diffraction) results that low-coverage depositions of Ti onto Al(001) may find Ti atoms residing in the second layer of the substrate [37]. The work by R. Stumpf cited above, found similar results from their DFT calculations. D. Spišák, et al. [6] proposed five theoretical models for Ti on Al(001) in a study using an ab-initio density-functional method which show Ti atoms replacing Al atoms in their original *fcc* lattice positions in the first few top layers of the ideal Al(001) crystal surface. These five models will be considered together with the analysis of experimental LEIS spectra to assist in determining a workable surface-structure model which is consistent with experimental results.

Figure 8.1 shows the five proposed models from the Spišák study [6]. All models show various configurations of one mono-layer (ML) of Ti on the Al(001) surface, the most favorable model being Model 5. These models will be discussed in the context of our data and a new model consistent with our results will be proposed in Section 8.4.

Analysis of LEIS spectra will be based on ion-target interactions under a screened-Coulomb potential [21], making use of geometrical shadow cone analysis explained in Chapter 4. The treatmant of this Ti-Al system will primarily focus on the use of LEIS and LEED in the analysis of surface layer structure. Both LEIS [19] and LEED are highly surface sensitive techniques. Thus only the top few layers of the crystal substrate were considered in the analysis.

8.2 Experiment

Experiments were done in an ultra-high vacuum (UHV) chamber with a base pressure of 5×10^{-10} Torr sustained by an 8" flanged triode ion pump with pumping

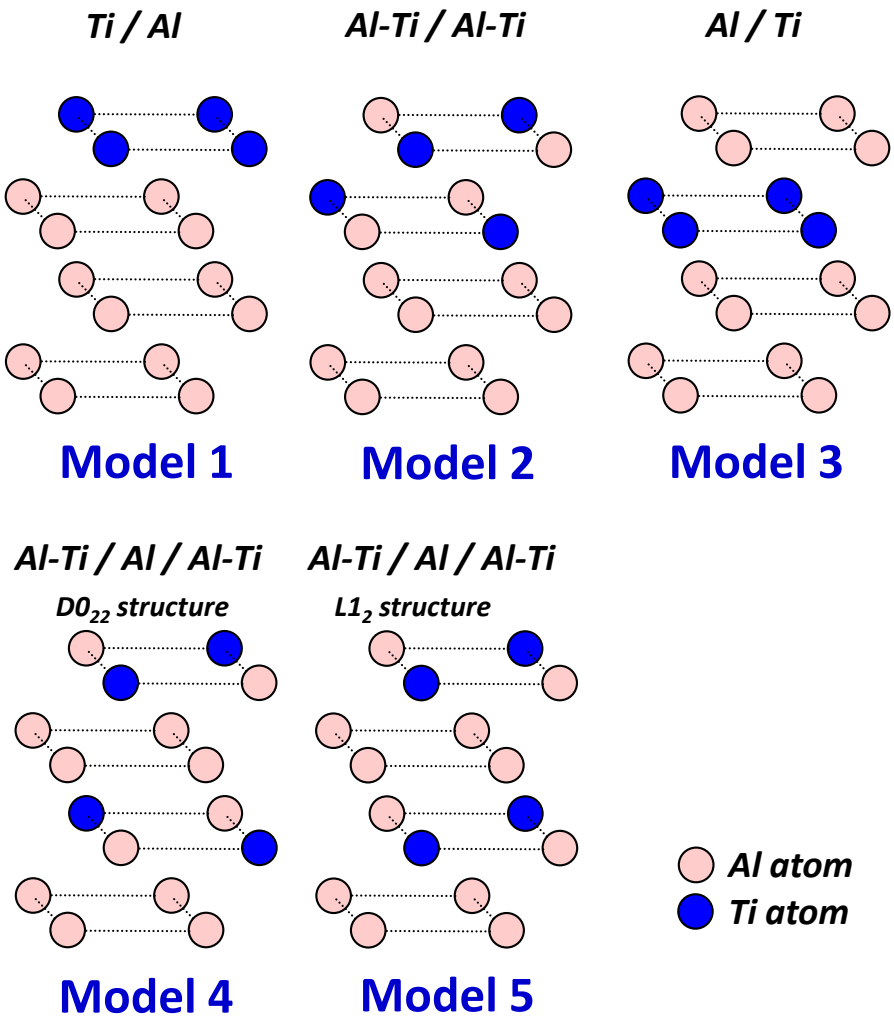

Figure 8.1: Theoretical models of Ti on Al(001) proposed by D. Spišák and J. Hafner [6].

speed of 220 l/s and a 6" flanged turbo pump with pumping speed of 230 l/s. The chamber was equipped with a quadrupole residual gas analyzer, a 6" reverse-view LEED optics instrument, and an LEIS ion gun and controller with associated 100 mm hemispherical electrostatic energy analyzer (VSW HA-100).

The three-axis goniometer as described in Section 2.4 was used for sample positioning. The sample is our Al(001) crystal. Ti deposition onto the Al(001) crystal surface was accomplished via evaporation using a resistively heated wire filament, composed of three W wires (0.2 mm in diameter) braided together, and then wrapped with a Ti wire (0.25 mm in diameter).

Prior to Ti deposition, the sample surface was cleaned with repeated Ar^+ sputtering at an incident ion-beam energy in the range 1.2 – 1.3 keV and current of about 0.5×10^{-6} amps, until LEIS energy spectra showed no evidence of oxygen contamination. Following Ar^+ sputter cleaning, the sample was annealed at a temperature in the range of 400–425°C for greater than 10 minutes. After cooling to < 50°C, to check the condition of the Al(001) surface, LEED was performed to insure that a sharp p(1×1) pattern was present. Ti deposition was carried out nominally at room temperature at chamber pressures in the range of approximately 1–5 $\times 10^{-9}$ Torr. Photographs of LEED images were taken for the clean Al(001) surface as well as for the post Ti-deposited surface when a faint c(2×2) image was observed.

LEIS was configured as explained in Section 4.2. Ion currents were kept in the range of 20–30 nA in order to minimize the damage to the sample surface which occurs from sputtering by the incident He^+ ion beam.

As previously described, three types of LEIS spectra were collected, energy, azimuth-angle and polar-angle scans.

LEIS energy scans were collected at a fixed polar angle of 45° and a fixed azimuth angle placing either of the two low-index direction vectors, [100] or [110], in the horizontal plane.

Azimuth-angle scans were collected at a fixed polar angle of 12° with respect to the sample surface plane. The goniometer azimuth angle setting was varied through a range of approximately 135° in a CCW direction as we look into the bulk. A DC motor was used to sweep the azimuth angle at a regular rate of about 4°/min. For plotting azimuth-angle scan spectra, we defined the azimuth angle to be the angle that the sample surface [100] direction vector makes with the horizontal scattering plane, thereby arbitrarily denoting the 0° position when this vector passes through this plane.

Polar-angle scans were collected for each of the two low index azimuth directions ([100] and [110]) when they respectively were oriented parallel to the horizontal plane. The goniometer polar angle setting was varied through the scanning range from 0° to 90°. The plotted data sets found in this discussion are smoothed versions of the original data. A 5-point or 25-point Adjacent-Averaging smoothing method provided in the *Origin* graphing software package (v.8.0, *OriginLab Corporation)* was used. Plotted azimuth- and polar-angle scans have been normalized by dividing by the respective maximum count collected for each spectrum. We define a scaling factor η for comparing signal strengths of un-normalized smoothed spectra as

$$\eta_{\alpha} = \left(\frac{C_{\alpha}}{C_{Al\text{-}clean}}\right)\left(\frac{I_{Al\text{-}clean}}{I_{\alpha}}\right), \tag{8.1}$$

where C_{α} is the un-normalized spectrum maximum count for the α signal and I_{α} is its corresponding nominal sample current observed while collecting spectrum counts. The scaling factor gives us a sense of the signal strength of a particular spectrum as

compared to the corresponding clean Al(001)-surface reference signal ($\eta_{Al\text{-}clean} \equiv 1$). Rather than just comparing two signal strengths using their respective un-normalized maximum, including the inverse relation to sample current gives a truer comparison, especially for spectra taken in different experimental sessions.

In our discussion, for Ti deposited on the Al(001)surface, LEIS azimuth- and polar-angle scan spectra collected at the fixed energy corresponding to the element Al will be referred to as the *Al-peak* signal and that for Ti as the *Ti-peak* signal. For the condition of a clean Al(001) surface, the spectra collected will be referred to as the *Al-clean* signal.

RBS analysis was performed to find the coverage of Ti on the Al(001) surface. A He^+ ion beam at a nominal energy of 1.3 MeV was directed to the sample surface and spectrum counts were collected using a silicon surface barrier detector positioned at a backscattering angle of 112°. The sample surface normal was oriented at approximately 22° with respect to the ion beam to minimize channeling effects. In the discussion to follow, one set of LEIS azimuth-angle scans and two sets of polar-angle scans are used. The RBS measurement for the azimuth-angle scan data set gave a Ti coverage of 0.8 ML. For the first set of polar-angle scans, RBS results gave a Ti coverage of 0.7 ML. For the second set of polar-angle scans, our van de Graaff accelerator was not in operation during the time of LEIS data collecting, and we will offer an argument for claiming that the Ti coverage to be of at least 1 ML by comparing LEIS spectrum yields for the post Ti-deposited surface to those for a clean Al(001) surface. For each data set, the presence of a c(2×2) LEED pattern was observed after Ti deposition.

8.3 Results

8.3.1 LEED

Figure 8.2(a) and (b) show LEED images for a clean Al(001) surface and for Ti deposited on the Al(001) surface respectively. The appearance of the faint c(2×2) pattern in Figure 8.2(b), allows us to infer that Ti is likely present at alternate Al lattice sites. In our work with Ti deposited on the Al(001) surface, LEED results showed evidence of a c(2×2) pattern for Ti coverage ranging from 0.8 ML to 3.1 ML as determined by RBS. The data sets collected for this discussion have Ti coverage within this range. The lack of sharpness and clarity in the spots forming the c(2×2) pattern, was present in all such LEED images we observed. This leads us to conclude that a structure needed to support a c(2×2) pattern is only partially developed, but yet undeniably present. The greater portion of our analysis was focused with this c(2×2) pattern in mind.

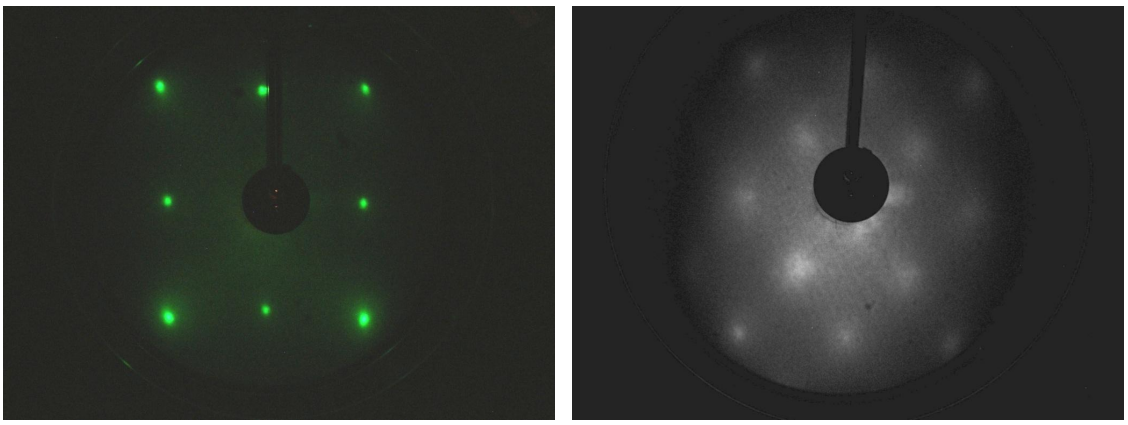

Figure 8.2: Two LEED images, (a) clean Al(001) at 83.0 eV LEED-electron energy, (b) ≈ 2.4 ML Ti on Al(001) showing a faint c(2×2) pattern at 86.7 eV LEED-electron energy.

8.3.2 LEIS

8.3.2.1 LEIS Energy Scans: Two typical LEIS energy scans are shown in Figure 8.3. For these scans an incident beam of He^+ ions at a nominal energy of 1.0 keV was directed to our sample surface. The analyzer acceptance energy was swept from 300 eV to approximately 800 eV and counts of backscattered ions were collected. Peaks appear in the spectra at energies corresponding to backscattered ions from the constituent elements found at or near the surface of the sample under test.

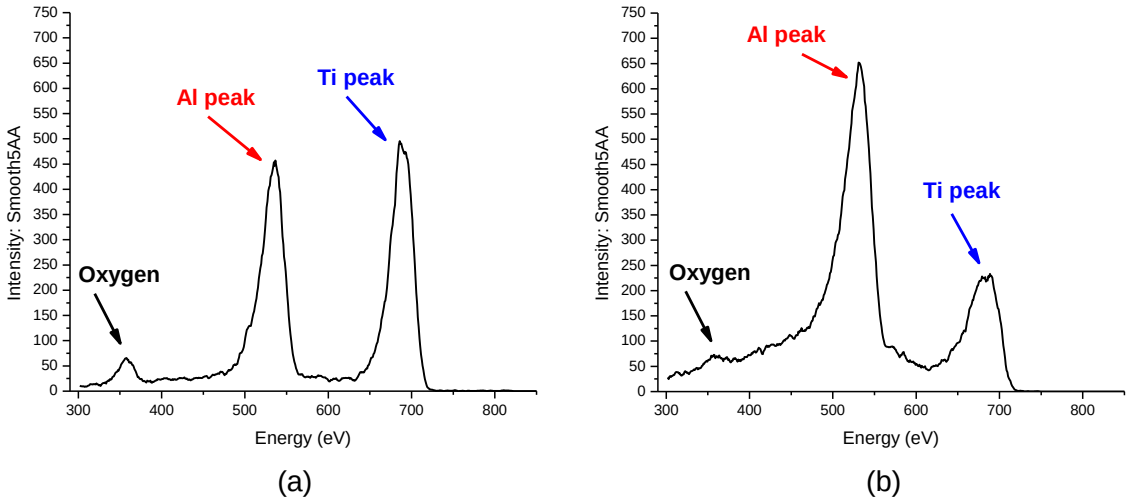

Figure 8.3: LEIS energy scan spectra post Ti deposition on the Al(001) crystal surface; (a) 0.8 ML Ti, [100] azimuth, (b) 0.7 ML Ti, [110] azimuth.

The Ti coverage as determined by RBS for the spectra in Figure 8.3(a) and (b) was 0.8 ML and 0.7 ML, respectively. Both scans were collected at a polar angle of 45°; the spectrum in (a) collected in the [100] azimuth with sample current $I_s = 24$ nA, and the other in the [110] azimuth with $I_s = 22$ nA. Note the height of the peak corresponding to the element Ti as compared to that for the element Al in the two scans. Though both scans have similar Ti coverage, the ratio of counts of ions backscattered from Al to those from Ti vary significantly. Because LEIS is a highly surface sensitive technique, arriving at quantitative values for metal deposition

coverage onto a substrate base is not a clear-cut calculation. To begin with, atoms of the deposited species may reside in layers below those visible to LEIS. In addition, incident-ion neutralization probabilities for the visible layers (at or just below the surface) are dependent upon the incoming ion angle of incidence and upon the azimuth angle position of the crystal surface [21]. Moreover, structure related effects due to shadowing and blocking, influence backscattered ion count intensities, especially in low-index azimuthal directions, at which the two scans depicted in Figure 8.3 were made. Due to these complications we rely on RBS measurements when available for metal deposition coverage determination. We do nevertheless, qualitatively get a sense of relative Ti coverage, using successive energy scans collected at similar parameter settings [22], from the rise in the intensity of the Ti peak as deposition continues.

8.3.2.2 LEIS Azimuth-angle Scans: Figure 8.4 illustrates a set of collected azimuth-angle scan spectra. The He^+ incident ion beam directed to our sample surface had a nominal energy of either 1.0 or 1.2 keV. Three curves are shown, the Al-clean signal, the Al-peak signal and the Ti-peak signal. Ti coverage as determined by RBS for the Al- and Ti-peak data sets was 0.8 ML. The scale factor η values for each spectrum are shown (see legend), giving a comparison of the strengths of the Al- and Ti-peak signals to the Al-clean signal. Valleys at particular azimuth directions are labeled, which occur due to shadowing of crystal surface atoms from the incident ion beam as they become aligned in rows behind target atoms. Peaks occur due to the focusing effect of incident ions at the boundary of the shadow cone as this boundary intersects collision atoms in their ordered rows. Note the clear valleys in the spectrum in the [100], [110] and [310] azimuth directions. Note also the clear

four-fold symmetry of the Al-clean signal whose signal shape repeats every 90°. The asymmetry of the Al-clean signal we believe is due to wobble of the Al(001) crystal surface which changes the angle of incidence of the ion beam as the azimuth angle is varied over the angular range of the scan. This same four-fold symmetry can be seen in both the Al- and Ti-peak signals, even though the signal quality of both is weaker in comparison to the Al-clean signal as the scale factor η values illustrate. The cause of an additional asymmetry in the intensities of the Al- and Ti-peak signals that occurs at the right side of the spectrum is unknown, though we speculate might be due to drift in experimental parameters.

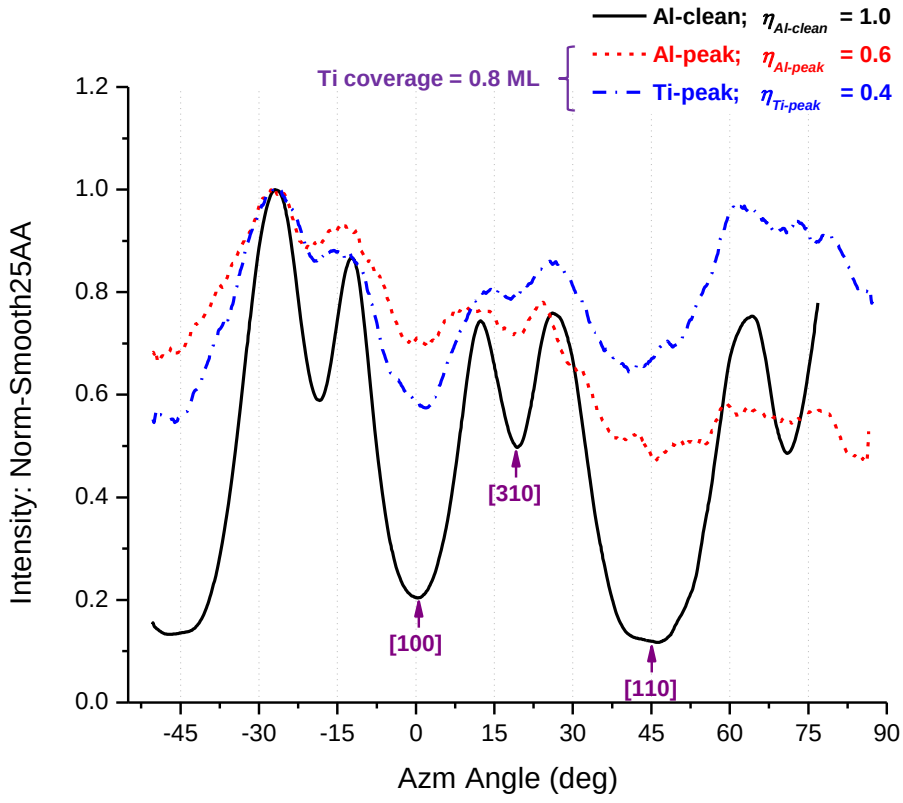

Figure 8.4: Azimuth-angle scan spectra, Al(001) surface collected at a 12° polar angle, showing the Al-clean scan (taken at an incident ion energy of 1.2 keV), and the Al-peak and Ti-peak scans (0.8 ML Ti, taken at an incident ion energy of 1.0 keV).

The matching symmetry of the Al-peak signal to the Al-clean signal allows us to conclude that the *fcc*-cubic lattice structure characteristic of clean surface Al atoms is not disrupted due to the addition of Ti atoms onto the surface. The symmetry of the Ti-peak signal supports the premise that the Ti atoms arrange themselves also into a cubic structure. This cubic symmetry for both the Al- and Ti-peak signals is in disagreement with the hexagonal-type structure suggested in the literature by S. Chaudhuri, et al. [36] mentioned earlier. This is also corroborated by our c(2×2) LEED image, which gives no evidence of a hexagonal pattern. Since we have collected these spectra at a glancing value for the polar angle, the intensity of each signal is primarily due to backscattered ions coming from the surface layer of the substrate which leads us to the conclusion that at 0.8 ML Ti coverage, we have some Ti atoms present in the 1^{st} layer of the substrate. The possible presence of below surface Ti atoms will be addressed by using results from polar-angle scan spectra.

8.3.2.3 LEIS Polar-angle Scans (sub-monolayer Ti coverage): Figure 8.5(a) depicts the (100) crystal plane at a side view of the crystal along the [100] azimuth. This plane is perpendicular to the crystal surface whose top row is made up of the surface atoms in the [100] azimuth direction. At the left side of the figure are label references for the substrate layers beginning with the surface as layer *1*, and proceeding downward into the substrate bulk. Note also the depiction of the two-dimensional slice of the shadow cone (not drawn to scale) created by the interaction of the incident He^{+} ion with its initial target atom located in the 1^{st} (surface) layer. The focusing effect at the shadow cone boundary gives rise to a high density ion flux which can potentially intersect substrate paired collision atoms labeled a, b, c, d and e.

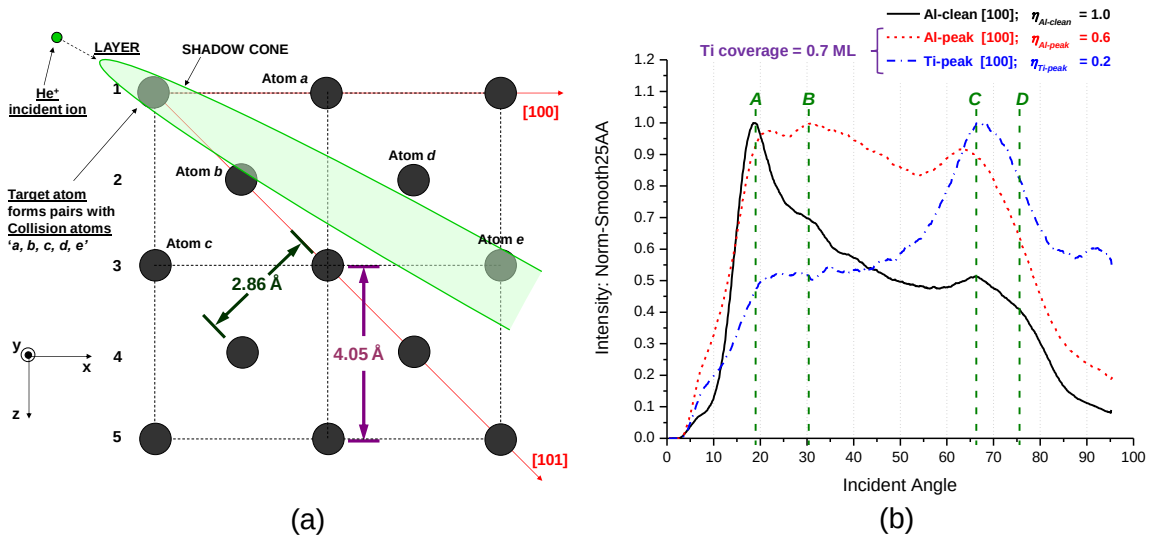

Figure 8.5: (a) The Al(100) crystal plane, perpendicular to surface plane. (b) LEIS polar-angle scan spectra in the [100] azimuth for the clean Al(001) surface and for 0.7 ML Ti on the Al(001) surface.

In Figure 8.5(b) we show the resulting spectra from LEIS polar-angle scans taken in the fixed [100] azimuth for the case of 0.7 ML Ti coverage. The Al-clean signal, plotted on the same axes, will be our baseline reference signal with which to analyze the post Ti-deposition Al- and Ti-peak signals. Shown are the smoothed and normalized spectra data as well as the scale factor η values (see legend) for each spectrum. Note the four dotted reference lines A–D located at the approximate position of major peaks or prominences in the Al-clean signal spectrum. Geometrical shadow cone analysis was used to analyze these peaks, the results of which are shown in Table 8.1 which lists the layer number and collision atom (in parentheses) from which the backscattered ions could originate. All entries in the table are based on the interaction of the incoming ion with the upper-left-most atom as target and origin of the shadow cone as depicted in Figure 8.5(a).

The lack of a strong peak in the Ti-peak polar scan at reference line A, as compared to that for the Al-clean and Al-peak signals, suggests relatively less Ti atoms present

Table 8.1: [100] azimuth, contributing layer and collision atom for Al-clean scan reference-line peaks. Refer to peak labels in Figure 8.5(b).

Peak [100]	**Contributing Layer & (Atom)**
A	1 (a); 3 (e)
B	2 (b, d)
C	2 (b)
D	3 (c)

in the 1st layer of the crystal substrate, while the prominence at line C indicates a relatively greater presence of Ti atoms in the 2nd layer. In view of only the top two layers, DFT calculations by D. Spišák, et al. [6], found that the crystal configuration with an Al surface layer (Figure 8.1, Model 3) to be more favorable compared to that with the Ti surface (Figure 8.1, Model 1). These two models suggest the AlTi $L1_0$ crystal structure, whose alternating layers are fully composed of either Al or Ti atoms. In light of this assertion, given the Ti coverage value of 0.7 ML for this set of polar scans, the lesser strength of the Ti-peak signal compared to the Al-peak signal ($\eta_{Ti-peak} = 0.2$ and $\eta_{Al-peak} = 0.6$) is consistent with this idea since LEIS is highly surface sensitive and neutralization of backscattered ions becomes progressively greater as below-surface layers are traversed. We believe this collection of arguments adds credence to the likelihood that Ti atoms prefer sub-surface occupancy.

The initial rise in the Ti-peak signal at A does suggest the presence of some 1st layer Ti atoms, and the sustained intensity level at D suggests the presence of Ti atoms in the 3rd layer as well. Due to the strength of the prominence at line C in the Ti-peak signal however, we infer that Ti atoms have populated the 2nd layer more so than the 1st layer. Theoretical support for this assertion can be found in a recent work by R. Stumpf, et al. [22]. Their DFT calculations showed that for $\frac{1}{2}$ ML Ti coverage on Al(001) the most stable configuration finds the Ti atoms in the 2nd layer in a c(2×2) substitutional array, with $\frac{1}{4}$ ML Al adatoms on the surface at fourfold

sites directly above 2nd layer Ti atoms. For a 1 ML Ti coverage, the lowest energy configuration has $\frac{1}{2}$ ML Ti in the 2nd and 4th layers in the $L1_2$ structure, along with the $\frac{1}{4}$ ML of Al adatoms positioned as before. In this same work with DFT analysis, the presence of H as a stabilizing effect on deposited sub-monolayer coverage of Ti on the Al(001) surface was also investigated. The most energetically favorable H-stabilized structure for a $\frac{1}{2}$ ML Ti coverage, has Ti atoms in the 2nd layer with 1 ML H on the surface at Al atom bridge sites. For a 1 ML Ti coverage, the most stable arrangement has $\frac{1}{2}$ ML Ti in the 2nd and 4th layers but now with $D0_{22}$ stacking and 1 ML surface H atoms positioned in in a specific configuration illustrated in the cited reference.

Figure 8.6(a) depicts a schematic of the (110) crystal plane. This plane is perpendicular to the crystal surface whose top row is made up of surface atoms in the [110] azimuth, in which direction the goniometer was fixed for this set of polar scans. Note the reference labels of the substrate layers at the left side of the figure. The surface layer is labeled *1, 2* and the lower two layers are labeled *3, 4* and *5, 6* respectively. Recall, that the {110} family of vertical planes are comprised of atoms from odd-numbered or even-numbered layers giving the incident ion beam an equal probability of targeting top row atoms in either the 1st or 2nd layer.

In Figure 8.6(b), for the same 0.7 ML Ti deposition, we now plot the smoothed and normalized Al- and Ti-peak signals resulting from an LEIS polar-angle scan in the [110] azimuth direction, as well as the Al-clean signal. A new set of reference lines A–D mark the positions of peaks and prominences in the Al-clean signal for comparison to the Al- and Ti-peak signals. The scale factor η values for each spectrum, are also shown in the legend. For each reference line, Table 8.2 lists the contributing layers and corresponding collision atoms (in parentheses) from which backscattered ions could originate. All entries in the table are based on the interaction of the incoming ion

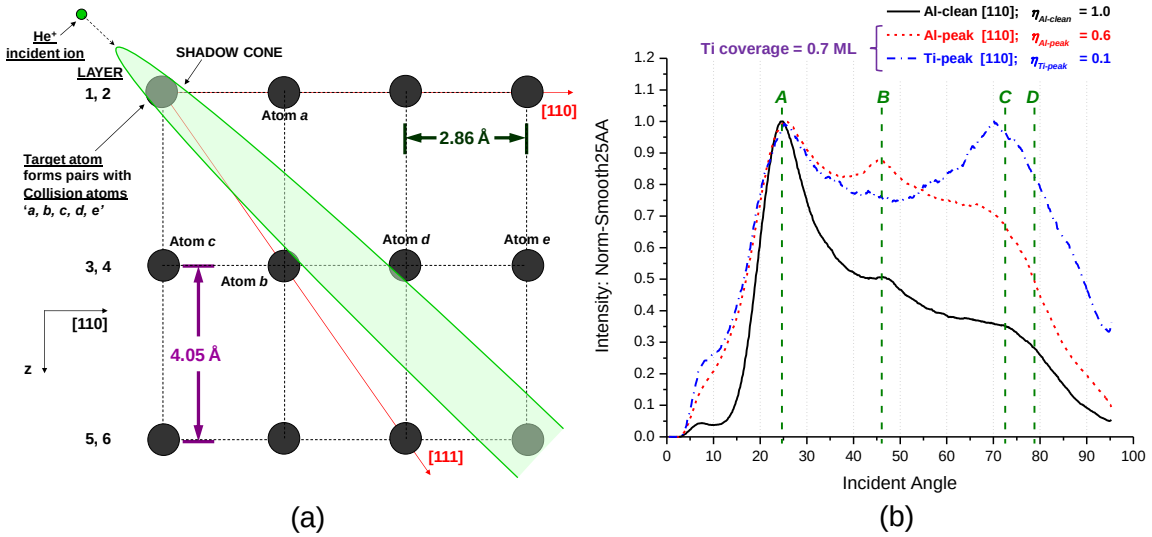

Figure 8.6: (a) The Al(110) crystal plane, perpendicular to surface plane. (b) LEIS polar-angle scan spectra in the [110] azimuth for the clean Al(001) surface and for 0.7 ML Ti on the Al(001) surface.

with the upper-left-most atom as target and origin of the shadow cone as depicted in Figure 8.6(a).

Table 8.2: [110] azimuth, contributing layer and collision atom for Al-clean scan reference-line peaks. Refer to peak labels in Figure 8.6(b).

Peak [110]	**Contributing Layer & (Atom)**
A	1, 2 (a); 3, 4 (d)
B	3, 4 (b, d)
C	3, 4 (b)
D	3, 4 (c)

Note that the Al-peak signal is of similar shape to the Al-clean signal. This allows us to infer that Al atoms post Ti-deposition occupy similar sites as in the clean substrate. The diminished intensity of the signal ($\eta_{Al-peak} = 0.6$) however does signify that fewer ion-to-Al-atom interactions have occurred. This we claim is due to a strong presence of Ti atoms in the 2nd layer of the substrate at every other lattice site as well as a lesser presence in the 1st layer. Thus, less Al atoms in the 1st

and 2nd layers, both of which form top rows of alternate (110) planes, contribute to the diminished strength of the peak at reference line A as compared to that in the Al-clean signal.

In the Ti-peak signal, in contrast to that in the [100] direction, we see a peak at the leading edge at reference line A which implies a 'top-row' presence of Ti atoms, which we believe primarily stems from the contribution of (110) planes whose top rows are located in the 2nd layer. Though there are no distinctive Ti peaks at line B, the presence of Ti atoms in the 3rd layer is suggested by the broad peak at C and D.

8.3.2.4 LEIS Polar-angle Scans (at higher Ti coverage): Figure 8.7 shows the polar-angle scans and corresponding scaling-ratio η values (see legend) for both the fixed [100] and [110] azimuths for a Ti coverage which we claim is higher than that in the previous discussion.

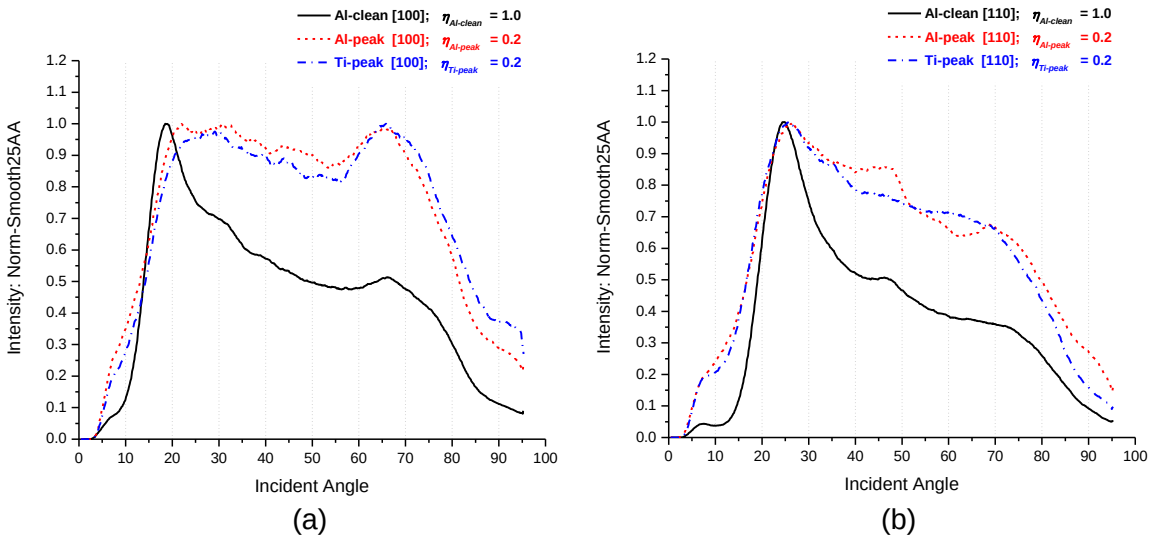

Figure 8.7: LEIS Polar-angle scan spectra for higher Ti coverage on the Al(001) surface. (a). [100] azimuth. (b). [110] azimuth.

The actual Ti coverage could not be determined through RBS for these two data sets due to equipment constraints. Since LEIS is sensitive primarily to the top two layers, we can gain insight to their structure by comparing the intensity of the un-normalized counts of the Ti-peak signals with that of the Al-peak signals. The scaling-ratio η values for the Al- and Ti-peak signals are comparable in each of the two respective azimuth directions tested. The scaling-ratio values shown in both Figure 8.5(b) and Figure 8.6(b) show a distinct contrast between $\eta_{Al-peak}$ and $\eta_{Ti-peak}$, the former being substantially greater than the latter. We believe this enables us to infer that the Ti coverage for the two sets of polar scans in Figure 8.7 is indeed higher than that in our previous sets with 0.7 ML Ti coverage. The results in Table 8.1 and Table 8.2, allow us to conclude that Al and Ti atoms are present in the top three layers. From the similarity in the Al- and Ti-peak signals respectively in each of the two sets of spectra shown in Figure 8.7(a) and 8(b), we can infer that the crystal structure for both Al and Ti atoms is of similar nature for this coverage of Ti. We propose a model for 1.5 ML Ti coverage as shown in Figure 8.8, placing Ti atoms at every other lattice site, in the top three layers. Given the lack of clarity in the c(2×2) LEED pattern however, such an ideally ordered structure is unlikely. The exact nature of the Ti occupancy in near surface layers cannot be determined from our data due to the inherent limitations of our LEIS setup which does not address ion neutralization effects which predominantly affect subsurface-layer contributions to collected spectra. We suggest that a Ti-Al alloy is not fully developed in the upper layers of the substrate, but incorporates in random patches or portions, enough to yield LEIS results which we have seen, as well as giving a blurry c(2×2) LEED pattern consistent with Ti occupancy at every other lattice site.

8.4 Conclusions

We have claimed from the analyses above, that Ti atoms displace Al atoms in the Al(001) crystal substrate. For 0.7 ML Ti coverage, we have argued that Ti atoms preferentially occupy sub-surface lattice sites, based on the analysis of LEIS polar-angle scan spectra and a surface energy argument for a preferred Al surface layer. The less than optimal yet undeniable c(2×2) LEED pattern supports the claim that Ti atoms incorporate into every other Al lattice site. As Ti deposition increases to a thickness greater than but close to 1 ML, the sustained c(2×2) LEED pattern continues to support this claim. LEIS polar-angle scan analysis results indicate that the top three layers are populated by Ti atoms, however due to the lack of quantitative information of ion-neutralization effects in sub-surface atomic layers the data do not evidence any particular layer preference for Ti occupancy.

We now address the theoretical models of Ti on the Al(001) surface as proposed by D. Spišák, et al. as shown in Figure 8.1. Each of these models proposed are for Ti coverage of 1 ML. The authors of this work found that Model 5 with Al-Ti/Al/AlTi/Al(001) in $L1_2$ stacking was the energetically preferred arrangement. From the results of our study we can directly dismiss theoretical Models 1 and 3 as inconsistent with our LEED image results since Ti atoms at every lattice site in a particular layer will not support a c(2×2) LEED pattern for 1 ML Ti coverage.

Models 2, 4 and 5, all having Ti atoms at every other lattice site regardless of which substrate layer they occupy, is consistent with our LEED results. However, Models 4 and 5 do not include Ti atoms in the 2^{nd} layer which is in disagreement with the strong evidence of 2^{nd} layer Ti occupancy as seen in our LEIS polar-angle scan results. Thus, we are left with Model 2 being in best agreement with our study when considering the top two layers of the substrate. Figure 8.8 shows our proposed

model for Ti on the Al(001) surface for Ti coverage of 1.5 ML. Since ideal ordering as depicted is unlikely, given the lack of clarity of the c(2×2) LEED pattern, we suggest the Ti-Al alloy is not fully developed in the upper layers but rather assembles in random portions of the substrate. The stacking arrangement from layer to layer is not determined by our measurements. Incorporating Ti atoms in the 3rd layer is our only addendum to the configuration proposed by D. Spišák in Model 2.

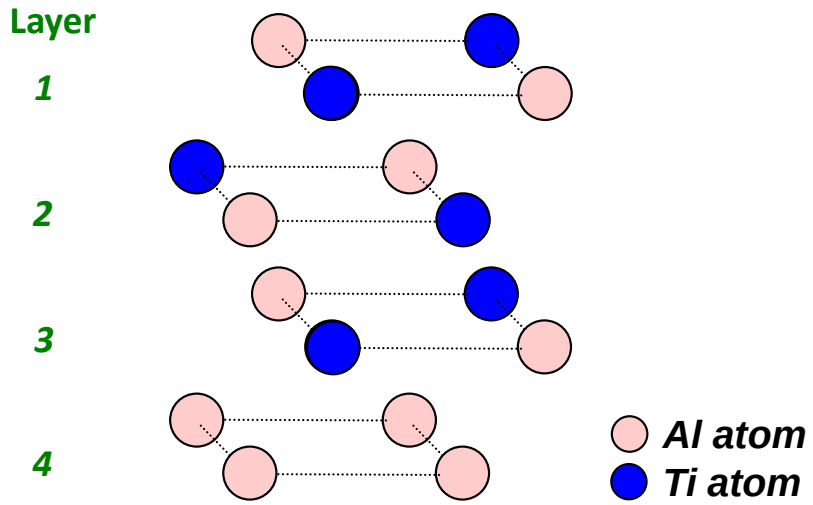

Figure 8.8: Proposed model for 1.5 ML Ti on the Al(001) surface.

8.5 LEIS Simulated Polar Scans for Ti on the Al(001) Crystal

Al-*fcc* crystal models with 11 atoms across the top and 3 rows into the bulk were created for two deposition thicknesses of Ti on Al(001) in each of the two major low-index azimuths, [100] and [110]. Simulated polar scans were generated using LEISsim for each of these models. We compare the computer simulated spectra with those collected experimentally.

To clarify terminology, Figure 8.9 labels the low index azimuth directions and planes in the Al(001) crystal with the coordinate system shown.

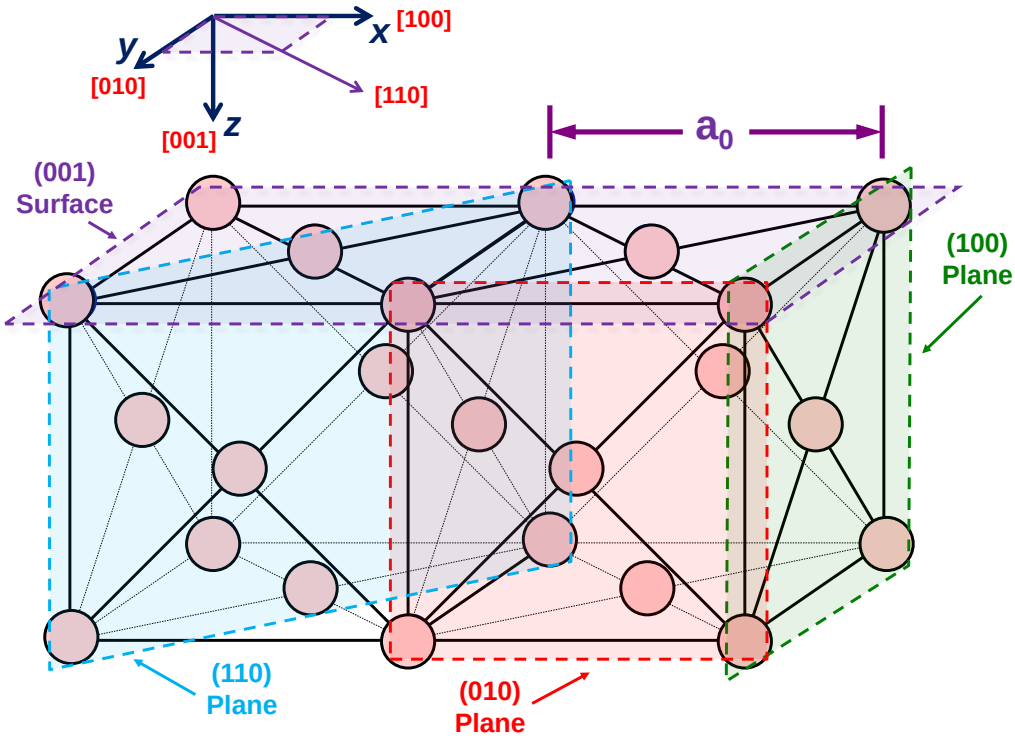

Figure 8.9: Low index azimuth directions and planes in the Al(001) crystal

The geometry of Ti atom placement in the Al crystal may require adding results of 2-D simulations generated from different target planes if Ti placement varies in adjacent planes lying along the same azimuth. This ensures that contributions from the proper proportion of Al and Ti atoms are accounted for. Alternate domain views of the crystal (e.g. as seen in the [100] azimuth direction compared to the [010] azimuth), may produce different 2-D target planes.

Only one of the two possible domains was chosen for a particular simulation. This approach saves time and effort. Though a complete simulation would include the use of the complete set of target planes and may offer a more accurate simulation, our objective is to identify peaks in the spectra only as an aid in interpreting the experimental data, and not to replicate the experimental spectra. Thus we deem this approach as justified.

Accounting for ion neutralization as a function of layer was implemented in the simulations. The neutralization parameters were identical as those used to generate the best Al-clean polar scans in both azimuths and are summarized in Table 8.3.

Table 8.3: Neutralization constants for each layer of the model target planes for both low index azimuths.

Azimuth	N_1	N_2	N_3
[100]	0.9	0.9	0.1
Azimuth	$N_{1,2}$	$N_{3,4}$	$N_{5,6}$
[110]	0.9	0.2	0.02

Simulated spectra were normalized by dividing the counts in each incident angle entry by the height of the highest peak, just as was done for their experimental counterparts. Corresponding η_i signal values are not defined for the simulations, but rather the ratio of the height of the highest peaks of the Ti- to Al-peak spectra is given so a comparison of the intensities of the un-normalized signals can be made.

8.5.1 Simulated 0.82 ML Ti on Al(001)

Simulated spectra in both low index azimuths were generated for a low Ti coverage of 0.82 ML for comparison with the experimental results with a Ti coverage of 0.8 ML as seen in the Ti-Al study.

In the analysis of LEIS experimental results, the claim was made that Ti prefers subsurface occupancy for submonolayer coverages. Here we test a proposed model for 0.82 ML Ti on Al(001). A portion of the 3-D model consisting of two unit cells of Al lattice constant a_0 is shown in Figure 8.10. The Ti atoms in the surface layer are dotted to represent a small contribution.

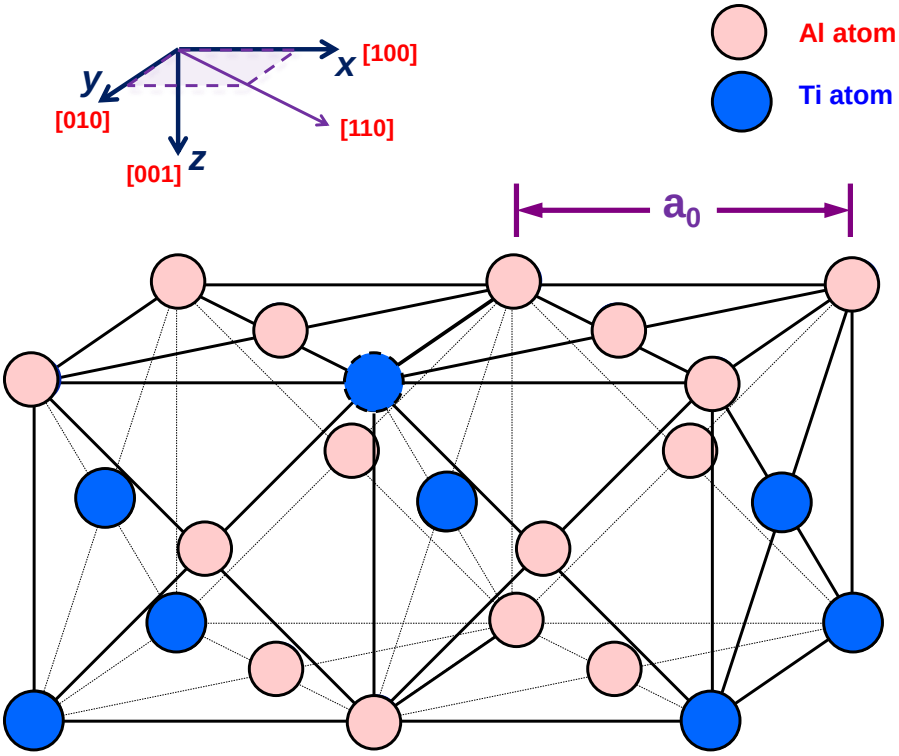

Figure 8.10: Portion of 3-D model for 0.82 ML Ti on the Al(001) surface.

8.5.1.1 Simulated Polar Scans in [100] Azimuth: Simulations of 0.82 ML Ti coverage LEIS polar scans in the [100] azimuth were generated. The target planes consist of atoms in 11, 10, 11 lattice sites in layers 1, 2, 3 respectively. Two targets were created for the (010) planes lying along the [100] azimuth direction. The geometry for Ti atom placement to be compatible with a $c(2 \times 2)$ LEED pattern, places Ti atoms in alternating Al lattice sites. This will be modeled in layer 2 for a Ti atom contribution of 0.5 ML. Layer 3 Ti occupancy of 0.27 ML and layer 1 of 0.05 ML make up the balance. Table 8.4 details the Ti atom placement.

Table 8.4: Ti atom placement for two target planes in the [100] azimuth for 0.82 ML Ti on Al(100).

Layer	# Sites	# Ti	Ti coverage
(010) Target Plane			
1	11	0	-
2	10	10	0.5 ML
3	11	0	-
Adjacent-(010) Target Plane			
1	11	1	0.05 ML
2	10	0	-
3	11	6	0.27 ML

Note the ratio of #Ti atoms to #Sites in the table must be halved to arrive at the proper value for Ti coverage. To clarify, in the first target, layer 2 has a #Ti to #Site ratio of 1, but the actual occupation of Ti in all of layer 2 is 0.5 ML. This is accounted for by the second target which has Al atoms and no Ti in layer 2.

The simulated results are shown in Figure 8.11(a) with the corresponding experimental set for 0.7 ML Ti shown in Figure 8.11(b).

In comparing the computer-generated polar scans to the experimental results, we see that the peak heights vary significantly in some cases especially for the Al-peak

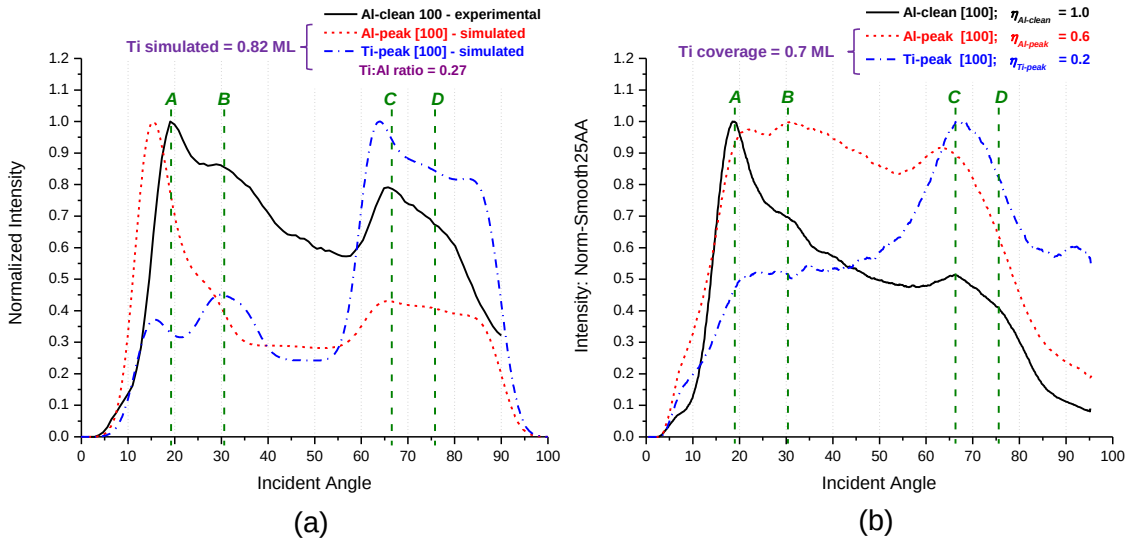

Figure 8.11: LEIS polar-angle scan spectra in the [100] azimuth for the clean Al(001) surface and for Ti on the Al(001) surface. (a) Simulated 0.82 ML Ti, (b) Experimental 0.7 ML Ti.

signal near reference lines *B*, *C* and *D*. However, the simulated scans do follow the shapes of the experimental spectra, which gives support to the model given above.

The Ti:Al signal ratio of 0.27 reveals that the simulated Ti-peak signal intensity is much less than that for the simulated Al-peak signal, just as the scaling factor $\eta_{Al-peak} = 0.6$ and $\eta_{Ti-peak} = 0.2$ in the experimental spectra show. It is encouraging also to see that the simulated Ti-peak signal leading peak at reference line *A* is missing as in its experimental counterpart.

The Al-clean signals shown in Figure 8.11 (a) and (b) are both experimental scans. The one used in the simulation plot was collected at a later date at a slightly different azimuth angle setting which we believe accounts for the more defined peak at reference lines *C* and *D*.

8.5.1.2 Simulated Polar Scans in [110] Azimuth: Simulations of 0.82 ML Ti coverage LEIS polar scans in the [110] azimuth were generated. The target planes

consist of atoms in 11, 11, 11 lattice sites in layers 1, 3, 5 respectively and adjacent plane layers 2, 4, 6 respectively. Recall that in this azimuth, top rows of adjacent (110) planes are in layers 1 and 2 respectively, giving the incident ion beam equal probability of first encounter strikes with 1^{st} or 2^{nd} layer atoms.

Two targets were created for the (110) planes lying along the [110] azimuth direction. One target plane in layer 2 accounts for a Ti atom contribution of 0.45 ML. In the other target, layer 3 Ti occupancy of 0.27 ML and layer 1 of 0.09 ML make up the balance. Table 8.5 details the Ti atom placement.

Table 8.5: Ti atom placement for two target planes in the [110] azimuth for 0.82 ML Ti on Al(100).

Layer	# Sites	# Ti	Ti coverage
(110) Target Plane			
1	11	1	0.09 ML
3	11	3	0.27 ML
5	11	0	-
Adjacent-(110) Target Plane			
2	11	5	0.45 ML
4	11	0	-
6	11	0	- ML

Note that in this azimuth the ratio of #Ti atoms to #Sites in the table is fully counted to arrive at the proper value for Ti coverage in contrast to the [100] azimuth case.

The simulated results are shown in Figure 8.12(a) with the corresponding experimental set for 0.7 ML Ti shown in Figure 8.12(b).

Comparing the simulated spectra with the experimental, once again we focus on spectrum overall shape rather than peak heights. Note that the Al-peak and Ti-peak signals in the simulated scan are similar in shape. The simulated Ti-peak signal leading peak at reference line A is present, matching the similar result in the

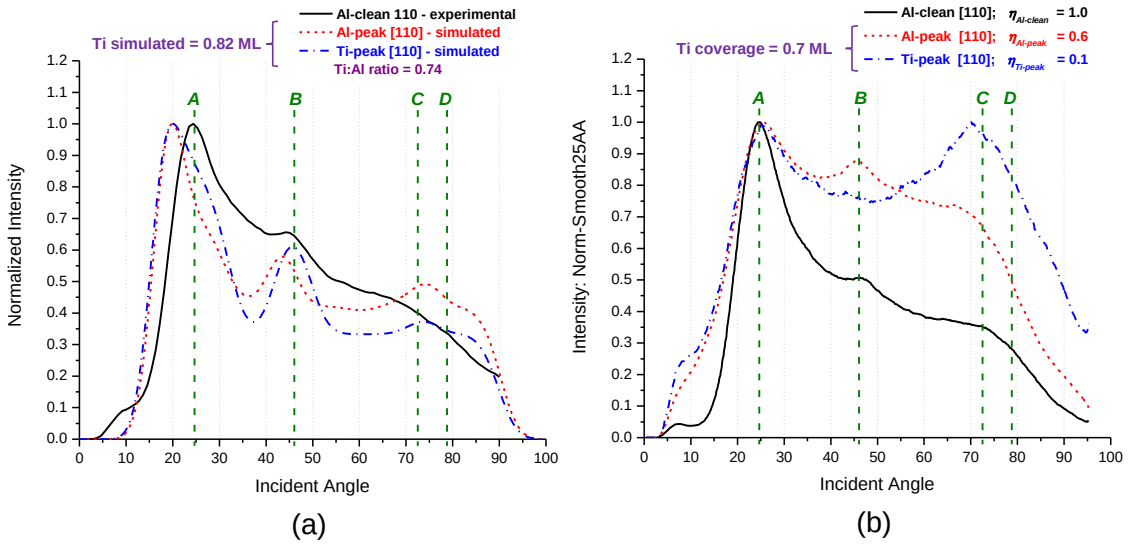

Figure 8.12: LEIS polar-angle scan spectra in the [110] azimuth for the clean Al(001) surface and for Ti on the Al(001) surface. (a) Simulated 0.82 ML Ti, (b) Experimental 0.7 ML Ti.

experimental scan. The Ti:Al signal ratio of 0.74 shows that the simulated Ti-peak signal intensity is less than that for the simulated Al-peak signal, but less pronounced in this azimuth as compared to the [100] direction which does not follow the trend that the scaling factor $\eta_{Al-peak}$ and $\eta_{Ti-peak}$ give in the experimental spectra with values of 0.6 and 0.1 respectively. Nonetheless, the placement of peaks in the simulated scans are similar to that in the experimental spectra, which gives credible support to the model proposed.

As in the previous azimuth, the Al-clean signals shown in Fig 8.12(a) and (b) are both experimental scans. Here the two Al-clean signals are very similar in shape.

8.5.2 Simulated 1.5 ML Ti on Al(001)

Simulated spectra in both low index azimuths were generated for a higher Ti coverage of 1.5 ML to test the model proposed in the results section of the Ti-Al study. Recall that for the experimental LEIS polar scans, RBS capability was not

available at the time of the data collection, and arguments were made that the Ti coverage was greater than but near 1 ML for the collected spectra. We use these experimental results for comparison to the simulated spectra. A portion of the 3-D model consisting of two unit cells of Al lattice constant a_0 is shown in Figure 8.13.

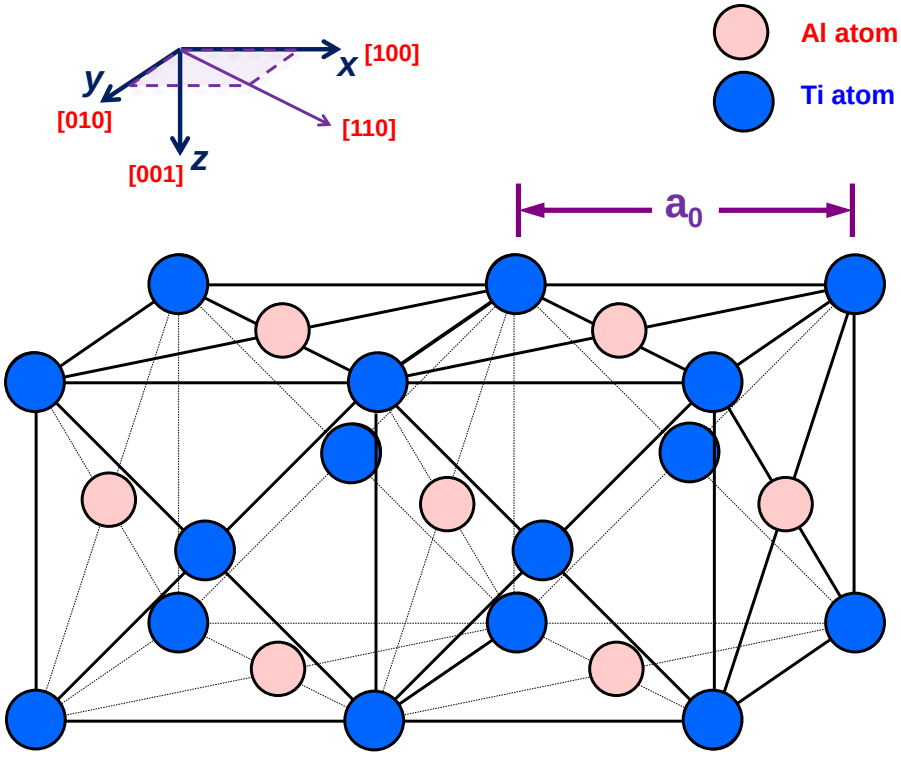

Figure 8.13: Portion of 3-D model for 1.5 ML Ti on the Al(001) surface.

8.5.2.1 Simulated Polar Scans in [100] Azimuth: Simulations of 1.5 ML Ti coverage LEIS polar scans in the [100] azimuth were generated. The target planes consist of atoms in 11, 10, 11 lattice sites in layers 1, 2, 3 respectively. Of the two domains possible, we chose the one lying along the [010] azimuth direction to create two targets found in the (100) planes (see Figure 8.9). The alternate domain would have two targets found in the (010) planes consisting strictly of either Al or Ti atoms

for adjacent planes, which is unrealistic. The geometry for Ti atom placement in the top three layers is fully compatible with a $c(2 \times 2)$ LEED pattern, placing Ti atoms in alternating Al lattice sites. This is modeled in layer 1, 2 and 3 with a Ti atom contribution of 0.5 ML per layer. Table 8.6 details the Ti atom placement.

Table 8.6: Ti atom placement for two target planes in the [010] azimuth for 1.5 ML Ti on Al(100).

Layer	# Sites	# Ti	Ti coverage
(100) Target Plane			
1	11	11	0.5 ML
2	10	0	-
3	11	11	0.5 ML
Adjacent-(100) Target Plane			
1	11	0	-
2	10	10	0.5 ML
3	11	0	-

The ratio of #Ti atoms to #Sites in the table must be halved to arrive at the proper value for Ti coverage.

The simulated results are shown in Figure 8.14(a) with the corresponding experimental set for higher coverage Ti shown in Figure 8.14(b).

As in the experimental scans the Al- and Ti-peak signals are similar in shape. The Ti:Al signal ratio of 1.25 says that the intensity of the simulated Ti-peak signal is somewhat higher than the simulated Al-peak signal. The scaling factor $\eta_{Al-peak}$ and $\eta_{Ti-peak}$ for the experimental spectra both at 0.2 show that the intensities of the Al- and Ti-peak signals are comparable. Apart from this difference, the simulated signals do have a similar shape as do their experimental counterparts, which does support the model proposed.

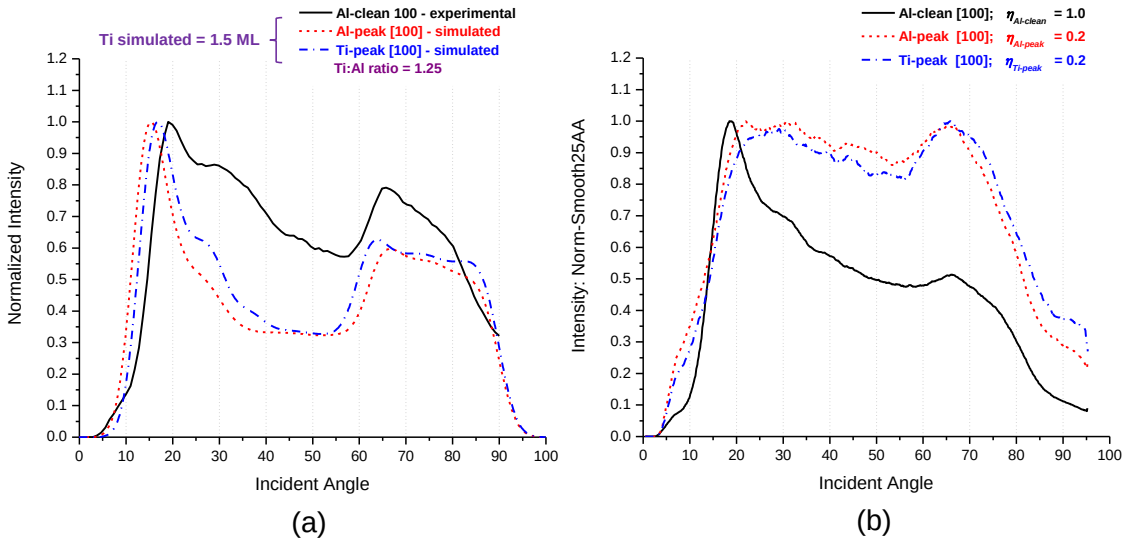

Figure 8.14: LEIS polar-angle scan spectra in the [100] azimuth for the clean Al(001) surface and for Ti on the Al(001) surface. (a) Simulated 1.5 ML Ti, (b) Experimental higher coverage Ti.

8.5.2.2 Simulated Polar Scans in [110] Azimuth: Simulations of 1.5 ML Ti coverage LEIS polar scans in the [110] azimuth were generated. As before, the target planes consist of atoms in 11, 11, 11 lattice sites in layers 1, 3, 5 respectively and adjacent plane layers 2, 4, 6 respectively.

Two targets were created for the (110) planes lying along the [110] azimuth direction. The first target plane gives a Ti atom contribution of 0.45 ML each in layers 1 and 3. The second target plane has 0.55 ML to complete the balance to 1.5 ML Ti total. Table 8.7 details the Ti atom placement.

In this azimuth the ratio of #Ti atoms to #Sites in the table is fully counted to arrive at the proper value for Ti coverage.

The simulated results are shown in Figure 8.15(a) with the corresponding experimental set for higher coverage Ti shown in Figure 8.15(b).

As in the previous azimuth at this higher coverage, the simulated Al- and Ti-peak signals are similar in shape, as are their experimental counterparts. The Ti:Al signal

Table 8.7: Ti atom placement for two target planes in the [110] azimuth for 1.5 ML Ti on Al(100).

Layer	# Sites	# Ti	Ti coverage
(110) Target Plane			
1	11	5	0.45 ML
3	11	5	0.45 ML
5	11	0	-
Adjacent-(110) Target Plane			
2	11	6	0.55 ML
4	11	0	-
6	11	0	-

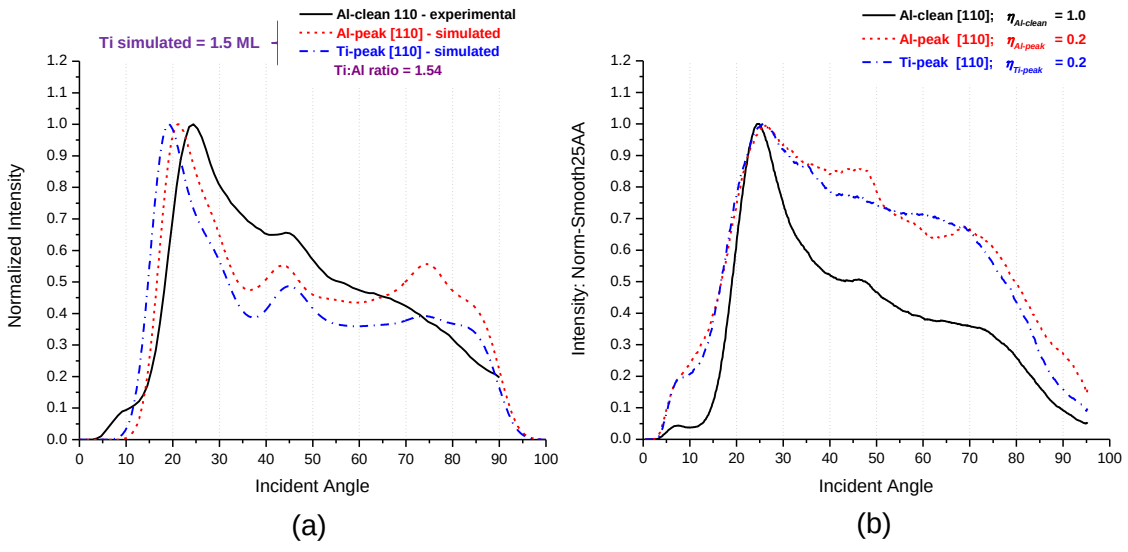

Figure 8.15: LEIS polar-angle scan spectra in the [110] azimuth for the clean Al(001) surface and for Ti on the Al(001) surface. (a) Simulated 1.5 ML Ti, (b) Experimental higher coverage Ti.

ratio of 1.54 as in the latter simulation says that the intensity of the simulated Ti-peak signal is higher than the simulated Al-peak signal. The scaling factor $\eta_{Al-peak}$ and $\eta_{Ti-peak}$ for the experimental spectra are again both equal to 0.2, showing that the Al- and Ti-peak signal experimental intensities are comparable. As in the latter azimuth, excepting this difference, the simulated signals have a similar shape as do their experimental counterparts, which does support the model proposed.

We note here that the model for 1.5 ML Ti in Figure 8.13 places Ti atoms in the 3$^{\text{rd}}$ layer in a line directly beneath the 1$^{\text{st}}$ layer, that is the stacking is ABA. If we shift the 3$^{\text{rd}}$ layer one lattice site in the [110] direction, this creates a different crystal structure with stacking ABC, which requires different simulation target planes. In any case, this was not pursued as analysis of our LEIS experimental results for the higher coverage Ti did not determine the stacking arrangement from layer to layer.

CHAPTER 9
V ON THE AL(001) SURFACE

9.1 Introduction

The surface structure of V on Al(001) is not well understood and to date only one reference was found in the literature which featured a similar structure of V on Ni(001) [38]. Whereas the structure at room temperature of Al is *fcc*, the native structure V is *bcc*.

The motivation to study V on Al(001) originated from work with the *BFS* (Bozzolo-Ferrante-Smith) *Method for Alloys* as explained in Section 6.1. Recall that the BFS Method predicts that Ti and V should both act as effective interlayer diffusion barriers between Al and Fe [1].

The electronic configurations of V and Ti vary only in the $3d$ subshell and have the same $4s^2$ outer most shell configuration. This suggests that their chemical properties should be similar. However they possess distinct properties, differing in atomic size, strength of bonds in forming alloys and values of surface energies in their pure crystal form. Our examination of V uses LEED and LEIS to study the structure of V in the the surface layers of Al(001). The results for V presented here will be contrasted to the results of the Ti-Al system covered in Chapter 8.

9.2 Experiment

Experiments were done in an ultra-high vacuum (UHV) chamber with the same equipment setup as was used for the study of Ti on Al(001).

Unlike Ti deposition which used a resistively heated wire filament, for V deposition we used an UHV e-beam evaporator system containing a V rod 1.5 mm diameter,

99.8% (metals basis) from *Alpha Aeser*. As for the Ti study, the chamber has a connection through a differentially pumped beam line to a 2 MV van de Graaff accelerator, giving RBS capability for determining deposited thin-film coverage of V on the sample surface.

Prior to V deposition, the sample surface was prepared in the same manner using Ar^+ sputtering and sample annealing as was done for the Ti-Al system. V deposition was carried out nominally at room temperature using an e-beam evaporator arrangement at chamber pressures in the range of approximately 6–7 $\times$ 10^{-10} Torr and flux-monitor current of approximately 5–6 nA.

LEIS was configured as described in Section 4.2 and was conducted using a He^+ incident ion beam at nominal energies of 1.2 keV and chamber He^+ pressure of approximately 2–3 $\times$ 10^{-7} Torr. Ion currents were kept relatively low (8–15 nA) in order to minimize the damage to the sample surface which occurs from sputtering by the incident He^+ ion beam.

As for the Ti study, three types of LEIS spectra were collected: energy, azimuth-angle and polar-angle scans.

LEIS energy scans were collected at a fixed polar angle of 45° and a fixed azimuth angle of 52°.

Azimuth-angle scans were collected at a fixed polar angle of 12° with respect to the sample surface plane. The goniometer azimuth angle setting was incremented manually in steps of approximately 1.2° every 30 sec. The azimuth angle was swept through a range of approximately 135° at a rate of about 2.3°/min.

Sets of polar-angle scans were collected in the [100] and [110] azimuth directions. The goniometer polar angle setting was incremented manually in steps of approximately 0.9° every 30 sec. The polar angle was swept through a range of approximately 0° to 90° at a rate of about 1.8°/min.

The plotted data sets found in this discussion are smoothed versions of the original data. A 5-point Adjacent-Averaging smoothing method provided in the *Origin* graphing software package (v.8.0, *OriginLab Corporation)* was used. Plotted azimuth- and polar-angle scans have been normalized by dividing by the respective maximum count collected for each spectrum. As for the Ti study, we define a scaling factor η for comparing signal strengths of un-normalized smoothed spectra as expressed in Equation 8.1.

LEIS azimuth- and polar-angle scan spectra collected at the fixed energy corresponding to the element Al will be referred to as the *Al-peak* signal, and that for V as the *V-peak* signal. For the condition of a clean Al(001) surface, the spectra collected will be referred to as the *Al-clean* signal.

RBS analysis was performed to find the coverage of V on the Al(001) surface in a similar manner under the same experimental parameters as in the Ti study. In the discussion to follow, two sets of LEIS azimuth-angle scans and three sets of polar-angle scans are used. The RBS thickness for sub-monolayer data set (azimuth and polar scans) gave a V coverage of 0.6 ML. For the second data set (azimuth and polar scans), RBS results gave a V coverage of 2.5 ML. For the third set (polar scans only) the coverage of V was 2.3 ML. For each data set, the LEED pattern was observed and photographed after V deposition.

Throughout this discussion we will contrast experimental results from the Ti on Al(001) study with those for V on Al(001).

9.3 LEED Results

Figure 9.1(a) and (b) shows a clean Al(001) surface and ∼0.6 ML V deposited on Al(001), respectively.

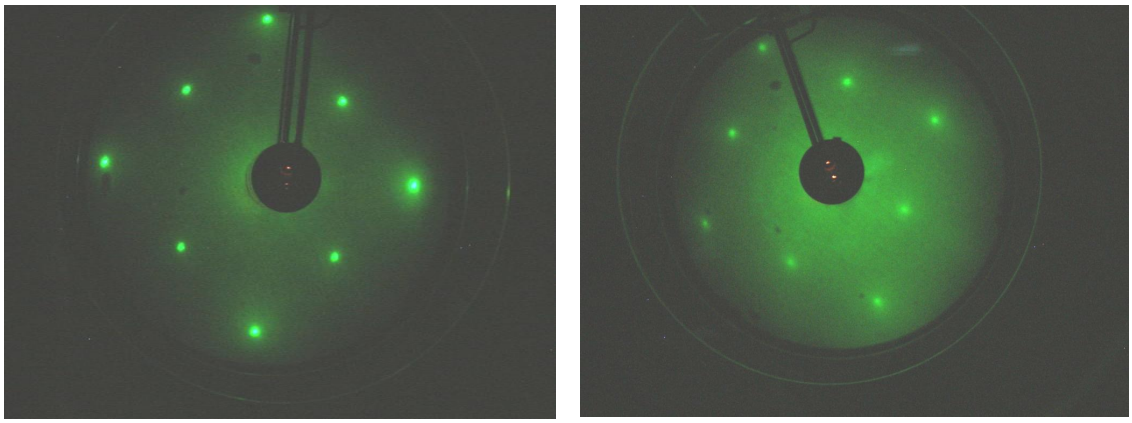

Figure 9.1: Two LEED images, (a) clean Al(001) $p(1 \times 1)$ pattern at 83.0 eV LEED-electron energy, (b) ∼0.6 ML V on Al(001) $p(1 \times 1)$ pattern at 93.7 eV LEED-electron energy.

Note the LEED image post V deposition shows no evidence of anything out of the ordinary developing but shows the typical $p(1 \times 1)$ pattern of the clean Al surface. We found at similar coverage (though not shown here), that Ti begins to evidence a faint $c(2 \times 2)$ pattern.

Figure 9.2(a) and (b) shows the LEED images for ∼2.5 ML V on Al(001), each at a slightly different LEED-electron energy.

Note that both LEED images show no evidence of any different pattern developing but rather have become very blurry with higher background illumination, evidencing that surface structure order has been disrupted. The light-colored circles were superimposed on the photos to aid in locating the $p(1 \times 1)$ spot locations which are present in the photos but very dim and indistinct given the highly illuminated background.

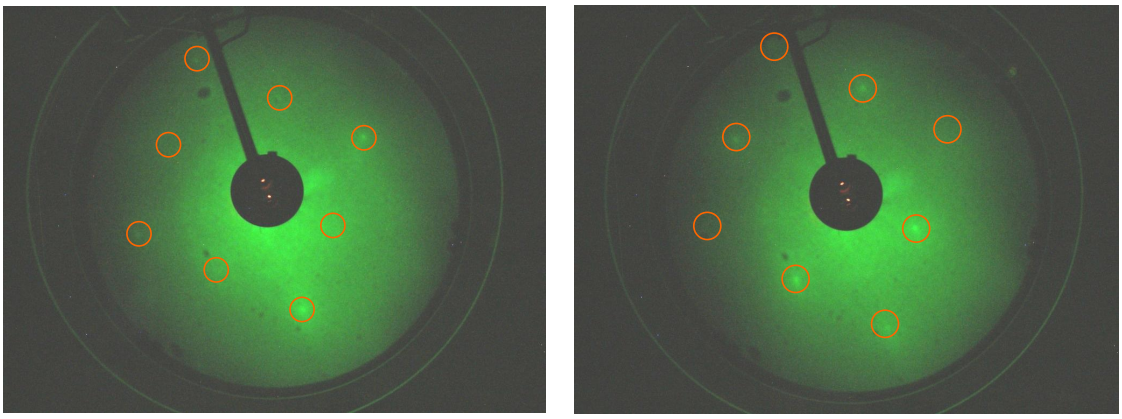

Figure 9.2: Two LEED images, (a) ∼2.5 ML V on Al(001) $p(1 \times 1)$ pattern at 90.0 eV LEED-electron energy, (b) ∼2.5 ML V on Al(001) $p(1 \times 1)$ pattern at 95.1 eV LEED-electron energy.

9.4 LEIS Results

In this section we will present the results for LEIS energy, azimuth and polar scans for submonolayer and higher coverage V on Al(001). All the data collected for the same V coverage was done in the same experimental session. Results will be contrasted with the Ti-Al system covered earlier.

9.4.1 LEIS Energy Scans

The deposited V thickness for the following two sets of energy scans was determined by RBS to be 0.6 ML and 2.5 ML respectively.

9.4.1.1 LEIS Energy Scans for 0.6 ML V:

Two LEIS energy scans are shown in Figure 9.3.

For these scans an incident beam of He^+ ions at a nominal energy of 1.2 keV was directed to our sample surface at a 45° polar angle and 52° azimuth angle. The

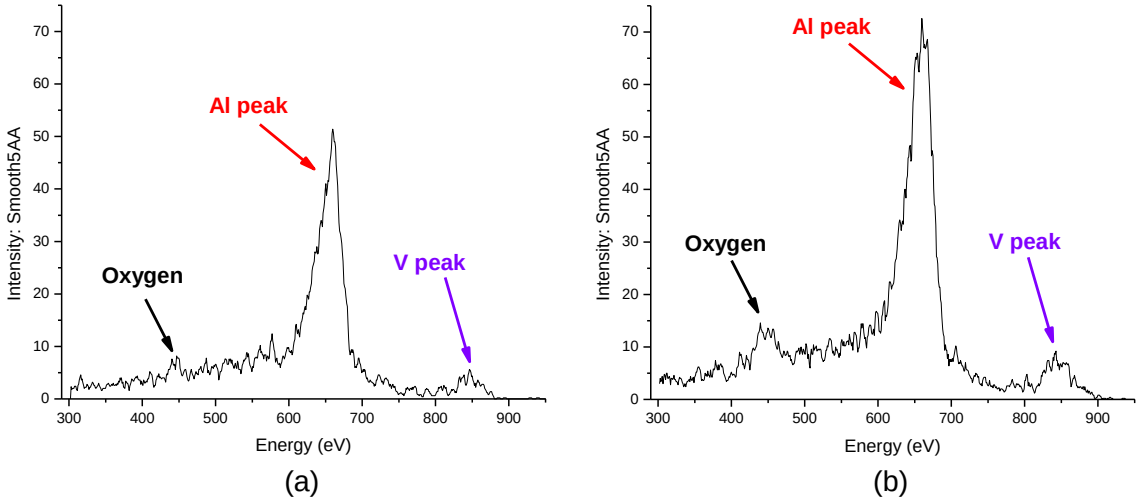

Figure 9.3: LEIS energy scan spectra post 0.6 ML V deposition on the Al(001) crystal surface, incident He^+ beam oriented at a 45° polar angle and 52° azimuth angle (a) before collection of set of LEIS-angular scans, sample current at $\sim$ 13.7 nA, (b) after collection of set of LEIS-angular scans, sample current at $\sim$ 14.1 nA.

analyzer acceptance energy was swept from 300 eV to approximately 900 eV. Note the rise in the oxygen peak in the scan taken after the set of LEIS angular scans (polar and azimuth scans) were completed. The time between collection of this pair of scans was about 6 hours, so a rise in the oxygen peak is expected due to the continual adsorption of the sample surface by residual amounts of O_2 in the chamber. The V and Al peaks also have increased but it is unclear as to the cause. There is a slightly greater incident ion beam sample current used in the energy scan, collected after all the angular scans were completed, which could have contributed to this increase. However, we could speculate that the sputtering of the surface by the incident ion beam throughout the experimental session, may have revealed more V atoms in the layers below.

9.4.1.2 LEIS Energy Scans for 2.5 ML V: Two LEIS energy scans for a V coverage of 2.5 ML are shown in Figure 9.4.

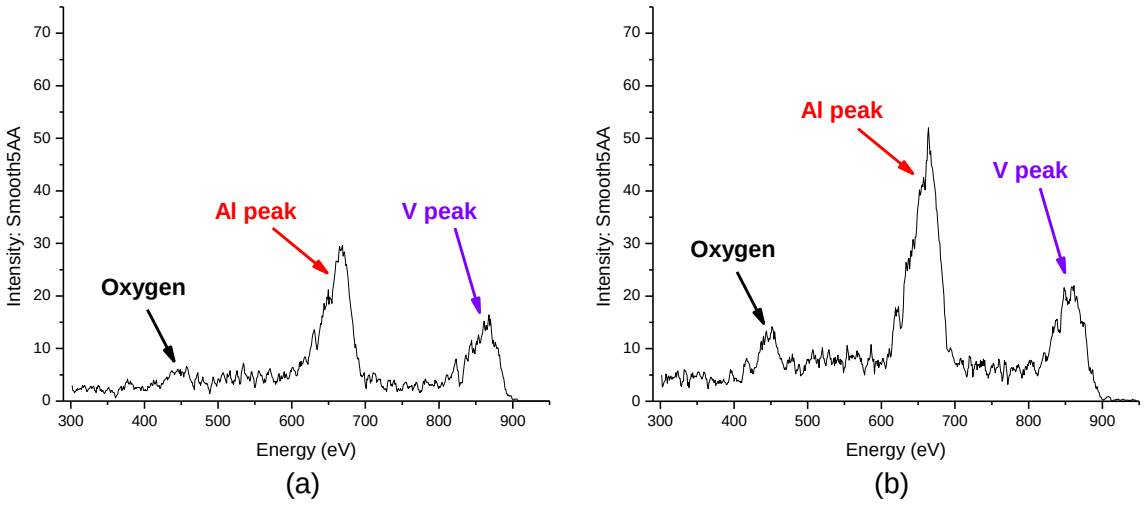

Figure 9.4: LEIS energy scan spectra post 2.5 ML V deposition on the Al(001) crystal surface, incident He^+ beam oriented at a 45° polar angle and 52° azimuth angle (a) before collection of set of LEIS-angular scans, sample current at $\sim$ 13 nA, (b) after collection of set of LEIS-angular scans, sample current at $\sim$ 14.2 nA.

As for the lower coverage set, the scan taken after the set of LEIS polar and azimuth scans were completed, the oxygen peak has increased which is expected, and also the V and Al peaks have increased in intensity as in the low coverage set.

9.4.2 LEIS Azimuth Scans

The deposited V thickness for the following two sets of azimuth scans was determined by RBS to be 0.6 ML and 2.5 ML which we will call the low coverage and high coverage sets, respectively. Figure 9.5(a) and (b) illustrates these two sets. The He^+ incident ion beam directed to our sample surface had a nominal energy of 1.2 keV. The polar angle was fixed at 12° from glancing with respect to the sample surface.

Three curves shown are the Al-clean signal, the Al-peak signal and the V-peak signal. The scale factor η values for each spectrum are shown (see legend), giving a comparison of the strengths of the Al- and V-peak signals to the Al-clean signal. Valleys at particular azimuth directions are labeled. Note the clear four-fold symmetry

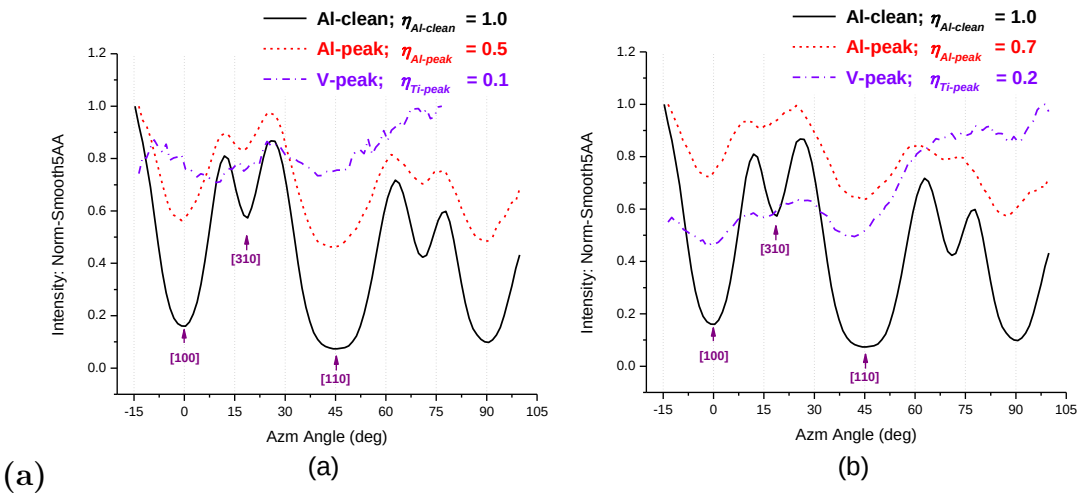

Figure 9.5: Azimuth-angle scan spectra for the Al(001) surface collected at a 12° polar angle, showing the Al-clean scan, and the Al-peak and V-peak scans for, (a) ∼0.6 ML V coverage, and (b) ∼2.5 ML V coverage.

of the Al-clean signal whose signal shape repeats every 90°. In (a) this same four-fold symmetry can be seen clearly in the Al-peak signal and very weakly in the V-peak signal particularly given its signal strength in comparison to the Al-clean signal as the scale factor η_{V-peak} value illustrates. The cause of an additional asymmetry in the intensity of the V-peak signal that occurs at the right side of the spectrum is unknown, though we speculate might be due to drift in experimental parameters. In (b) the same four-fold symmetry found in the Al-clean signal again can be clearly seen in the Al-peak signal and more now in the V-peak signal than in the low coverage case. The curious asymmetry in the intensity of the V-peak signal still occurs at the right side of the spectrum as seen in the low coverage case.

For both the low and high coverage sets, the matching symmetry of the Al-peak signal to the Al-clean signal allows us to conclude that the *fcc*-cubic lattice structure of clean Al surface is not disrupted due to the addition of V atoms. For the low coverage set, the hint of four-fold symmetry of the V-peak signal allows us to infer that V atoms begin to arrange themselves into a cubic structure. Since we have

collected these spectra at a glancing value of 12° for the polar angle, the intensity of each signal is primarily due to backscattered ions coming from the surface layer of the substrate which leads us to the conclusion that at 0.6 ML V coverage, we have very few V atoms present in the 1st layer of the substrate. For the high coverage set the more developed four-fold symmetry of the V-peak signal suggests that V atoms continue to arrange themselves into a cubic structure commensurate with Al-lattice sites. A valley at 16° azimuth angle is even evident in both the Al- and V-peak signals at this higher V coverage. As the contribution to the intensity of each signal in azimuth scans comes primarily from backscattered ions from the surface layer, we conclude that at 2.5 ML V coverage with $\eta_{V-peak} = 0.2$, we have more V atoms present in the 1st layer of the substrate compared to that for the low coverage case where $\eta_{V-peak} = 0.1$. However, $\eta_{Al-peak} = 0.5$ for the low coverage set and $\eta_{Al-peak} = 0.7$ for the high coverage set also shows the same trend, so the argument is not a strong one. Table 9.1 summarizes this.

Table 9.1: Azimuth scan η_{signal} value comparisons for V deposition thickness of 0.6 ML vs. 2.5 ML.

Azimuth scan V on Al(001)		
η_{signal}	**0.6 ML V**	**2.5 ML V**
Al-clean	1.0	1.0
Al-peak	0.5	0.7
V-peak	0.1	0.2

The azimuth scans therefore weakly support the argument for more V atoms in the surface layer for higher V deposition thickness. We will try to gain insight into this matter from the results of the polar-angle scans. Before we leave the analysis for azimuth scans, let us compare the corresponding system of Ti on Al(001) treated earlier, with these results for the V-Al system.

The scale-factor η_{signal} values for 0.8 ML Ti on Al(001) covered in Section 8.3.2.2 are listed in Table 9.2.

Table 9.2: Azimuth scan η_{signal} values for 0.8 ML Ti on Al(001).

Azimuth scan Ti on Al(001)		
η_{signal}	**0.8 ML Ti**	**≥1 ML Ti**
Al-clean	1.0	n/a
Al-peak	0.6	n/a
Ti-peak	0.4	n/a

Azimuth scans for 0.8 ML Ti on Al(001) were the only set treated in the Ti-Al system analysis. Table 9.2 gives the scale-factors of $\eta_{Al-peak} = 0.6$ and $\eta_{Ti-peak} = 0.4$ for this coverage of Ti. These scale-factor values contrast each other less than either of the corresponding low or high V coverage η_{signal} values. This suggests that Ti atoms populate the surface layer of the Al(001) substrate slightly more than V atoms do.

9.4.3 LEIS Polar Scans

The deposited V thickness for the following two sets of polar scans was determined by RBS to be 0.6 ML and 2.5 ML which as for the azimuth scans, we will call the low coverage and high coverage sets, respectively.

9.4.3.1 LEIS Polar-angle Scans for 0.6 ML V: Figure 9.6 shows the resulting spectra from LEIS polar-angle scans taken in the fixed [100] and [110] azimuths for 0.6 ML V coverage.

The Al-clean signals, plotted on the same axes, will be our baseline references with which to analyze the post V-deposition Al- and V-peak signals. Shown are the smoothed and normalized spectra data as well as the scale factor η values (see legend) for each spectrum. Note the four dotted reference lines *A*–*D* located at the

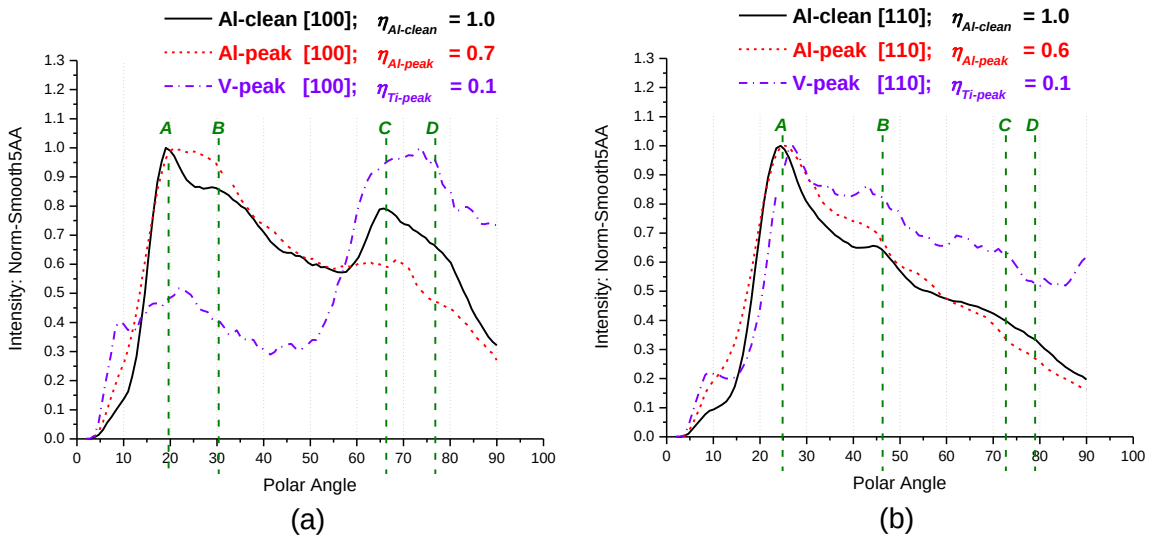

Figure 9.6: LEIS polar-angle scans for 0.6 ML V coverage plotted with the Al-clean scan for (a) the [100] azimuth, and (b) the [110] azimuth.

approximate position of major peaks or prominences in the Al-clean signal spectrum. Geometrical shadow cone analysis was used to analyze the Al-clean signal peaks for both azimuths as was covered in Section 4.4.3.

The lack of a strong peak in the V-peak polar scan in the [100] direction at reference line A, as compared to that for the Al-clean and Al-peak signals, suggests relatively fewer V atoms present in the 1st layer of the crystal substrate, while the prominence at line C indicates a relatively greater presence of V atoms in the 2nd layer. Given the V coverage value of 0.6 ML for this set of polar scans, the much lesser strength of the V-peak signal compared to the Al-peak signal ($\eta_{V-peak} = 0.1$ and $\eta_{Al-peak} = 0.7$), along with the assertion that neutralization of backscattered ions becomes progressively greater as below-surface layers are traversed, suggests that V atoms prefer sub-surface occupancy. The initial rise in the V-peak signal at A does suggest however that some 1st layer V atoms are indeed present, and the intensity level at D suggests the presence of V atoms in the 3rd layer as well.

In the [110] azimuth a new set of reference lines A–D mark the positions of peaks and prominences in the Al-clean signal for comparison to the Al- and V-peak signals. Note that the Al-peak signal is of similar shape to the Al-clean signal. This allows us to infer that Al atoms post V-deposition occupy similar sites as in the clean substrate. The diminished intensity of the signal ($\eta_{Al-peak} = 0.6$) however does signify that fewer ion-to-Al-atom interactions have occurred. This we claim is due to a strong presence of V atoms in the 2$^{\text{nd}}$ layer of the substrate as well as a lesser presence in the 1$^{\text{st}}$ layer as concluded by the results of the polar scans in the [100] azimuth. We also cannot distinguish here whether the 2$^{\text{nd}}$ or 1$^{\text{st}}$ layer has the greater presence of V atoms, due to the equal probability for ion-target atom interactions in either layer since top row atoms in alternate (110) planes are comprised of 1$^{\text{st}}$ and 2$^{\text{nd}}$ layer atoms respectively. Thus, less Al atoms in either the 1$^{\text{st}}$ or 2$^{\text{nd}}$ layers cause the strength of the Al-peak at reference line A to diminish as compared to that for the Al-clean signal.

In the V-peak signal, in contrast to that in the [100] direction, we see a peak at the leading edge at reference line A which implies a 'top-row' presence of V atoms, which we believe primarily stems from the contribution of (110) planes whose top rows are located in the 2$^{\text{nd}}$ layer. Small peaks in this scan also appear at reference lines B, C and D which suggest a 3$^{\text{rd}}$ layer presence of V atoms. The similar shape of the V-peak signal to the Al-clean signal also implies that the structure of V atoms is similar to that of the clean Al crystal in the surface layers.

9.4.3.2 LEIS Polar-angle Scans for 2.5 ML V: Figure 9.7 shows the polar-angle scans in the [100] and [110] azimuths and corresponding scaling-ratio η values (see legend) for 2.5 ML V coverage.

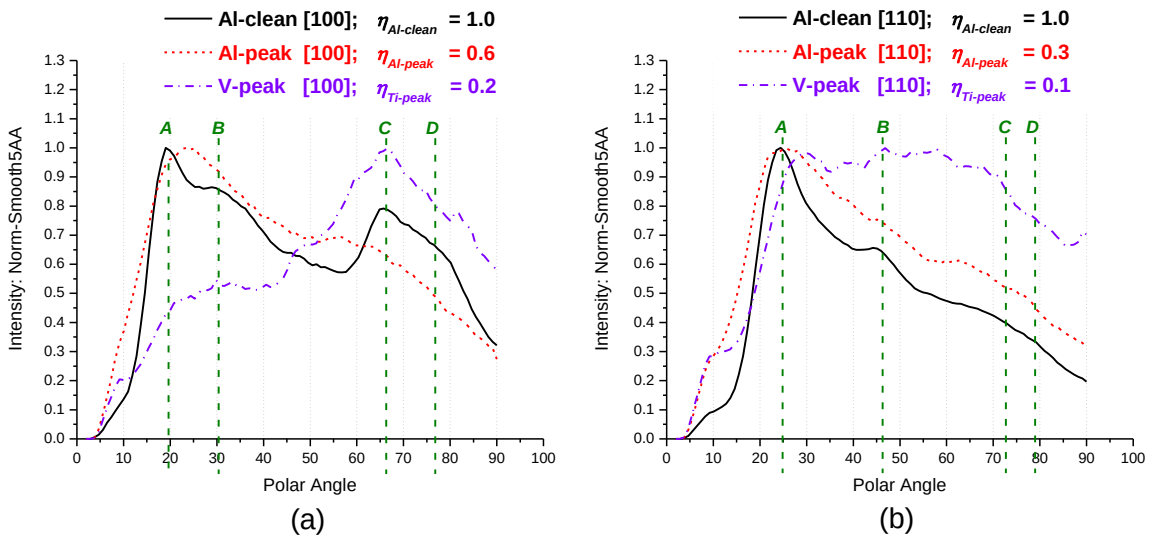

Figure 9.7: LEIS polar-angle scans for 2.5 ML V coverage plotted with the Al-clean scan for (a) the [100] azimuth, and (b) the [110] azimuth.

In Figure 9.7 the general shapes of the Al- and V-peak signals in the [100] azimuth are not unlike those of their counterparts in Figure 9.6. The Al-peak signal still mirrors the general shape of the Al-clean signal. The V-peak signal also still has a pronounced greater prominence at reference line C compared to that at reference line A. This suggests that even at this higher coverage, V tends to prefer sub-surface occupancy. As an aid in the comparison between these two sets of polar scans, let us again try to gain insight into the structure by comparing the intensity of the un-normalized counts of the V-peak signals with that of the Al-peak signals. The scaling-ratio η values for the Al- and V-peak signals for both coverages are listed in Table 9.3.

Note that the Al- and V-peak signal scaling ratio values are not comparable to each other at either V coverage, which supports the premise that V prefers sub-surface occupancy even at the higher V deposition thickness. There is though a slight contrast between the Al- and V-peak scaling-ratio difference at 2.5 ML ($\eta_{Al-peak} = 0.6$ and

Table 9.3: Polar scan ([100] azimuth) η_{signal} value comparisons for V deposition thickness of 0.6 ML vs. 2.5 ML.

Polar scan ([100] azimuth) V on Al(001)		
η_{signal}	**0.6 ML V**	**2.5 ML V**
Al-clean	1.0	1.0
Al-peak	0.7	0.6
V-peak	0.1	0.2

$\eta_{V-peak} = 0.2$) which is not as great as in the 0.6 ML case ($\eta_{Al-peak} = 0.7$ and $\eta_{V-peak} = 0.1$). This suggests that V occupancy is increasing in the layers visible to LEIS (top 2–3 layers) as the V deposition increased from low to high coverage.

Finally let us compare this analysis with that from the the Ti-Al system. For Ti on Al(001), the contrast in Al- and Ti-peak signal shapes between the sub-monolayer and higher Ti coverage polar angle scans in the [100] azimuth, were markedly different. In the sub-monolayer Ti case, the Al- and Ti-peak signal shapes match the corresponding signals for the sub-monolayer V set. However, for the greater Ti coverage case, the Al- and Ti-peak signals were comparable in both shape (see Figure 8.7 in Ti-Al system treatment) and scaling-ratio η_{signal} values, as can be seen in Table 9.4 below.

Table 9.4: Polar scan ([100] azimuth) η_{signal} value comparisons for Ti deposition thickness of 0.7 ML vs. ≥ 1 ML.

Polar scan ([100] azimuth) Ti on Al(001)		
η_{signal}	**0.7 ML Ti**	≥ 1 **ML Ti**
Al-clean	1.0	1.0
Al-peak	0.6	0.2
Ti-peak	0.2	0.2

Contrasting the $\eta_{Al-peak}$ and $\eta_{Ti-peak}$ values for the low and high Ti coverage cases, we concluded that Ti atom occupancy is comparable to Al atom occupancy in the top layers at the higher Ti coverage. This same argument will apply for the [110] azimuth Ti-Al data sets.

Figure 9.7(b) for the high V coverage set in the [110] azimuth, as in the low V coverage set, the Al-peak signal is of similar shape to the Al-clean signal suggesting that Al atoms post V-deposition occupy similar sites as in the clean substrate. The scale-factor ($\eta_{Al-peak} = 0.3$) shows a further diminished intensity of the signal at this coverage compared to the lower V coverage as can be seen in Table 9.5, signifying even fewer ion-to-Al-atom interactions have occurred. This points to a greater presence of V atoms in either the 2nd or 1st layers as explained in the analysis for the lower coverage set.

Table 9.5: Polar scan ([110] azimuth) η_{signal} value comparisons for V deposition thickness of 0.6 ML vs. 2.5 ML.

Polar scan ([110] azimuth) V on Al(001)		
η_{signal}	**0.6 ML V**	**2.5 ML V**
Al-clean	1.0	1.0
Al-peak	0.6	0.3
V-peak	0.1	0.1

The [110] azimuth V-peak signal, at this higher V coverage is similar to that at the lower V coverage, showing the same overall shape and presence of a strong peak at the leading edge at reference line *A*. The more distinct small peaks at reference lines *B, C* and *D* in the lower V coverage V-peak signal for the [110] azimuth direction in Figure 9.6(b) have evolved into what appears to be a higher relative intensity with a loss of peak resolution at these reference lines for the corresponding V-peak signal in Figure 9.7(b). This could indicate that at this higher V coverage there exists a less ordered structure in the 3rd layer, with respect to the original Al-lattice sites. But regardless, as for the lower V coverage set, the similar shape of the V-peak signal signal to the Al-clean signal suggests that the structure formed by V atoms in this plane is similar to that of the clean substrate.

Let us also list the η_{signal} values for the polar scans in the [110] azimuth for Ti low- and high-coverage sets, which can be seen in Table 9.6.

Table 9.6: Polar scan ([110] azimuth) η_{signal} value comparisons for Ti deposition thickness of 0.7 ML vs. ≥ 1 ML.

Polar scan ([110] azimuth) Ti on Al(001)		
η_{signal}	**0.7 ML Ti**	≥ 1 **ML Ti**
Al-clean	1.0	1.0
Al-peak	0.6	0.2
Ti-peak	0.1	0.2

As in the [100] azimuth, the respective arguments for V atoms preferring sub-surface occupancy for both the low and high coverage sets can be repeated here when contrasting $\eta_{Al-peak}$ with η_{V-peak} for both coverages as seen in Table 9.5. The difference is not as high as for the high V coverage case suggesting that V occupancy does increase in the surface layers at this higher coverage.

For the Ti η_{signal} values seen in Table 9.6, the trend is similar to that in the [100] azimuth, allowing us to make the same inference that for sub-monolayer coverage, Ti atoms prefer sub-surface occupancy, while at the higher coverage, Ti and Al occupancy in the surface layers is comparable. This indicates then that at higher coverage, Ti atoms tend to populate surface layers in the substrate to a greater degree than V atoms do.

9.5 Summary of V-Al LEIS Results

LEED results for low coverage V and especially for high coverage V on Al(001), show no evidence that a unique ordering of the surface layer structure is occurring, but rather the $p(1 \times 1)$ pattern for Al(001) becomes more blurry with higher V

deposition. This suggests that the placement of V atoms in the substrate surface layers is a random process.

For low coverage V, analysis of LEIS azimuth and polar scans suggests that V prefers subsurface occupancy. For high coverage V, the results suggest that V continues to have a preference to subsurface occupancy, but also indicating that the presence of V in the surface layers does increase as V coverage increases.

9.6 Contrasting Ti and V on Al(001)

LEED results show that the Ti-Al system produces a blurry but undeniable $c(2\times2)$ pattern. For the V-Al system, a blurry $p(1 \times 1)$ pattern is present.

LEIS results show that for low-coverage, both Ti and V prefer subsurface occupancy. For high-coverage Ti and V, LEIS results suggest that Ti occupies surface layers more than V.

9.7 Conclusions

For V on Al(001) the less than optimal LEED patterns show no discernable changes from the typical $p(1 \times 1)$ pattern of a clean Al(001) surface, other than becoming more blurry for higher V coverage. This gives us little to work with in determining a structure in the surface layers, except for concluding that a disruption of the highly ordered structure of the clean Al substrate has occurred. This is in contrast to the Ti-Al system which shows a blurry but undeniable $c(2 \times 2)$ pattern for Ti-deposition thicknesses in the range of 0.7–3 ML.

LEIS azimuth- and polar-angle scan results indicate that V atoms prefer subsurface occupancy for both lower and high coverage cases. Due to the lack of quan-

titative information regarding ion-neutralization effects in sub-surface atomic layers [21], the data do not evidence any particular layer preference for V occupancy below the surface. From two higher-coverage polar-angle scan sets, we do conclude that V occupancy of surface layers increases compared to that for the lower V coverage set.

A qualitative comment regarding the structure of V on Al(001) can be proposed when considering the blurry quality of the LEED images especially at the higher coverages in light of the LEIS results. For LEED to yield a crisp image pattern, we must have long-range order in the scanning area covered by the LEED instrument. In contrast, LEIS will yield azimuth and polar scan spectra with discernable peaks at specific angles from shadow-cone interactions of target-collision atoms from atomic arrangements which possess only short-range order. That is, we can have short-range ordering of Al-V or V-V atom pairs at random spots in the sample surface layers which can give LEIS results as we have seen, but if order does not exist over a larger domain, a crisp LEED image cannot be formed. The results we have seen therefore are possible for occupation of V atoms at random sites in the Al lattice. In contrast, the $c(2 \times 2)$ LEED pattern for the Ti-Al system suggests that Ti atoms occupy every other Al lattice site.

In summary, the behavior of V deposited on Al(001) compared with that of Ti, for low coverages is similar, both elements preferring subsurface occupancy. For the higher coverage cases, V tends to still prefer subsurface occupancy, while Ti atoms tend to occupy surface layers more than do V atoms.

CHAPTER 10

CONCLUSION

10.1 A Contrasting Comparison of Ti and V on Al(001)

A comparison will now be made for Ti and V on Al(001). First we present a short results summary of what we found from the LEIS and LEED studies. Then we compare some properties and characteristics of Ti and V with Al, some of which can be interpreted to support our LEIS and LEED results, and others for the sake of showing distinctions between Ti and V. In the concluding subsection, we bring these ideas together to answer the question whether V can be considered as effective of an interlayer as Ti. Finally a section on proposed continued work will be presented.

10.1.1 LEED and LEIS Results Ti and V on Al(001)

Comparing the behavior of low-deposition thicknesses of V on Al(001) with that of Ti using LEED, we found that Ti produces a blurry but nonetheless undeniable $c(2 \times 2)$ LEED pattern while V continues to show the typical $p(1 \times 1)$ LEED pattern of clean Al(001) which becomes more blurry with greater deposition thickness. These observations allow us to conclude that Ti tends to occupy every other Al lattice site, while V appears to have no occupation preference and seemingly occupies random Al lattice sites near the surface of the crystal.

LEIS and LEED are both sensitive to only the top surface layers (top two or possibly three) of our sample. We determined that for sub-monolayer coverages both Ti and V prefer subsurface occupancy. For higher coverage of greater but near 1 ML, Ti appears to occupy the top surface layers more than V, a conclusion arrived at from the analysis of relative intensities and shapes of Ti-peak, V-peak and Al-peak LEIS

scans collected after deposition of the element, and comparing these to corresponding scans taken from the clean Al(001) surface.

10.1.2 Heats of Formation ΔH for Ti-Al and V-Al Alloys

We now consider the enthalpy or heat of formation ΔH^{for}, for Al-Ti and Al-V alloys. The enthalpy of formation is the energy absorbed in the formation of a compound by the bringing together of its separated constituent elements. Most values of the enthalpy of formation for compounds are negative, indicating energy is released in the formation of the compound. deBoer, et al. [3] created a model for theoretically calculating the enthalpy of alloy formation for compounds. We extract the enthalpy of formation from tables presented in their work for Ti, V and Al. Both ΔH^{for}_{exp} (experimental values) and ΔH^{for}_{calc} (values calculated from their model) will be listed. Our focus is to compare the enthalpy of formation of compounds for Ti and V with Al respectively. For our purposes, considering only the experimental entries will be sufficient, hence the calculated values are listed only for completeness.

Two tables are shown with data for the various alloy compounds. Multiple listings for the same alloy come from the author's different references for the experimental values. The data shown here are for ambient temperature (298K) conditions. ΔH^{for} has units of kJ/moles-of-atoms or simply kJ/mol. The method of calorimetry or assessment [3] were used for obtaining values for ΔH^{for}_{exp} that we have taken from the author's listing.

10.1.2.1 Ti Alloyed with Al:

The enthalpy of formation for four alloys for Al with Ti are listed in Table 10.1.

Energy released in the formation of Ti-Al compounds as seen in Table 10.1 indicates alloying is favorable. We can also surmise that the most negative value indicates

Table 10.1: Values for enthalpy of formation ΔH (kJ/mol) experimental and calculated [3] for alloys of Al with Ti at ambient temperature.

Compound	ΔH_{exp}^{for}	ΔH_{calc}^{for}
TiAl	-38	-61
	-36	
$TiAl_3$	-37	-39
	-37	
	-36	
Ti_3Al	-25	-39
$Ti_{88}Al_{12}$	-14	-19

the strongest bond. Out of the three most common, ΔH_{exp}^{for} for TiAl and $TiAl_3$ are nearly equivalent followed by Ti_3Al.

10.1.2.2 V Alloyed with Al: The enthalpy of formation for three alloys for Al with V are listed in Table 10.2.

Table 10.2: Values for heats of formation ΔH (kJ/mol) experimental and calculated [3] for alloys of Al with V at ambient temperature.

Compound	ΔH_{exp}^{for}	ΔH_{calc}^{for}
VAl_3	-28	-24
V_5Al_8	-23	-35
$V_{60}Al_{40}$	-15	-38

Once again, negative values for the enthalpy of formation indicate that alloying is favorable for V-Al compounds. Out of the two most common alloys, the values for ΔH_{exp}^{for} indicate that VAl_3 has the strongest bond followed by V_5Al_8.

10.1.2.3 Comparing Ti-Al with V-Al Alloys using ΔH^{for}: Comparing the heats of formation ΔH of Ti-Al and V-Al alloys from Tables 10.1 and 10.2 above, we can take the average of values listed for each compound. The three most common com-

pounds TiAl, $TiAl_3$ and Ti_3Al have heats of formation at -37, -36.7 and -25 kJ/mol respectively. Repeating for V, the two most common compounds VAl_3 and V_5Al_8 have heats of formation at -28 and -23 kJ/mol respectively. Overall the Ti-Al alloy compounds are more negative than those for V-Al (with the exception of Ti_3Al at -25 kJ/mol). We conclude therefore that on the average since more energy is released in Ti-Al bond formation, these bonds are stronger than V-Al bonds.

This conclusion is corroborated by the heat of formation from the results of the BFS Model which served as the motivation for this thesis. Table 6.11 shows $\Delta H_{Ti-Al} = -0.42$ ev/atom and $\Delta H_{V-Al} = -0.04$ ev/atom. Thus the Ti-Al pairing demonstrated a greater lowering of formation energy than the V-Al pairing, thus indicating that a Ti-Al bond is stronger than a V-Al bond.

10.1.3 Comparing Surface Energies for Bulk Ti, V and Al

We now address the surface energies of bulk Al, Ti and V. Vitos, et al. [4] used density functional theory (DFT) to calculate the surface energies for the low index surfaces of certain metals using a full charge density (FDC) linear muffin-tin orbitals (LMTO) method with the generalized gradient approximation (GGA). Table 10.3 lists their results for Al, Ti and V.

Table 10.3 shows that the surface energies for Al, Ti and V increase in this order. Though these data are for bulk Al, Ti and V and do not necessarily reflect the surface energies of each as they are deposited on the Al substrate, the difference in the energies for each, can give us a qualitative relative comparison. From the table we see that the values listed for V are substantially higher than those for Ti which by the same token are higher than those for Al. Qualitatively this ranking of surface energies for the three elements could suggest that when Ti and V are deposited onto Al, the preference would be for an Al surface layer. Furthermore, given the extent

Table 10.3: Surface energies calculated (FDC) and experimental (Exp) for Al, Ti and V for low index surfaces [4].

Metal	Structure (aÅ)	Surface	FCD (eV/atom)	FCD (J/m^2)	Exp (J/m^2)
Al	fcc (4.049)	(111)	0.531	1.199	1.143, 1.160
		(110)	0.919	1.347	
		(100)	0.689	1.271	
Ti	hcp (2.945)	(0001)	1.234	2.632	1.989, 2.100
		$(10\bar{1}0)_A$	2.224	2.516	
		$(10\bar{1}0)_B$	2.435	2.754	
V	bcc (3.021)	(110)	1.312	3.258	2.622, 2.550
		(100)	1.725	3.028	
		(211)	2.402	3.443	
		(310)	2.921	3.244	
		(111)	3.494	3.541	

that the surface energy of V is substantially higher than that for Ti, this suggests that V would penetrate deeper into the Al substrate compared to Ti. This premise is supported by our LEIS results for the Ti-Al and V-Al systems.

We can also comment on the alloys TiAl and VAl. TiAl binary pairing would be in a $L1_0$ *fcc*-type structure, the native structure of Al. Note the lattice constant for Ti's *hcp* structure of 2.945 Å is close to Al's nearest neighbor separation of 2.86 Å giving only a 3% mismatch. The native structure of V is *bcc* and we would expect VAl to take on the B2 *bcc*-like structure. V's lattice constant in the *bcc* structure is 3.021 Å which then gives nearly a 6% mismatch with Al. This suggests that the $L1_0$ structure of TiAl is more compatible with the *fcc* structure of Al(001) than the corresponding B2 structure of VAl, and this further supports the premise of the likelyhood of stronger bonding by Ti with Al in the surface layers of Al(001).

A comment regarding the $L1_0$ structure discussed above. The $c(2 \times 2)$ LEED pattern we see for Ti-Al indicates that for a particular layer, Ti occupies every other Al lattice site which is not compatible with the $L1_0$ structure of TiAl for all {100}

planes. The alloy formed between the two would more likely be $TiAl_3$ in a $L1_2$ structure, having Ti at every other lattice site in alternating layers with a full layer of Al atoms in between. The Ti on Al(001) system was studied by D. Spišák and J. Hafner [11] as mentioned in Chapter 1. DFT calculations were used to test the $Al_3Ti(001)$ compound, the surface being terminated with three layers comprised of $L1_2$ stacking, which provided an effective barrier to prevent diffusion of Fe into the substrate, which gives us a theoretical confirmation for the preference to the $L1_2$ stacking arrangement. Together with the argument that the lattice constant of *hcp* Ti is closer to nearest neighbor atomic separation in *fcc* Al than is the lattice constant of *bcc* V, we can conclude that the bonding strength of Ti-Al should be greater than for the V-Al system.

10.1.4 Atomic Size and Other Characteristics of Ti, V and Al

We now look at some atomic characteristics of Ti, V and Al listed in Table 10.4.

Table 10.4: Comparison of atomic characteristics of Al, Ti and V. [5].

Elem	Electronic Config.	Atomic Radius (Å)	Ionic Radius (Å)	Electro-Negativity (Pauling)	Electron Affinity (eV)	1^{st} Ionic Potential (eV)
Al	$[Ne]3s^2p^1$	1.43	0.54 (+3)	1.61	0.44	5.99
Ti	$[Ar]3d^24s^2$	1.45	0.61 (+4)	1.54	0.08	6.83
V	$[Ar]3d^34s^2$	1.31	0.54 (+5)	1.63	0.53	6.75

10.1.4.1 Electronegativity and Other Characteristics of Ti, V and Al: Along with atomic size, listed is the ionic radius with valence state indicated, electronegativity, electron affinity and 1^{st} ionic potential. The electronegativity is given in the Pauling Scale which is a relative measure of the ability of an element to attract an electron. The electron affinity is the energy released in the acceptance by the element

of an electron to make an anion. The 1st ionization potential is the energy required to remove one electron from the element to make a cation.

From Table 10.4 we see that the electronegativity of Al (1.61) falls between that of Ti (less at 1.54) and V (greater at 1.63). The values for the electron affinity of each follow the trend of the respective values for electronegativity. The 1st ionic potential values show that Al is the least among the three so Al is most willing to give up an electron.

It is interesting to note that the electronegativity of V and Al are relatively close compared to Ti and Al. This seems to suggest that for V and Al, both having a relatively high ability to attract an electron in the bonding process, would thereby not favor a strong bond as compared to Ti and Al, where Ti having a substantially less electronegativity would allow Al to attract its our shell $4s^2$ electrons and make for a stronger bond. The electronegativity ranking then of the three elements appears to be consistent with the results from the BFS Model as well as our experimental LEIS results.

10.1.4.2 Atomic Size of Ti, V and Al: Comparing the atomic sizes of Ti and V with that of Al can offer a case in support of a $c(2 \times 2)$ LEED pattern for Ti and a $p(1 \times 1)$ pattern for V.

From the table we see that the atomic radius of Al (1.43 Å) falls between that of Ti (greater at 1.45 Å) and V (less at 1.31 Å). From this we can postulate that Ti, the 'bigger' atom compared to Al, has a greater challenge to physically fit into the Al lattice structure, and thus would prefer to occupy every other lattice site than every consecutive one. Thus it is reasonable that Ti produces some semblance of a $c(2 \times 2)$ LEED pattern, albeit blurry as it is.

V on the other hand, is the 'smaller' of the pair with Al, and could therefore find comfortable accommodations in an Al lattice structure. V apparently would also find no hinderance in occupying successive Al lattice spacings or interstitial sites in the B2 structure. This could suggest that the occupation process of V in Al(001) has a random nature of filling the nearest available lattice site or interstitial. Thereby no distinctive LEED pattern forms and continues to show the $p(1 \times 1)$ pattern of clean Al, but gets fuzzier as V deposition thickness increases.

Due to its size, V would apparently more easily fit between Al atoms in the crystal compared to Ti, i.e. would not have to 'stretch' the lattice bonds as much and make its way to lower layers with much greater ease. This simple physical argument is congruent with the idea that V tends to populate subsurface layers more than Ti.

10.2 Conclusion: Effectiveness of V as an Interlayer Compared to Ti

An effective interlayer must have a sufficient presence in the top layers of the Al substrate to form the required bonds to stiffen the surface so as to act as a barrier to interdiffusion from a third element deposited on top [10, 11]. Considering that the enthalpy of formation of Ti-Al bonds is on the average more negative than those for V-Al bonds, we concluded that Ti forms stronger bonds in the surface layers with Al than V does. Using a comparison of relative peak height intensities for the two systems from LEIS polar-angle scan spectra, we concluded that V prefers to go more subsurface than Ti, so there is less bonding in the surface layers with Al for the same coverage of the two. Lastly, Ti is physically 'bigger' than Al and V is 'smaller' than Al, so V tends to diffuse into the bulk more easily. Thus for a Ti interlayer system, the top surface layers would be populated with Ti-Al bonds more than the corresponding V interlayer system would be with V-Al bonds.

Before we close the arguments in favor Ti being the more effective interlayer over V, a recent work in our group by W. Priyantha studied the use of Ti and V as interlayers between amorphous Fe and Al, and found that V does act effectively in this role as does Ti [39]. The amorphous state of the Ti-Al and V-Al interface suggests more freedom exists in the mechanism of bonding allowing the two pairs to choose the most favorable bond independent of structural considerations. This could explain that the two systems could act similarly in regards to stiffening an interface to prevent diffusion of the overlayer element Fe. However, the restriction of needing to conform with an existing crystal lattice, imposes an added complication to the bonding mechanism. Thus it is not practical to compare an amorphous system with one required to obey the constraints of a crystal lattice.

A final comment on the prediction by the BFS Model that motivated this study. From Table 6.11 we see that the formation energies $\Delta H_{Ti-Al} = -0.42$ ev/atom and $\Delta H_{V-Al} = -0.04$ ev/atom do differ substantially between the two elements Ti and V, and what is the most significant is the proximity to zero of ΔH_{V-Al}. Given the possibility that The BFS Model may be in error in calculation of the elemental parameters which form the foundation of the technique, it is not overstating that there is a chance that this value may be positive, and thus void the prediction. Furthermore, the basis of the BFS Model considers structural effects as secondary to energy of formation considerations, and the prediction made regarding V and Ti as interlayers was based on the use of the B2 *bcc*-like structure in all calculations. Thus we have reason to doubt the validity of this prediction. Based on all these arguments, we conclude that V will not be as effective of an interlayer as Ti on the Al(001) surface.

10.3 Future Work

10.3.1 Expanded Studies for Ti and V on Al(001)

We propose for future work, the collecting of LEIS spectra for depositions of Ti and V for coverages in increments of 1 ML or less, starting at $\leq$ 1 ML to about 4 ML. This analysis would provide a systematic development of the Ti- and V-peak signals as a function of deposition thickness. A direct comparison could be made of the subsurface occupation of Ti versus V on Al(001) based on qualitative RBS determination of thickness for each deposition.

10.3.2 Cr, Nb and Mo on Al(001)

Having explored Ti and V on Al(001), two other transition metals remain in Group 5 [1] in the BFS study. These are Nb and Mo. Both of these share the native *bcc*-structure with V, leaving Ti as the unique one of the four whose structure is *hcp*. Exploring Mo and Nb would allow us to determine if the native structure of the deposited species plays a role in the resulting structure when deposited on the Al(001) surface.

The plan of study would be similar to that implemented for Ti and V, i.e. for low-coverage depositions, observe the LEED pattern if any is discernable, followed by LEIS polar- and azimuth-angle scan spectra collection and subsequent analysis.

A. Vorontsov [40] noted that Cr ($3d^5 4s^1$) and Nb ($4d^4 5s^1$) have distinctly different d-shell characteristics compared to Ti ($3d^2 4s^2$) and V ($3d^3 4s^2$). Interestingly, Cr also has a native *bcc*-structure. Vanadium seems to be the bridge between Ti and the differently-configured valences of Cr and Nb. The BFS Model gives a formation energy $\Delta H_{Cr-Al} = +0.12$ eV/atom [1], a positive value. Thus Cr is not in the same sub-grouping as Ti and V. Furthermore this beaks a requirement of an effective

interlayer, since the pairing does not favor alloying. However, it would be interesting to test the BFS Model via experiment.

10.3.3 BFS Model Analysis of Fe-V-Al(001) Interlayer System

We presented a summary of Guille Bozzolo's analysis using the BFS Model for Alloys applied to the specific study of the effectiveness of Ti as an interlayer between Fe and Al and predicted that V should therefore act similarly in interlayer effectiveness. From our LEIS and LEED experimental studies, we concluded that the characteristics of the Ti-Al(001) and V-Al(001) interfaces were dissimilar to the extent to disagree with the BFS prediction.

Follow-up work could look into the BFS model more closely to see why it is erroneously predicting the similarity between Ti and V. The parameters for Ti and V used in the BFS Model may be set in such a way as to make a similarity evident, but these parameters may not be correct. Furthermore, the BFS Model study performed by Bozzolo with Ti consisted of detailed modeling of the interaction of crystal layers of Fe, Ti and Al leading to the conclusion of the effectiveness of Ti as an interlayer. Being that V was in the same BFS Model sub-grouping as Ti, V was predicted to have similar characteristics. An actual detailed BFS Model study was not performed using V with Fe and Al, so to arrive at a more conclusive prediction, the interlayer modeling study could be repeated with V.

10.3.4 RBS Channeling Study of Fe-V-Al(001) Interlayer System

Perform experimental work testing V as an interlayer between Fe and Al(001) using the RBS channeling technique. This will give definitive results for the effectiveness of V as an interlayer between Fe and Al.

10.3.5 Follow-up Work with Simulation of LEIS Polar Scans

Perform a comparison of simulations of LEIS polar scans generated using the TFM screening function with those using the Universal screening function. This is motivated by comparing the raw data simulations of polar scans in the [100] azimuth, see Figure 7.3 and Figure 7.5. In the former figure, the TFM screening function was used, note the distinctive peak at around 30°. In the latter figure this peak is nearly non-existent. The TFM and Universal screening functions have similar values over a large range of $x = r/a_U$ [2]. It would be interesting to contrast the use of the two screening functions when applied to the same crystal structure model.

REFERENCES CITED

[1] Dr. Guillermo Bozzolo. Ohio Aerospace Institute and NASA GRC, Ohio, U.S.A., private communication.

[2] J.F. Ziegler, editor. *The Stopping and Range of Ions in Solids*. Pergamon Press, New York, U.S.A., 1985.

[3] F.R. deBoer, D.G. Pettifor, editors. *Cohesion in Metals*. Elsevier Science Publishers B.V., 1989.

[4] L. Vitos, A. V. Ruban, H. L. Skriver, J. Kollár. The surface energy of metals. *Surf. Sci.*, **411**: 186–202, 1998.

[5] *Reriodic Table - Advanced*. BarCharts Inc.

[6] D. Spišák, J. Hafner. Interface stabilization of Fe/Al(001) films by Ti interlayers – an ab-initio DFT study. *Surf. Sci.*, **582**: 69–78, 2005.

[7] C.V. Ramana, P. Masse, R.J. Smith, Bum-Sik Choi. Using metallic interlayers to stabilize abrupt, epitaxial metal-metal interfaces, 2003.

[8] Jorge E. Garcés, Guillermo Bozzolo, Hugo O. Mosca, Phillip S. Abel. Determination of structural alloy equilibrium properties from quantum approximate methods. *Phys Rev B*, **71**: 134201, 2005.

[9] C.V. Ramana, W. Priyantha, R.J. Smith, Bum-Sik Choi. Thermal and chemical stability of epitaxial Fe films grown on the Ti-stabilized Al(100) surface. *Surf. Sci.*, **602**: 534–544, 2008.

[10] C.V. Ramana, N. Winward, R.J. Smith, Bum-Sik Choi. Epitaxial growth of bcc Fe films on Al(100) surfaces using Ti as an interface stabilizer. *Surf. Sci.*, **551**: 189–203, 2004.

[11] D. Spišák, J. Hafner. Theoretical study of Ti and Fe surface alloys on Al(001) substrate. *Appl. Surf. Sci.*, **252**: 5376–5378, 2006.

[12] D.S. Choi, M. Kopczyk, A. Kayani, R.J. Smith, Guillermo Bozzolo. Structure of ultrathin Ag films on the Al(100) surface. *Phys Rev B*, **74**: 115407, 2006.

[13] O. Kircher, M. Fichtner. Kinetic studies of the decomposition of $NaAlH_4$ doped with a Ti-based catalyst. *J. Alloys Compd.*, **404-406**: 339–342, 2005.

[14] Matej Mayer. *SIMNRA User's Guide*. Max-Plank-Institut fur Plasmaphysik, Germany, 2008.

[15] *Fundamental of Surface and Thin Film Analysis*. PTR Prentice Hall, New Jersey, U.S.A., 1986.

[16] D.R. Clarke, S. Suresh, I.M. Ward FRS, editors. *Ion-Solid Interactions: Fundamentals and Applications*. Cambridge University Press, Cambridge, U.K., 1996.

[17] J.R. Tesmer, M. Nastasi, editors. *Handbook of Modern Ion Beam Materials Analysis*. Materials Research Society, Pittsburgh, PA, U.S.A., 1995.

[18] J.W. Mayer, E. Rimini, editors. *Ion Beam Handbook for Materials Analysis*. Academic Press, Inc., New York, NY, U.S.A., 1977.

[19] M. Aono. Quantitative surface structure analysis by low-energy ion scattering. *Nucl. Instrum. Methods Phys. Res. B*, **2**: 374–383, 1984.

[20] R. Souda, M. Aono, C. Oshima, S. Otani, Y. Ishizawa. Thermal vibration amplitude of surface atoms measured by specialized low-energy ion scattering spectroscopy: TiC(111). *Surf. Sci.*, **128**: L236–L242, 1983.

[21] J.W. Rabalais. Low energy ion scattering and recoiling. *Surf. Sci.*, **299/300**: 219–232, 1994.

[22] R. Stumpf, R. Bastasz, J. A. Whaley, W. P. Ellis. Effect of adsorbed hydrogen on the stability of titanium atoms on aluminum surfaces. *Phys Rev B*, **77**: 235413, 2008.

[23] O.S. Oen. Universal shadow cone expressions for an atom in an ion beam. *Surf. Sci.*, **131**: L407–L411, 1983.

[24] S.S. Kim, K.S. Kim, N.G. Park, Y.W. Kim, K.H. Jeong, C.N. Whang, D.S. Choi. Universal curve for the shadowing critical angle in coaxial impact collision ion scattering. *Journ. Kor. Phys. Soc.*, **26**: 485–491, 1993.

[25] M. Aono, R. Souda. Quantitative surface atomic structure analysis by low-energy ion scattering spectroscopy (ISS). *Jap. Journ. Appl. Phys.*, **24**: 1249–1262, 1985.

[26] M. Aono. Quantitative surface structure analysis by low-energy ion scattering. *Nucl. Instrum. Methods Phys. Res. B*, **2**: 374–383, 1984.

[27] J. Morse, G. Bozzolo, J. Khalil. *adwTools, v2.6*. Ohio Aerospace Institute and NASA GRC, 2003.

[28] R. J. Smith, Y. W. Kim, N. R. Shivaparan, G. A. White, M. A. Teter. Growth of thin Ti films on Al single-crystal surfaces at room temperature. *Surf. Interface Anal.*, **27**: 185–193, 1999.

[29] A. A. Saleh, V. Shutthanandan, N. R. Shivaparan, R. J. Smith, T. T. Tran, S. A. Chambers. Epitaxial growth of fcc Ti films on Al(001) surfaces. *Phys Rev B*, **56**: 9841–9847, 1997.

[30] M.T. Robinson, I.M. Torrens. Computer simulation of atomic-displacement cascades in solids in the binary-collision approximation. *Phys Rev B*, **9**: 5008, 1974.

[31] M.H. Langelaar, M. Breeman, A.V. Mijiritskii, D.O. Boerma. Simulation of low-energy ion scattering. *Nucl. Instrum. Methods Phys. Res. B*, **132**: 578–584, 1997.

[32] C.A. Severijns, G. Verbist, H.H. Brongersma. SISS-92: a computer code for the simulation of ion-surface scattering. *Surf. Sci.*, **279**: 297–304, 1992.

[33] Yong Wook Kim. *Atomic Structures and Growth of Ag on Si(001).* Doctoral Dissertation, Yonsei University, Seoul, 120-749, Korea, Jun 1997.

[34] J.P. Biersack, L.G. Haggmark. *Nucl. Inst. and Meth.*, **174**: 257, 1980.

[35] Dr. Robert Bastasz. Sandia National Laboratories, Livermore, CA, U.S.A., private communication.

[36] S. Chaudhuri, J.T. Muckerman. First-principles study of Ti-catalyzed hydrogen chemisorption on an Al surface: A critical first step for reversible hydrogen storage in $NaAlH_4$. *J. Phys. Chem. B*, **109**: 6952–6957, 2005.

[37] S.K. Kim, F. Jona, P.M. Marcus. Growth of face-centered-cubic titanium on aluminum. *J. Phys. Condens. Matter*, **8**: 25–36, 1996.

[38] F. Jona Y. Tian, P. M. Marcus. Metastable phase of vanadium. *Phys Rev B*, **58**: 14051, 1998.

[39] W. Priyantha, H. Chen, M. Kopczyk, R.J. Smith, A. Kayani, A. Comouth, M. Finsterbusch, P. Nachimuthu, D. McCready. Interface intermixing of Al/Fe and Fe/Al multilayer systems and the role of Ti as a stabilizer layer using Rutherford backscattering spectroscoopy (RBS) and x-ray reflectrometry (XRR). *J. Appl. Phys.*, **103**: 014598, 2008.

[40] Dr. Anton Vorontsov. Department of Physics, Montana State University, Bozeman, MT, U.S.A., private communication.